UNIVERSITÉ DE
GRENOBLE

THÈSE

Pour obtenir le grade de

DOCTEUR DE L'UNIVERSITÉ DE GRENOBLE

préparée dans le cadre d'une cotutelle entre l'*Université de Grenoble* en France et l'*Université de Shandong en Chine*

Spécialité : **Physique Subatomique et Astroparticules**

Arrêté ministériel : le 6 janvier 2005 -7 août 2006

Présentée par

Jin WANG

Thèse dirigée par **Julien DONINI** et **Annick LLERES**
codirigée par **Cunfeng FENG**

préparée au sein de **Laboratoire LPSC Grenoble**

dans l'**Écoles Doctorale Physique**

Mesure de la section efficace de production du single top en voie-t en utilisant des arbres de decision avec ATLAS à sqrt(s)=7TeV

Thèse soutenue publiquement le **29 juin 2012**,
devant le jury composé de :

Prof. Yanwen LIU
Prof. USTC, Rapporteur
Prof. Chengguang ZHU
Prof. SDU, Membre
Prof. Denis GELE
DR2 Strasbourg, Rapporteur
Prof. Gerard SAJOT
Prof. Grenoble, Président
Prof. Cunfeng FENG
Prof. SDU, Directeur de thése
Prof. Julien DONINI
Prof. Clemont-Ferrand, Directeur de thése
Prof. Annick LLERES
CR1 Grenoble, Directeur de thése

Université Joseph Fourier / Université Pierre Mendès France / Université Stendhal / Université de Savoie / Grenoble INP

RÉSUMÉ

Cette thèse présente une mesure de la section efficace de production du quark-top célibataire en voie t avec $1,04\ fb^{-1}$ de données recueillies par le détecteur ATLAS au LHC à partir de collisions proton-proton d'énergie centre de masse $\sqrt{s} = 7$ TeV. Les événements sélectionnés contiennent un lepton, de l'énergie transverse manquante, et deux ou trois jets, l'un d'eux étant étiqueté comme étant issu d'un quark-b. Le modèle pour le bruit de fond se compose des processus multijets, W+jets et production de paires de quarks top ainsi que de contributions moindres venant d'événements Z+jets et diboson. En utilisant une sélection basée sur la distribution d'un discriminant multivarié construit avec des arbres de décision stimulés, la section efficace de production de quark-top célibataire en voie t a été mesurée. La valeur

$$\sigma_t = 97.3^{+30.7}_{-30.2}\ pb$$

a été obtenue. Ce résultat est en bon accord avec la prédiction du Modèle Standard.

En supposant que les éléments de la matrice CKM reliée au quark-top obéissent à la relation $|V_{tb}| \gg |V_{ts}|, |V_{td}|$, la force du couplage W-t-b est extraite à partir de la section efficace mesurée,

$$|V_{tb}| = 1.23^{+0.20}_{-0.19}.$$

Si on suppose que $|V_{tb}| \leq 1$, une limite inférieure $|V_{tb}| > 0.61$ est obtenue avec un niveau de confiance de 95%.

Abstract

This thesis presents a measurement of the cross section of t-channel single top-quark production using 1.04 fb^{-1} data collected by the ATLAS detector at the LHC with proton-proton collision at center-of-mass $\sqrt{s} = 7$ TeV. Selected events contain one lepton, missing transverse energy, and two or three jets, one of them b-tagged. The background model consists of multijets, W+jets and top-quark pair events, with smaller contributions from Z+jets and diboson events. By using a selection based on the distribution of a multivariate discriminant constructed with the boosted decision trees, the cross section of t-channel single top-quark production is measured:

$$\sigma_t = 97.3^{+30.7}_{-30.2} \ pb,$$

which is in good agreement with the prediction of the Standard Model.

Assuming that the top-quark-related CKM matrix elements obey the relation $|V_{tb}| \gg |V_{ts}|, |V_{td}|$, the coupling strength at the W-t-b vertex is extracted from the measured cross section,

$$|V_{tb}| = 1.23^{+0.20}_{-0.19}. \tag{1}$$

If it is assumed that $|V_{tb}| \leq 1$ a lower limit of $|V_{tb}| > 0.61$ is obtained at the 95% confidence level.

DEDICATION

To my parents Zhenfu WANG, Youying YU,
and my wife Jing CHEN.

TABLE OF CONTENTS

LIST OF FIGURES

Chapter 1

INTRODUCTION

What are the world's fundamental building blocks? Which kind of forces hold them together? These are the questions that people have long asked. Particle physics is the study of the basic elements of matter and the interactions between them. From the discovery of the electron about one hundred years ago (1897), the particle physics have developed gradually from the atomic theory to a theory called Standard Model (SM), which describes the three generations of quarks and leptons, as well as the four basic forces via force carrier particles. Standard model successfully explains and predicts a wide variety of experimental results. Although it still remains some questions without answers, such as the reason of the presence of only three generations of quarks, the reason that matters have mass, the problem of the gravity not included in the present formulation of the SM. The top quark, the last and heaviest quark in the SM, is sensitive to physics beyond the SM due to its large mass. The study of top quark is thus very interesting to test the SM and to probe new physics.

The Large Hadron Collider (LHC) located at CERN[1] and Fermilab Tevatron are the only places in the world that can produce top quarks under experiment steering. LHC collides proton and proton beams while Tevatron is a proton-antiproton collider. In both cases, the dominant top-quark production are from top-quark pair processes through strong interactions, while the top quarks are also produced singly via electroweak interactions, named single top-quark production.

The studies on single top-quark production help us to learn the weak interactions of the top quark. Its cross section measurement leads to a direct determination of one of the quantities predicted by the SM, the CMK matrix element $|V_{tb}|$. In addition, the rate

---

[1]Conseil Europeen pour la Recherche Nucleaire

of single top-quark production can be significantly modified by new-physics interactions. Thus the cross section measurement of single top-quark production provides an excellent examination of the SM and deviations from SM prediction give a hint of the presence of new physics. Further more, the single top-quark productions constitute as backgrounds to many possible new physics. The studies on single top-quark production are important in new-physics searching.

Single top-quark production consists of three different processes, t-channel, Wt associated production, and s-channel. This thesis presents a cross section measurement on t-channel single top-quark production using the data collected by ATLAS detector located at the LHC, contributing in one of the most recent results of single top-quark studies [18]. It is a test of the Standard Model and also gives further understandings on the single top-quark productions.

Chapter 2 of this thesis gives an introduction of the Standard Model and the top-quark physics. Then the LHC experiment and ATLAS detector are described in Chapter 3, where the reconstruction of the collected data are also explained. Chapter 4 shows the phenomenology of single top-quark t-channel production and possible background processes, as well as their modeling using Monte Carlo simulations.

Single top-quark t-channel cross section measurement starts with applying selections on data to select single top-quark t-channel signal enriched data set, so called pre-selection. A multivariate discriminator is then exploited by using boosted decision trees to further extract signal events. Chapter 5 of this thesis describes the pre-selection of data and the estimations of the backgrounds in the selected data. Then the application of boosted decision trees and the final cross section measurement are given in Chapter 6. Chapter 7 summarizes the results of this analysis and gives a perspective of the future single top-quark measurements.

Chapter 2

THE STANDARD MODEL AND TOP-QUARK PHYSICS

Particle physics has developed rapidly in the 20th century. Decades of theoretical and experimental discoveries lead to the Standard Model, which explains the fundamental particles of the world and their interactions. Top quark, the heaviest known fundamental particle in the Standard Model, is especially sensitive to new physics beyond the SM due to its large mass. The measurement of top-quark properties is an excellent test of the SM and a key part of new physics searching.

This chapter will give a short introduction to the particle physics and its evolution from the beginning. Then the Standard Model is briefly described. At the end the top-quark physics is discussed in detail.

2.1 Particle Physics

Particle physics is a branch of physics which studies the fundamental constituents of matter and defines how they interact with each other. It is also called High Energy Physics, because most of the studied particles are created through very energetic collisions with other particles, normally in particle accelerators or cosmic rays.

The discovery of the first fundamental particle in particle physics can be tracked back to 1897, the identification of the electron by J. J. Thomson. In 1919, Ernest Rutherford discovered the proton as a product of the decay of the nitrogen nucleus. 13 years later, James Chadwick discovered the neutron, another particle located within the nucleus. The scientists at that time believed that these were the smallest atomic building blocks. Along with the photon hypothesized by Albert Einstein in 1905, the neutrino postulated by Wolfgang Pauli in 1930 and the positron discovered by Carl D. Anderson in 1932, these particles were called "elementary particles".

Then a lot of particles were discovered from 1930s to 1960s, such as the lepton μ in 1936, the strange particle Kaon in 1947, the pion in 1947, as well as their anti particles in 1950s. The accelerators and detector developed fast and were widely used for the new particle searching. People started to wonder which were the fundamental particles and how to classify these new particles.

In 1964, Murray Gell-Mann and George Zweig proposed the quark model, which introduced the up, down and strange quark as parts of an ordering scheme for hadrons. Soon their theory was proven by deep inelastic scattering experiments at the Stanford Linear Accelerator Center in 1968. The discovery of the J/ψ in 1974 introduced the charm quark and ushered in a series of breakthroughs. The Standard Model was then developed in early 1970s. The left bottom quark and top quark predicted by the Standard Model were found by Fermilab in 1977 and 1995 respectively. With the discovery of the heavy gauge bosons W and Z in 1983, the theory of electroweak interactions in the Standard Model was firmly established. The Standard Model has become a well-tested physics theory with its success on explaining lots of experimental results and precise prediction of a wide variety of phenomena.

Elemental Particles
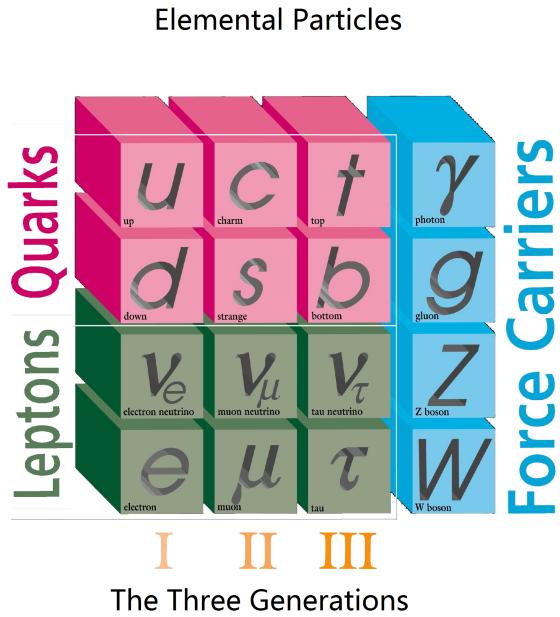
Figure 2.1: The elementary particles in the SM.

2.2 Standard Model

The Standard Model (SM) is a theory of the fundamental particles and the fundamental forces. It explains all the particles and their complex interactions with:

- 6 quarks,

- 6 leptons,

- 4 interactions (forces) with corresponding force carriers.

For each kind of matter particle there is a corresponding antimatter particle. All known particles are composed of quarks and leptons, and interact by exchanging force carrier particles. The quarks and leptons are categorized into three generations, as shown in Figure 2.1.

The 6 kinds of quarks are the up (u), down (d), charm (c), strange (s), bottom (b) and top (t) quarks. The u, c and t quarks are up-type quarks with $+\frac{2}{3}$ charge, while the d, s and b quarks are the down-type quarks with charge $-\frac{1}{3}$. The 6 leptons are electron (e), muon (μ), tau (τ) with charge -1 and their corresponding neutrinos ν_e, ν_μ, ν_τ with no charge.

All quarks and leptons are fermions with spin of $\frac{1}{2}$. The quarks also have colour charge and carry a baryon number $\frac{1}{3}$. And all leptons carry a lepton number $L = 1$.

In the world around us, the stable matter are composed by only the first generation of quarks and leptons. This is due to the fact that heavy quarks and leptons quickly decay to the lighter ones until they reach the stable level. The quarks could decay (flavor change) through the weak interaction by exchanging a W boson. The transformation from mass eigenstates to eigenstates of the weak interaction is described by the Cabibbo-Kobayashi-Maskawa (CKM) matrix [25]:

$$
\begin{pmatrix} |d' > \\ |s' > \\ |b' > \end{pmatrix} = \begin{pmatrix} V_{ud} & V_{us} & V_{ub} \\ V_{cd} & V_{cs} & V_{cb} \\ V_{td} & V_{ts} & V_{tb} \end{pmatrix} \begin{pmatrix} |d > \\ |s > \\ |b > \end{pmatrix} \tag{2.1}
$$

On the left is the weak interaction doublet partners of up-type quarks, and on the right is the CKM matrix along with a vector of mass eigenstates of down-type quarks. The CKM matrix element V_{ij} is the coupling constant that determines the coupling strength of two quarks i and j to a W boson. The square of the matrix elements $|V_{ij}|^2$ is proportional to the probability that the quark of i flavor decays into a quark of j flavor. A current best determination of the magnitudes of the CKM matrix elements is given by [26]

$$
\begin{pmatrix} V_{ud} & V_{us} & V_{ub} \\ V_{cd} & V_{cs} & V_{cb} \\ V_{td} & V_{ts} & V_{tb} \end{pmatrix} = \begin{pmatrix} 0.97428 \pm 0.00015 & 0.2253 \pm 0.0007 & 0.00347^{+0.00016}_{-0.00012} \\ 0.2252 \pm 0.0007 & 0.97345^{+0.00015}_{-0.00016} & 0.0410^{+0.0011}_{-0.0007} \\ 0.00862^{+0.00026}_{-0.00020} & 0.0403^{+0.0011}_{-0.0007}0 & 0.999152^{+0.000030}_{-0.000045} \end{pmatrix}
$$

The photon (γ), gluon (g), Z boson (Z) and W (boson) are the force carrier particles with spin of 1. They transmit three of the four fundamental forces in nature. The four fundamental forces are: the strong force, the weak force, the electromagnetic force and the gravitational force. They work over different ranges and have different strengths. The strong force, which binds together quarks inside protons and neutrons and holds together particles inside an atomic nucleus, is mediated by gluons. The electromagnetic force uses photon as carrier particle to generate the force between charged particles. The weak force, playing a role in radioactive decay, is mediated by the W and Z bosons. Gravity is the

weakest force but with an infinite range. It is the force between all matters due to their mass. The force-carrying particle of gravity is not yet found in the experiment.

Physicists are expecting a grand unified theory that would unite all four of the forces. The electromagnetic, weak and strong interaction can be unified in Standard Model by a combination of local gauge symmetry groups: $SU(2)_L \otimes U(1)_Y \otimes SU(3)_C$. The electroweak theory based on $SU(2)_L \times U(1)_Y$ and the Quantum Chromodynamics theory (QCD) based on $SU(3)_C$ gauge symmetry group are briefly introduced below. Despite that, the gravity is proved to be very difficult to fit in Standard Model, although it does not play a significant role since it is so weak as to be negligible in minuscule scale of particles.

2.2.1 Electroweak Theory and Higgs Mechanism

The electromagnetic and weak interactions are unified by interpreting $SU(2)_L \times U(1)_Y$ as the group of gauge transformations under which the Lagrangian is invariant [27, 28, 29, 30]. To give $W\pm$, Z boson mass, the full symmetry has to be broken by the Higgs mechanism down to the electromagnetic gauge symmetry [31]. Thus the gauge invariant Lagrangian of electroweak theory is constructed by the gauge, fermion and Higgs parts:

$$\mathcal{L}_{EW} = \mathcal{L}_G + \mathcal{L}_F + \mathcal{L}_H \tag{2.2}$$

Gauge fields

The pure gauge field Lagrangian $\mathcal{L}_G$ is invariant under non-Abelian gauge transformations. It is formed by:

$$\mathcal{L}_G = -\frac{1}{4}W^i_{\mu\nu}W^{\mu\nu,i} - \frac{1}{4}B_{\mu\nu}B^{\mu\nu},$$

where the isotriplet W^i_μ , i = 1, 2, 3, and the isosinglet B_μ lead to the field strength tensors:

$$W^i_{\mu\nu} = \partial_\mu W^i_\nu - \partial_\nu W^i_\mu + g_1 \epsilon^i{}_{jk} W^j_\mu W^k_\nu$$
$$B_{\mu\nu} = \partial_\mu B_\nu - \partial_\nu B_\mu \tag{2.3}$$

Here, g_1 is the non-Abelian $SU(2)$ gauge coupling constant, ϵ^{ijk} is the $SU(2)$ structure constant. The observable weak gauge bosons $W^\pm$, Z and γ can be expressed by the combination

of the gauge fields W_μ^i and B_μ:

$$W_\mu^\pm = \frac{1}{\sqrt{2}}(W_\mu^1 \mp W_\mu^2) \tag{2.4}$$

$$A_\mu = B_\mu \cos\theta_W + W_\mu^3 \sin\theta_W \tag{2.5}$$

$$Z_\mu = W_\mu^3 \cos\theta_W - B_\mu \sin\theta_W \tag{2.6}$$

with Weinberg angle θ_W:

$$\cos\theta_W = \frac{g_1}{\sqrt{g_1{}^2 + g_2{}^2}}. \tag{2.7}$$

The g_2 is the Abelian $U(1)$ coupling constant.

Fermion fields

$\mathcal{L}_F$ describes the interactions between fermions and the gauge fields:

$$\mathcal{L}_F = \sum_j \bar{\psi}_j^L i\gamma^\mu D_\mu \psi_j^L + \sum_{j,\sigma} \bar{\psi}_{j\sigma}^R i\gamma^\mu D_\mu \psi_{j\sigma}^R \tag{2.8}$$

ψ_j^L represents the left-handed fermion fields of each lepton and quark family with family index j:

$$\psi_j^L = \begin{pmatrix} \psi_{j+}^L \\ \psi_{j-}^L \end{pmatrix}$$

while the right-handed fields is:

$$\psi_j^R = \psi_{j\sigma}^R$$

where $\sigma = \pm$ is the component index. D_μ is the covariant derivative to ensure the gauge invariance of the Lagrangian:

$$D_\mu = \partial_\mu + ig_1 I_i W_\mu^i + ig_2 \frac{Y}{2} B_\mu. \tag{2.9}$$

Here, I_i is the quantum numbers of the weak isospin and Y is the weak hypercharge.

The Higgs Mechanism

The Higgs mechanism is an extension of the spontaneous symmetry breaking to create massive vector bosons in a gauge invariant theory, while keeping the photon massless [31].

The Lagrangian terms of Higgs scalar field is

$$\mathcal{L}_H = (D_\mu \Phi)^\dagger (D^\mu \Phi) - V(\Phi), \tag{2.10}$$

while D_μ is the covariant derivative to preserve the gauge invariance under the gauge transformation:

$$D_\mu = \partial_\mu - ig_1 I_i W_\mu^i + i\frac{g_2}{2} B_\mu. \tag{2.11}$$

The Φ is scalar doublet filed with hypercharge $Y = 1$:

$$\Phi = \begin{pmatrix} \phi^+ \\ \phi^0 \end{pmatrix}, \tag{2.12}$$

and $V(\Phi)$ is the potential term:

$$V(\Phi) = \mu^2 \Phi^\dagger \Phi + \lambda (\Phi^\dagger \Phi)^2. \tag{2.13}$$

Φ has a non-vanishing vacuum expectation value

$$< \Phi >_0 = \frac{1}{\sqrt{2}} \begin{pmatrix} 0 \\ v \end{pmatrix}, \qquad with \qquad v = \sqrt{-\frac{\mu^2}{\lambda}} \tag{2.14}$$

In the unitary gauge, the Higgs field has the simple form

$$< \Phi > = \frac{1}{\sqrt{2}} \begin{pmatrix} 0 \\ v + H \end{pmatrix}. \tag{2.15}$$

The real field H describes physical neutral scalar particles with mass

$$M_H = \sqrt{-2\mu^2}. \tag{2.16}$$

The Higgs kinetic term $(D_\mu \Phi)^\dagger (D^\mu \Phi)$ produces the gauge boson masses

$$\begin{aligned} M_{W^\pm}{}^2 &= \frac{g_1{}^2 v^2}{4}, \\ M_Z{}^2 &= \frac{v^2}{4}(g_1{}^2 + g_2{}^2). \end{aligned} \tag{2.17}$$

Fermion masses are generated by interactions between Higgs field and the fermions in a gauge invariant way. This can be described by Yukawa couplings [32] between Higgs scalar field Φ and fermion field ψ

$$\mathcal{L}_{Yukawa} = g_\psi (\bar{\psi}_L \Phi \psi_R + \bar{\psi}_R \Phi^\dagger \psi_L). \tag{2.18}$$

where g_ψ denotes the Yukawa coupling constant of the fermion. Via the Yukawa coupling of the Higgs doublet to the fermions, the vacuum expectation value gives masses to fermion particles, $m_f = \lambda_f v/\sqrt{2}$. In particular, to explain the large top-quark mass the coupling of the top quark to the Higgs boson has to be of order unity,

$$\lambda_{top} = \sqrt{2} m_{top}/v \approx \sqrt{2} \times 173/246 \approx 0.99, \tag{2.19}$$

which might suggest a special role of the top quark in electroweak symmetry breaking.

2.2.2   Quantum Chromodynamics Theory

The strong interaction between quarks and gluons are described by another non-abelian gauge theory with $SU(3)_C$ symmetry group, the Quantum Chromodynamics theory (QCD) [33]. The QCD attributes the quarks an internal quantum number colour charge, red, green and blue. Quarks interact by emitting and absorbing massless gluons, each of which carries one unit of colour and one unit of anticolour. Eight kinds of gluons are required to transmit the strong force between quarks. The quarks form colourless hadrons, which are mesons with a quark and an antiquark or bayons with three quarks or antiquarks (e.g a proton(uud)). Inside the hadron, the gluons emitted by quarks can split into quark-antiquark pairs (sea quark), resulting a bevy of quarks and gluons (gluon-quark sea) that constantly blink into and out of existence. QCD theory has a feature called confinement hypothesis, which refers that the quarks have to be confined within colour singlet bound states. The forces between quarks get stronger when they are pulled apart and will be large enough to create new quark-antiquark pairs to form new hadrons before they are unbounded to be free. The process that forms hadrons out of quarks and gluons is called hadronization. Another feature of QCD is called asymptotic freedom, indicating that the strength of strong interaction progressively decreases as quarks and gluons get closer to each other until it vanishes at zero distance.

Quark fields Ψ are in triplet colour representation. The eight gluon filed $G_a^\mu, a = 1, 2, ..., 8$ have the field strength,

$$G_{\mu\nu}^a \equiv \partial_\mu G_\nu^a - \partial_\nu G_\mu^a + g_s f^a{}_{bc} G_\mu^b G_\nu^c, \tag{2.20}$$

where f^{abc} are the structure constants of the $SU(3)$ colour group, and g_s characterizes the QCD coupling strength α_s,

$$\alpha_s = \frac{g_s^2}{4\pi}. \tag{2.21}$$

The covariant derivative acting on the quark triplets is,

$$D_\mu = \partial_\mu - ig_s \frac{\lambda_a}{2} G_a^\mu, \tag{2.22}$$

where the $\lambda_a, a = 1, 2, ..., 8$ are the Gell-Mann 3×3 matrices. Then the $SU(3)_c$ gauge invariant Lagrangian of QCD can be written as,

$$\mathcal{L}_{QCD} = \bar{\Psi}(i\gamma^\mu D_\mu - m)\Psi - \frac{1}{4} G_a^{\mu\nu} G_{\mu\nu}^a. \tag{2.23}$$

2.3 Top-quark Physics

With the discovery of bottom quark in 1977, the Standard Model of elementary particles predicted the existence of top quark, the last quark in the three generations of quarks. 18 years later in 1995, this prediction was proven by the discovery of top quark at Tevatron by CDF and D0 experiments [34, 35]. In Standard Model, the top quark is an elementary fermion with spin 1/2 and electric charge of +2/3. As one of the elementary particles with no internal structure, the top quark has an extraordinary large mass of $173.2 \pm 0.9\,\mathrm{GeV}$ [36], which is even more massive than most of the elements in the periodic table. The large mass of top quark enables it to decay to a less massive on-shell W boson via electroweak interaction, before the hadronization takes place. It makes the top quark the only quark whose properties can be studied experimentally without the complications of hadronization effects. Thus the Standard Model prediction of these properties can be tested with precise measurements. Top quark also plays an important role in models of electroweak symmetry breaking (EWSB) due to its mass close to EWSB scale. Further more, the measured top-quark mass, together with the W boson mass, can be used to constrain the Higgs mass based via its contribution to the radiative correction [37]. In Standard Model, the top quark decays to a W boson and a b almost 100% of the time, where about 70% of the W bosons are longitudinally polarized. Some models in the New Physics (NP) beyond SM indicate the modifications on the top-quark decay ratio and the decayed W-boson helicity comparing to the SM prediction. These new physics can be proved or denied by the precision measurement of the top-quark production.

As a conclusion, the study of top quark is very important to test Standard Model and to probe the possible New Physics. In this section the top-quark production and its decay are explained in detail. Then the latest results of the measurement on top-quark properties are introduced.

2.3.1 Top-quark Production

The top-quark can be produced from top-quark pair processes through strong interactions and single top-quark processes via electroweak interactions.

Top-quark Pair Production

The top-quark pairs are produced by the strong interaction between partons (quark, anti-quark, gluon) in hadron collisions. Assume the collision hadrons are A and B with momentums p_A and p_B, the two partons that create top quark are i from A and j from B with momentums p_i and p_j. The cross section of top-quark pair production at center-of-mass energy $\sqrt{s}$ can be written as [1]:

$$\sigma(AB \to t\bar{t}) = \sum_{i,j=q,\bar{q},g} \int dx_i dx_j f_{i/A}(x_i, \mu^2) f_{j/B}(x_j, \mu^2) \cdot \hat{\sigma}_{ij}(ij \to t\bar{t}; \hat{s}, \mu^2) \qquad (2.24)$$

x_i and x_j are the momentum fraction of partons $x_i = p_i/p_A, x_j = p_j/p_B$, $\hat{\sigma}_{ij}$ is the parton-parton cross section. $f_{i/A}$ is the parton distribution function (PDF), which describes the probability density for finding a parton i inside the hadron A. $\hat{s}$ denotes the square of the center-of-mass energy of the colliding partons,

$$\hat{s} = (p_i + p_j)^2 = (x_i p_A + x_j p_B)^2 \approx 2x_i x_j p_A p_B \approx x_i x_j (p_A + p_B)^2 = x_i x_j s \qquad (2.25)$$

Here the terms proportional to parton mass and hadron mass are neglected since they are very small comparing to the collision energy. By convention, the scale μ satisfies $\mu = \mu_F = \mu_R$, where the μ_F is the factorization scale introduced by the factorization, and μ_R is the renormalization scale from the normalization procedure to calculate $\hat{\sigma}_{ij}$. In the case of top-quark production, it is set with top-quark mass $\mu = m_t$, while different choices between $m_t/2$ and $2m_t$ are used to calculate indicative theoretical uncertainties to the cross section prediction.

As shown in the function above, the top-quark pair production have contributions from $gg \to t\bar{t}, q\bar{q} \to t\bar{t}, qg \to t\bar{t}$ and $g\bar{q} \to t\bar{t}$ processes. Figure 2.3.1 show their corresponding luminosities L_{ij} as a function of $\sqrt{\hat{s}}$, where we can notice that the qg process has the highest luminosity at the LHC. But the cross sections $\hat{\sigma}_{qg}$ and $\hat{\sigma}_{g\bar{q}}$ are of order $\alpha_s{}^3$ (α_s is QCD coupling strength introduced in Section 2.2.2), which are much smaller comparing to $\hat{\sigma}_{gg}$ and $\hat{\sigma}_{q\bar{q}}$ of order $\alpha_s{}^2$. As a result, about 90% top-quark pairs are produced by gluon-gluon fusion (gg process) at the LHC at $\sqrt{s} = 14$ TeV. Another 10% are from quark-antiquark annihilation ($q\bar{q}$ process). At the Tevatron, about 85% contribution of top-quark

14

pair production are from $q\bar{q}$ process and 15% from gg process. At both of the LHC and Tevatron, qg and $g\bar{q}$ processes only contribute to top-quark pair production at 10^{-2} level.
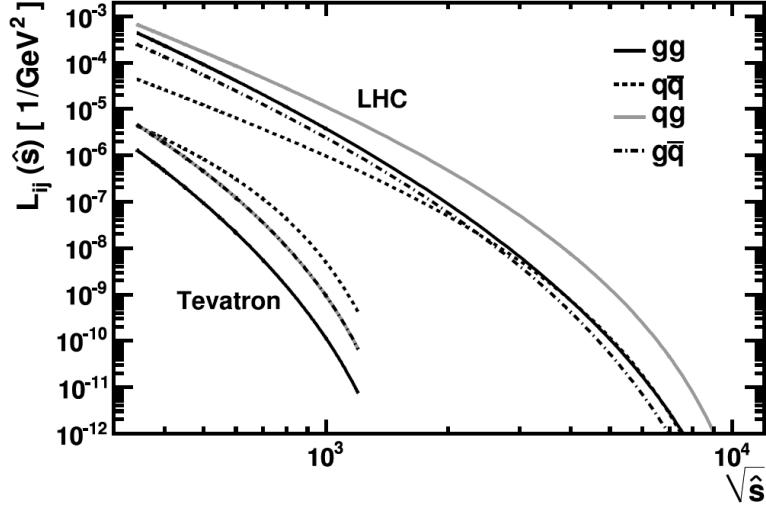
Figure 2.2: Parton luminosities for gluon-gluon, quark-antiquark, quark-gluon and gluon-antiquark interactions at the LHC and Tevatron [1].

gg and $q\bar{q}$ processes are the Leading Order (LO) processes while qg and $g\bar{q}$ processes are formally Next-to-Leading-Order (NLO) corrections. The Feynman diagrams of gg and $q\bar{q}$ processes for $t\bar{t}$ production are shown in Figure 2.3.1.
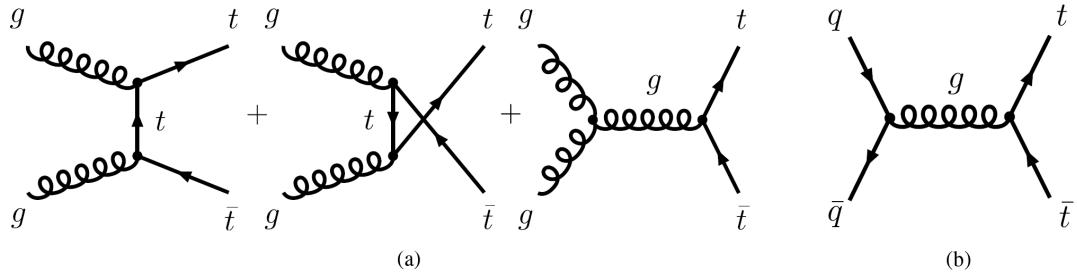
Figure 2.3: Feynman diagrams of the LO processes for $t\bar{t}$ production: (a) gluon-gluon fusion $(gg \rightarrow t\bar{t})$ and (b) quark-antiquark annihilation $(q\bar{q} \rightarrow t\bar{t})$.

$\hat{\sigma}_{ij}$ can be calculated in perturbative QCD. The leading order cross section calculation

is given by the reference [38]. The LO cross section predictions are not reliable due to their huge dependence on the renormalization scale μ_R and factorization scale μ_F. More accurate predictions can be obtained by taking into account the Next-to-Leading-Order (NLO) corrections. The NLO calculations involve virtual contributions to the LO process, the final state gluon bremsstrahlung, gluon splitting and the flavor excitation processes. Details about NLO calculation for $t\bar{t}$ cross section can be found in reference [39]. More studies on achieving further accuracy using Next-to-Next-to-Leading logarithmic (NNLL) [40] and Next-to-Next-to-Leading-Order (NNLO) [41] are undergoing. In this thesis, an approximate NNLO cross section at $\sqrt{s} = 7$ TeV, $\sigma_{t\bar{t}} = 164.6$ pb [42] with $m_t = 172.5$ GeV, is used for the modeling of $t\bar{t}$ production.

Single Top-quark Production

In contrast to the top-quark pair production from strong interactions, top quarks can be produced singly at the hadron collider via electroweak interaction. There are three different single top-quark production modes, which can be distinguished by the virtuality Q^2 of the W boson where

$$Q^2 = -q^2, \qquad q \text{ is the four momentum of the } W \text{ boson.}$$

One of them is called t-channel process and proceeds via the exchange of a space-like W boson $(q^2 < 0)$; a second one is the s-channel process that fusions two quarks and produces a time-like W boson $(q^2 \geq (m_t + m_b)^2)$; a third one is Wt channel process where the top quark is produced in association with a real W boson $(q^2 = M_W^2)$.

In all channels, single top-quark is produced dominantly via Wtb vertex. The cross section of these three single top-quark channels are proportional to the square of CKM matrix element $|V_{tb}|$ (See Section 2.2 for $|V_{tb}|$). The measurement of the single top-quark production is the only way to directly determine this CKM matrix element. The single top-quark productions through Wtd or Wts vertices are strongly suppressed due to the small $|V_{td}|$ and $|V_{ts}|$. Thus their contributions are neglected and not considered in this thesis.

1. t-channel single top-quark production
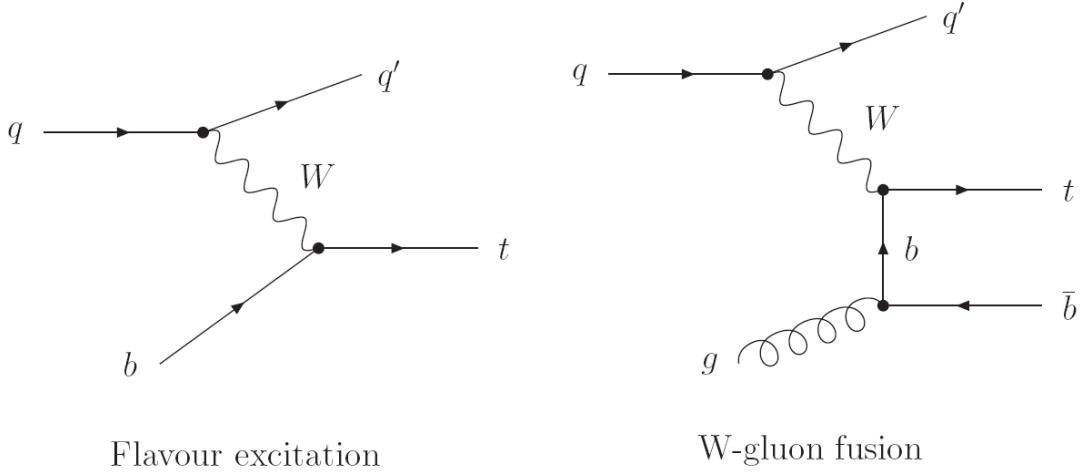
Figure 2.4: Leading order Feynman diagrams for single top-quark t-channel production.

Figure 2.4 shows the Leading-Order Feynman diagrams for single top-quark t-channel production. In the t-channel, there are two kinds of productions, the flavour excitation production $qb \to q't$ and the W-gluon fusion production $qg \to q't\bar{b}$. The flavour excitation production corresponds a five-flavour scheme while W-gluon fusion production corresponds to a four-flavour scheme [43]. There are two different approaches of single top-quark t-channel production with different treatment for the b-quark and different calculation of the t-channel production cross section. In the five-flavour scheme the initial b-quark is from the quark sea inside the proton, with its luminosity described by a PDF set. It is considered massless at leading order. In the four-flavour scheme, the b-quark comes from a gluon splitting into a $b\bar{b}$ pair and its mass is taken to be non-zero already at leading order.

At both the LHC and Tevatron, the t-channel process is the dominate process for single top-quark production. The initial light quark q shown in Figure 2.4 can be u, d, s, c or their antiquark. The top quark is produced with initial quark $u, \bar{d}, \bar{s}, c$, while for antitop-quark production they are $\bar{u}, d, s, \bar{c}$. Table 2.1 shows the contributions of different parton process to single top-quark and antitop-quark t-channel production [44]. LHC is proton-proton (u,u,d quark in a proton) collider, resulting larger cross section of top-quark production

than the one of antitop-quark production. At the proton-antiproton collier Tevatron, the cross sections for top-quark and antitop-quark productions are the same.

top-quark production		antitop-quark production	
$ub \rightarrow dt$	74%	$d\bar{b} \rightarrow u\bar{t}$	56%
$\bar{d}b \rightarrow \bar{u}t$	12%	$\bar{u}b \rightarrow \bar{d}\bar{t}$	20%
$\bar{s}b \rightarrow \bar{c}t$	8%	$s\bar{b} \rightarrow c\bar{t}$	13%
$cb \rightarrow st$	6%	$\bar{c}\bar{b} \rightarrow \bar{s}\bar{t}$	11%

Table 2.1: Contributions of different parton processes to the t-channel single top-quark and antitop-quark production at the LHC at $\sqrt{s} = 14$ TeV [44].

In single top-quark t-channel and s-channel processes, the produced top quark is 100% polarized along the direction of the d ($\bar{d}$) quark, because in the Standard Model the W boson couples only to fermions with left-handed chirality. Any observation of a different top-quark polarization state in the experiment would indicate the new physics effects.

The leading order cross section of t-channel single top-quark production can be calculated by squaring and convoluting with the parton density functions (PDFs) for the initial state b-quark and light quark (or gluon and light quark), performing the phase space integral and including the overall flux factor. The PDFs of quarks in the parton (see also Section 2.3.1) are extracted from global fits to measurements of deep inelastic scattering experiment.

The NLO QCD corrections on the cross section calculation consist of two parts: the one-loop virtual correction to the $2 \rightarrow 2$ (or $2 \rightarrow 3$) parton scattering process, and the real emission correction from all possible parton scattering processes with one extra QCD parton in the final state.

The single top-quark t-channel production can be calculated in five-flavour scheme or four-flavour scheme. These two approaches are equivalent if all orders in the perturbative expansion would be included. However, at low order the two predictions could differ substantially [43]. The advantage of five-flavour scheme is that in the calculation the logarithms of the form $ln((Q^2 + m_t^2)/m_b^2)$ are resummed into the b-quark parton density function which

18

improves the stability of the perturbative expansion. Also the NLO calculation starts from
$2 \rightarrow 2$ processes, which simplifies the calculation. The problem of this approach is that
the b-quark is only effectively described at leading order and in NLO level it enters as the
radiative contributions. This is not good for high-precision measurements which require the
distributions related to the spectator b should also be described at NLO accuracy. This
goal can be achieved by using the four-flavour scheme, which is the W-fusion production. In
this cross section calculation, the b quarks are considered to be massive quarks and do not
enter the evolution of the parton density functions and the running of the strong coupling.
One difficulty is that the terms related to $ln((Q^2 + m_t^2)/m_b^2)$ cause the perturbation series
to converge rather slowly [1], another difficulty is that the NLO calculation is much more
complex and time consuming due to the presence of an additional (massive) particle in the
final state.

The leading order calculation for single top-quark t-channel production is referred in [45].
Some recent studies provide the NLO corrections for single top-quark t-channel production[46,
47, 48, 49, 50]. Further accurate calculations for single top-quark production beyond
NLO includes higher-order corrections from Next-to-Leading-Logarithm (NLL) soft-gluon
resumption [51]. In this thesis, the predicted cross section of t-channel single top-quark
production is calculated at NLO in the 5-flavour scheme with Next-to-Next-to-Leading-
Logarithm (NNLL) resumption [20] $\sigma_t = 64, 57^{+2.71}_{-2.01}pb$ for $m_t = 172.5$ GeV. More cross
section results with different top-quark masses for t-channel production at the LHC can be
seen if Table 2.2.

$m_t($ GeV$)$	170	171	172	173	174	175
top-quark (pb)	42.9	42.5	42.1	41.7	41.4	41.0
antitop-quark (pb)	23.2	23.0	22.8	22.5	22.3	22.1

Table 2.2: The NNLO approx cross sections of single top-quark and antitop-quark t-channel
productions at the LHC with $\sqrt{s} = 7$ TeV [20].

2. **Single top-quark s-channel and Wt channel processes**
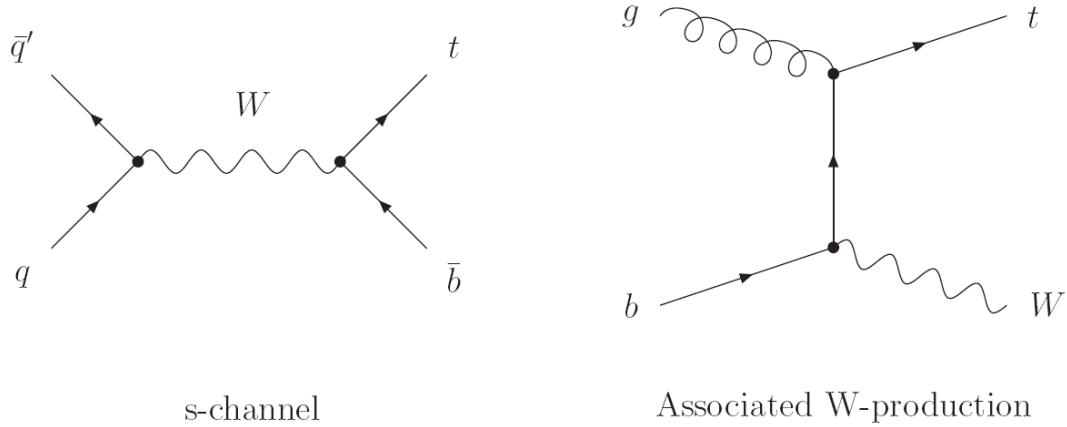
Figure 2.5: Leading order Feynman diagrams for single top-quark s-channel and Wt channel production.

Single top-quark s-channel process is a Drell-Yan type process where quark and antiquark annihilate into a time like virtual W boson. LO Feynman diagram of s-channel is shown on the left of Figure 2.5. s-channel have the smallest contribution to single top-quark production at the LHC, while it is the second largest process at the Tevatron. The dominant parton process in s-channel is $u\bar{d} \to \bar{b}t$. In this thesis, the cross section prediction of s channel is 4.6 ± 0.2 pb [52], from the NLO calculation with NNLL corrections.

Single top-quark Wt channel process is also called W associated single top-quark production. As shown on the right of Figure 2.5, a b-quark and a gluon create an on-shell W boson along with a top quark. At the LHC, Wt channel single top-quark production has a cross section 15.7 ± 1.1 pb [53]. While at the Tevatron, Wt production is negligible.

2.3.2 Top-quark Decay

As discussed in Section 2.2, the probability of a quark i decay into j is proportional to the square of CKM matrix element $|V_{i}j|$. Utilizing the unitarity of CKM matrix and assuming three quark generations only, the $|V_{tb}|$ is between 0.9990 and 0.9992 at 90% Confidence Level [54]. This means that top quarks almost fully decay into a b-quark and a W boson

with other decay modes neglectable. Then the top-quark decay final states can be easily identified by the W boson decays:

$$BR(W \to e\nu) : BR(W \to \mu\nu) : BR(W \to \tau\nu) : BR(W \to jets) = 1 : 1 : 1 : 6.$$

In top-quark pair production, if the two W-bosons originated from top-quark decay leptonically to leptons e, μ or τ, it is referred as dilepton channel. If one W boson decay leptonically and the other decay to jets, this process is called single lepton channel or lepton+jets channel. If two W-bosons all decay hadronically to jets, this process is referred as all hadronic channel. The single top-quark t-channel production can also be identified as lepton+jets channel and hadronic channel according the W boson originated from top-quark decay leptonically or hadronically.

With first order QCD corrections and some approximation, the top-quark decay width is given by [55, 56]

$$\Gamma_t = \frac{G_F m_t^3}{8\pi\sqrt{2}}(1 - \frac{m_W^2}{m_t^2})(1 + 2\frac{m_W^2}{m_t^2})[1 - \frac{3\alpha_s}{3\pi}(\frac{2\pi^2}{3} - 2.5)] \tag{2.26}$$

With given constants α_s and G_F, the decay width of top quark is calculated to be $\Gamma_t \simeq 1.4$ GeV with m_t around 170 GeV while corresponding life time of top quark is $\tau_t = 1/\Gamma_t \approx 5 \times 10^{-25} s$. It is shorter than the top-quark hadronization time 3×10^{-24}. As a consequence, the top quark decays before it can form hadrons. The top-quark spin "survives" non-perturbative QCD and it can be studied with the angular distributions of the final state particles in top-quark decay.

According to the SM, the weak decay of top quark follows a vector minus axial vector (V-A) structure and produces polarized W bosons. The W-boson helicity in top-quark decays is predicted to be 69.8% longitudinal polarized, 30.1% left-handed and 0.041% right-handed [57]. Any deviation between measurement results and expected values would indicate the existence of the new physics.

The top quark could also decay into a charm quark or up quark via flavor-changing neutral currents (FCNC) decays. These are highly suppressed in the Standard Model to branching ratios $\sim 10^{-9}$ or smaller. The huge top-quark samples at the LHC make it possible to test the predictions of these rare processes.

2.3.3   Cross Section Measurements of Top-quark Production

With the full Tevatron Run II samples and the increased integral luminosity of data from the LHC in 2011, we could expand our knowledge on the properties of the top quark. The published results of the Tevatron and LHC show a picture of the top quark that corresponds closely to the one predicted by the SM. In this part, the current top-quark production cross section measurement results are introduced.

Results of Top-quark Pair Production Cross Section Measurement

The cross section measurements of the $t\bar{t}$ production are good tests of perturbative QCD. For the time being, the published most precise cross section measurement of the $t\bar{t}$ production comes from Tevatron $\sigma_{t\bar{t}} = 7.70 \pm 0.52pb$ [58] with NLO prediction $\sigma_{t\bar{t}}^{NLO} = 7.5 \pm 0.7pb$ [59]. It is extracted from a measurement of the ratio $R = \sigma_{t\bar{t}}/\sigma_Z$. The relative total uncertainty of this measurement is $\sim 7\%$, exceeding the theoretical prediction with uncertainty $\sim 9\%$. The latest results from LHC with high-statistics samples and new NNLO theoretical calculation could help to identify possible new physic.

The published results of $t\bar{t}$ cross section measurements from CMS and ATLAS experiment at the LHC are listed in table 2.3. All measured $\sigma_{t\bar{t}}$ assume a top-quark mass of 172.5 GeV. These results used the early data collected in 2010.

Channel	Experiment	$\mathcal{L}_{integral}(pb^{-1})$	$\sigma_{t\bar{t}}(pb)$
l+jets - kinematics only	CMS	36	$173^{+39}_{-32}(stat. + syst.) \pm 7(lumi)$
l+jets - with b-tagging	CMS	36	$150 \pm 9(stat.) \pm 17(syst.) \pm 6(lumi)$
dilepton	CMS	36	$168 \pm 18(stat.) \pm 14(syst.) \pm 7(lumi)$
dilepton	ATLAS	35	$171 \pm 20(stat.) \pm 14(syst.)^{+8}_{-6}(lumi)$

Table 2.3: The published LHC results on the $t\bar{t}$ production cross section [60, 61, 62, 63].

The results at the LHC using the full statistics of 2011 data are still preliminary. Figure 2.6 shows some of these preliminary results..
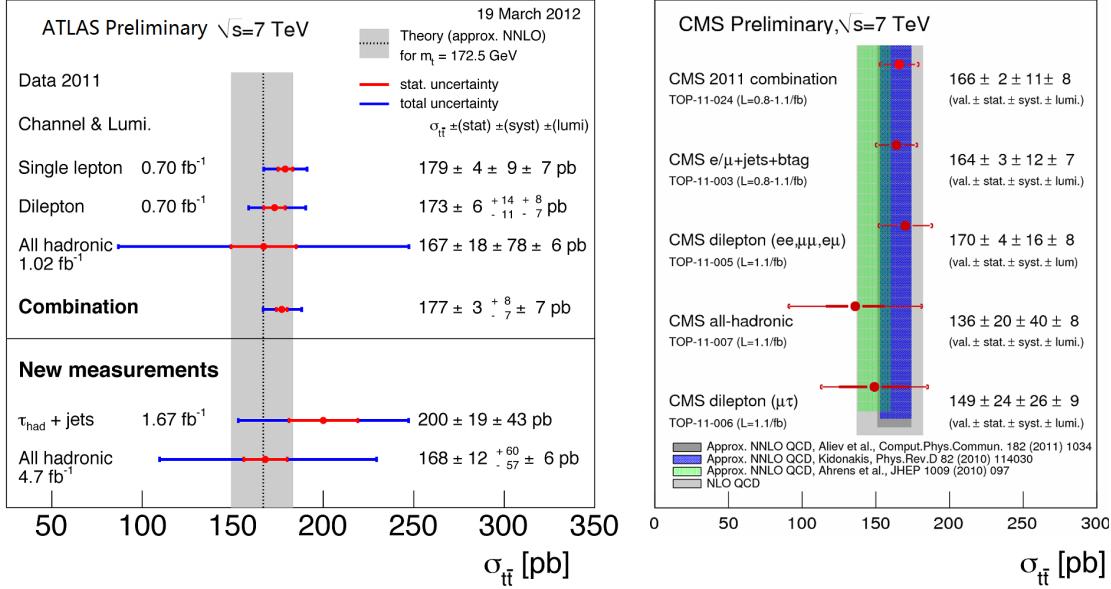
Figure 2.6: Preliminary results on top-quark pair cross section measurement from ATLAS and CMS experiment at the LHC [2, 3]. The vertical band are the predicted cross section from approximate NNLO calculation [4, 5, 6, 7].

Single Top-quark Production Cross Section Measurement

The studies on single top-quark production help us to learn the charged-current weak interactions of the top quark. The measurements of the single top-quark production cross section lead to a direct determination of the CKM matrix element V_{tb}, which could be used to test the unitarity of the CKM matrix. The single top-quark production cross section also probes the bottom-quark density distribution inside the proton, which at the moment is computed from light parton densities rather than extracted from data. Furthermore, single top-quark production rates can be significantly modified by new-physics interactions, such as heavy resonances or non-standard flavor-changing vertices [64]. In addition, the single top-quark processes contribute as backgrounds to many possible new-physics processes. For example, single top-quark t-channel process leads to the same final states as the Higgs boson associated production $WH \to Wb\bar{b}$. The precise understanding of single top-quark production would help to search for these new physics. Because of these reasons, the cross section

measurement of single top-quark production has been very interesting and very important in the high energy physics studies.

The single top-quark production was first observed by CDF [65] and D0 [66] experiment at the Tevatron in 2009. The results from CDF and D0 are combined to a measured cross section of

$$\sigma_{s-channel+t-channel} = 2.76^{+0.58}_{-0.47}(stat+syst)pb \tag{2.27}$$

in $p\bar{p}$ collisions at $\sqrt{s} = 1.96$ TeV with $m_t = 170$ GeV , which is consistent with the Standard Model expectation $2.26 \pm 0.12pb$ [67]. The CKM matrix element is extracted $|V_{tb}| = 0.88 \pm 0.07$ with a 95% Confidence Level lower limit of $|V_{tb}| > 0.77$ [68].

The single top-quark t-channel production are also measured independently by D0 group at the Tevatron [22] with $p\bar{p}$ collisions at $\sqrt{s} = 1.96$ TeV, which up to date gives the most precise measurement of t-channel single top-quark production cross section

$$\sigma(p\bar{p} \to tqb + X) = 2.90 \pm 0.59(stat+syst)pb \tag{2.28}$$

for a top-quark mass $m_t = 172.5$ GeV.

For the single top-quark Wt channel, the production cross section at the Tevatron is negligibly small. Thus the observation of this process relies on the LHC experiment.

The ATLAS and CMS experiments at the LHC have made many progresses in the studies on single top-quark production. The results are still preliminary and some of them are discussed in the Chapter 7.

Chapter 3

ACCELERATOR, DETECTOR AND OBJECT RECONSTRUCTION

The Large Hadron Collier could produce 80 million pairs of top quarks and an additional 34 million single top-quarks annually at the designed high luminosity. It is indeed a top-quark factory and thus plays an important role for top-quark study. The work in this thesis is based on the data collected in 2011 by ATLAS detector at the LHC with proton-proton (pp) collisions at a center-of-mass energy $\sqrt{s} = 7$ TeV.

This chapter first introduces the LHC accelerator and its running. Then a detailed introduction of the ATLAS detector and its components is described. The third part of this chapter gives the reconstructions of the particles and some definitions which will be used in the following analysis. The luminosity measurement in ATLAS and the data distribution are briefly introduced in last sections.

3.1 Large Hadron Collider

The Large Hadron Collider [69] is a superconducting particle accelerator, located from 50 to 175 meters beneath the surface at CERN, about 20 kilometers from Geneva center. It is nowadays the world's largest and highest-energy particle accelerator and the most powerful particle smasher. The LHC is an international project jointed by thousands of scientists from hundreds of countries all over the world. The purpose of the LHC is to increase our knowledge about the origin of the universe and the origin of matters. It is used to recreate the conditions and energies present immediately after the big bang, with the hope of discovering how our universe came into existence. It helps the scientists to look for these particles existing in some theory but have never been observed, particularly for the hypothesized Higgs boson(s) and the large family of new particles predicted by supersymmetry. It is expected to address some fundamental questions of physics, such as the nature of dark matter, origin of the baryon asymmetry, sources of CP violation, and the organizing principles for flavor physics.

CERN's accelerator complex includes particle accelerators and colliders, can handle beams of electrons, positrons, protons, antiprotons, and "heavy ions" (the nuclei of atoms, such as oxygen, sulphur, and lead). A global view of CERN accelerator complex is show in Figure 3.1 [8]. The LHC program is mainly based on proton-proton collisions, while in shorter running periods the heavy-ion and light-ion collisions are proceeded as well. Below the acceleration chain of protons and lead ions are briefly described. Then the experiments installed at the LHC and the current status of the LHC operation are introduced.

3.1.1 The Acceleration Chain and Designed Parameters of the LHC

Protons are obtained by removing electrons from hydrogen atoms. At first they are injected from the linear accelerator (LINAC2) to Proton Synchrotron Booster (PSB) to be accelerated to 1.4 GeV. Then they are boosted by Proton Synchrotron (PS) to the energy of 26 GeV. These protons are further accelerated by the CERN's second biggest accelerator Super Proton Synchrotron (SPS) to increase their energy to 450 GeV. Finally, the protons will be introduced into LHC's 27 kilometers circumference underground tunnel and be
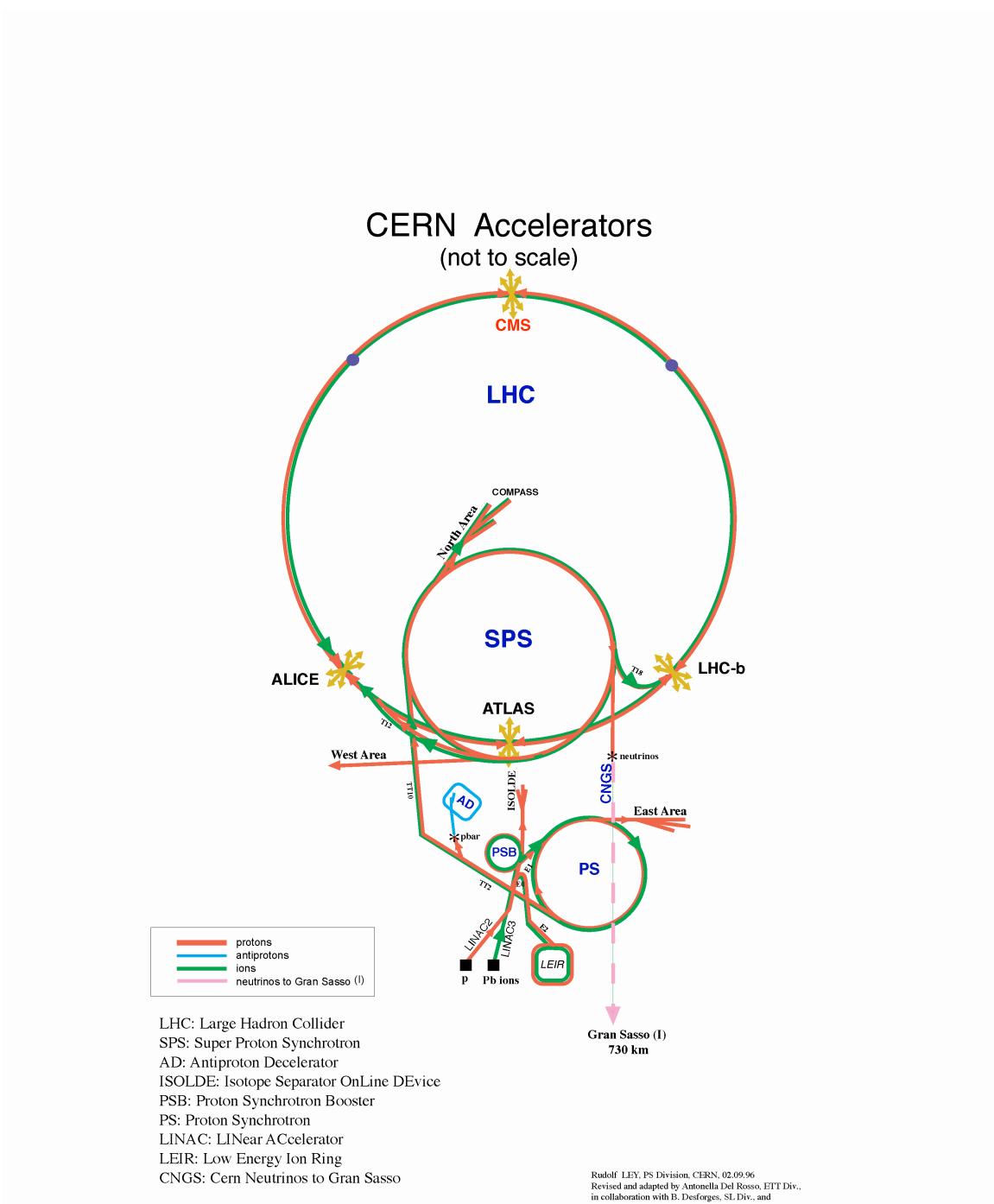
Figure 3.1: The CERN Accelerator Complex [8].

accelerated to the colliding energy.

The lead ions are generated from a source of vaporized lead. They are injected from LINAC3 to Low Energy Iron Ring (LEIR) to be accelerated. Then they follow the same route to reach maximum acceleration as the protons.

The LHC carries two beams, one clockwise and the other counter-clockwise. For the proton-proton collision, as designed, one beam consists of 2808 bunches, with over 10^{11} protons in each bunch. The two beams are circulating in separate magnet fields and vacuum chambers in the main arcs of the LHC, within one ring of magnets which consist of two sets of coils to create different magnet fields for the two beams. The two beams collide at the insertion regions (IRs) in the common sections of the two beam, where the experimental detectors are located. The maximum beam energy that can be reached in the LHC is limited by the peak dipole field in the storage ring. To bend 7 TeV protons around the ring, it requires a dipole field of 8.33 Tesla, which is generated by the superconducting dipole magnets. The beam are focused by the quadrupole magnets. Strong focusing power of the quadrupole could limit the bean size to be small and ensure a high event rate at the collision point. The event rate R for a physics process with cross-section σ is proportional to the instantaneous luminosity L:

$$R = L\sigma. \tag{3.1}$$

With n_1 and n_2 protons per bunch for the two beams, and n_b bunches in one beam, an approximate calculation of the luminosity L is given by [70]:

$$L = f_r \frac{n_b n_1 n_2}{2\pi \Sigma_x \Sigma_y}. \tag{3.2}$$

Here f_r is the revolution frequency of the LHC machine, $\Sigma_x \Sigma_y$ characterize the beam size and can be expressed as $\Sigma_x \Sigma_y = \epsilon_n \beta^*$, where ϵ_n is the normalized transverse beam emittance and β^* is the beta function which characterizes the beam optics. The total number of events for a process is obtained by integrating the event rate R with time t,

$$N_{event} = \int R dt = \mathcal{L}\sigma, \text{ with } \mathcal{L} = \int L dt. \tag{3.3}$$

Instead of the total event number, the integrated luminosity $\mathcal{L}$ is often used to refer the collected data size. The LHC is designed for very high instantaneous luminosity to ensure

a high event rate even for those physics processes with small cross sections. Table 3.1 lists some designed beam parameters of the LHC.

Beam parameters	value	Beam parameters	value
Proton Injection Energy	450 GeV	Peak Luminosity	$10^{34}\text{cm}^{-2}\text{s}^{-1}$
Proton Beam Energy	7 TeV	β^*	0.55m
Particles per Bunch	1.15×10^{11}	Normalized Transverse Emittance	$3.75\mu\text{m}$
Number of Bunches	2808	Energy Loss per Turn	6.7KeV
Bunch Spacing	25ns	Peak Dipole Magnet Field	8.33T
Bunch Length	7.5cm	Peak Quadrupole Magnet Field	6.85T
Circulating Current	0.584A	Total Cross Section	100pb
Stored Energy	362MJ	Inelastic Cross Section	60pb

Table 3.1: LHC designed beam parameters [70]

3.1.2 The Experiments Installed at the LHC

As shown in 3.1, there are four main detectors installed at the four interaction points (IP) of the LHC: the ATLAS (IP1), CMS (IP5), LHCb (IP8) and ALICE (IP2) detectors [10] [71] [72] [73]. Another two small experiments LHCf [74] and TOTEM [75] are installed on the LHC accelerator ring near the ATLAS region and the CMS region separately.

- ATLAS (**A T**oroidal LHC **A**pparatu**S**) and CMS (**C**ompact **M**uon **S**olenoid) are two general purpose detectors designed to investigate a wide range of physics, including the search for Higgs boson, supersymmetry particles, dark matters and extra dimensions. Both of them consist of four concentric subsystems: the inner detector, electromagnetic calorimeter, hadronic calorimeter and muon detector. The CMS has a single magnet surrounding the inner detector and calorimeters with large magnet field of 3.8T, and its muon chambers are in return yoke. This is different comparing to the ATLAS detector as introduced in Section 3.2. The different designs of the ATLAS and

CMS detectors result in different capabilities of identifying and measuring particles, which give rather different systematic uncertainties in the measurements. This way they provide an independent cross-check measurement for each other.

- LHCb (**L**arge **H**adron **C**ollider **b**eauty) is a forward single arm spectrometer which uses a series of sub-detectors to detect mainly forward particles. It is dedicated to the study of the CP violating effects, phenomena in the decays of the b hadrons (hadrons containing b quark).

- ALICE (**A L**arge **I**on **C**ollider **E**xperiment) is a dedicated heavy-ion detector used to study nucleus-nucleus interactions at LHC energies. The collisions in ALICE generate high temperature and large energy density, which could create a state of matter called quark-gluon plasma. The existence of such a phase and its properties are important to understand the confinement and of chiral-symmetry in QCD.

- LHCf (**L**arge **H**adron **C**ollider **f**orward) is the smallest one of the six official LHC experiments, consisting two detectors located on either side of the ATLAS experiment. It studies the neutral-particle production cross sections in the very forward region of proton-proton and nucleus-nucleus interactions, helping to understand the development of atmospheric showers induced by very high energy cosmic rays.

- TOTEM (**TOT**al **E**lastic and diffractive cross section **M**easurement) is installed near the point where protons collide in the center of the CMS detector. It studies forward particles that are very close to the LHC beams, dedicated to the precise measurement of the proton-proton interaction cross section with the luminosity independent method and to the study of elastic and diffractive scattering at the LHC.

3.1.3 *Status of the LHC Operation*

In November 2009, the proton beams were successfully circulated in the main ring of the LHC, and first data at the center-of-mass energy of 900 GeV were recorded. With the luminosity around $10^{27} cm^{-2} s^{-1}$, about 1.5 million events were collected. On 30 March

2010, the LHC started the proton-proton collisions at the center-of-mass energy of 7 TeV. The numbers of protons per bunch increased from 5×10^{10} to 1.2×10^{11}, which exceeded the designed parameter. And the highest instantaneous luminosity in 2010 reached $2 \times 10^{32} cm^{-2} s^{-1}$. Till the end of October 2010, the integrated luminosity of $48pb^{-1}$ proton-proton collisions were collected. And $48\mu b^{-1}$ of heavy ion collision data were collected in the following 4 weeks at center-of mass energy 2.76 TeV.

In 2011, the LHC was steadily running at 7 TeV center-of-mass energy with instantaneous luminosity above $10^{33} cm^{-2} s^{-1}$. From March to October 2011, The LHC delivered $5.63fb^{-1}$ data for ATLAS and $5.7fb^{-1}$ for CMS, as shown in Figure 3.2. And starting from November, heavy ion collisions were proceeded for more than three weeks at center-of mass energy 2.76 TeV. The performance of the LHC machine in 2011 has been outstanding, delivering integrated luminosities beyond the expectations for both the proton-proton and Pb-ion runs. Some performance like particles per bunch and normalized transverse emittance have exceeded the designed value. The beam parameters in 2011 LHC operation can be referred in Table 3.2 [9].

In 2012, the LHC has started its run from April and it is operating at 4 TeV beam energy. The performance of LHC will be increased step by step during the operation procedure in 2012. Some current beam parameters of the LHC run in April as well as the expected values in 2012 are shown in Table 3.2 [76] [77]. After 2012 run, the LHC will shutdown for about 20 months for upgrades to allow full energy operation (7 TeV per beam).
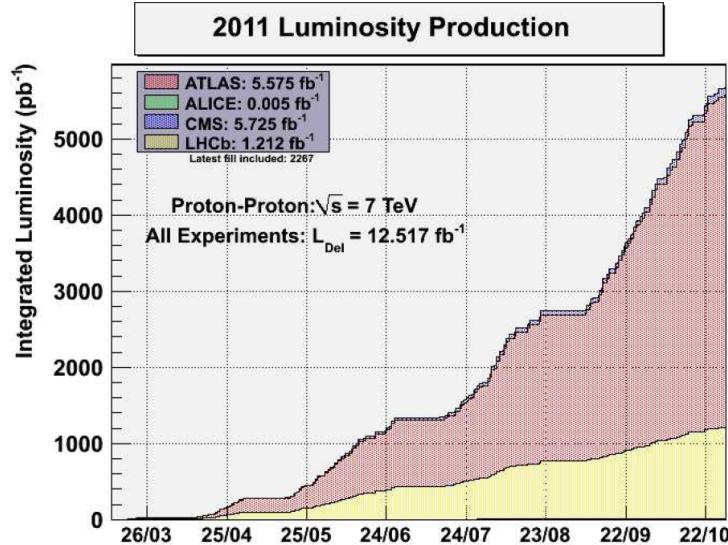
Figure 3.2: Luminosity integrated by experiments in 2011 [9].

Beam parameters	2011	2012 April	2012 plan
Peak luminosity ($\times 10^{33} \text{cm}^{-2}\text{s}^{-1}$)	3.6	4.2	5-6.8
Proton Beam Energy (TeV)	3.5	4	4
Number of Bunches	1380	1092	1380
Particles per Bunch ($\times 10^{11}$)	1.5	-	1.6
Bunch Spacing (ns)	50	50	50
Normalized Transverse Emittance (μm)	1.9-2.3	-	2
β^* (m)	1	0.6	0.6-0.9

Table 3.2: LHC beam parameters in 2011 and 2012 operation and the expected value in 2012 [9] [76] [77]

.
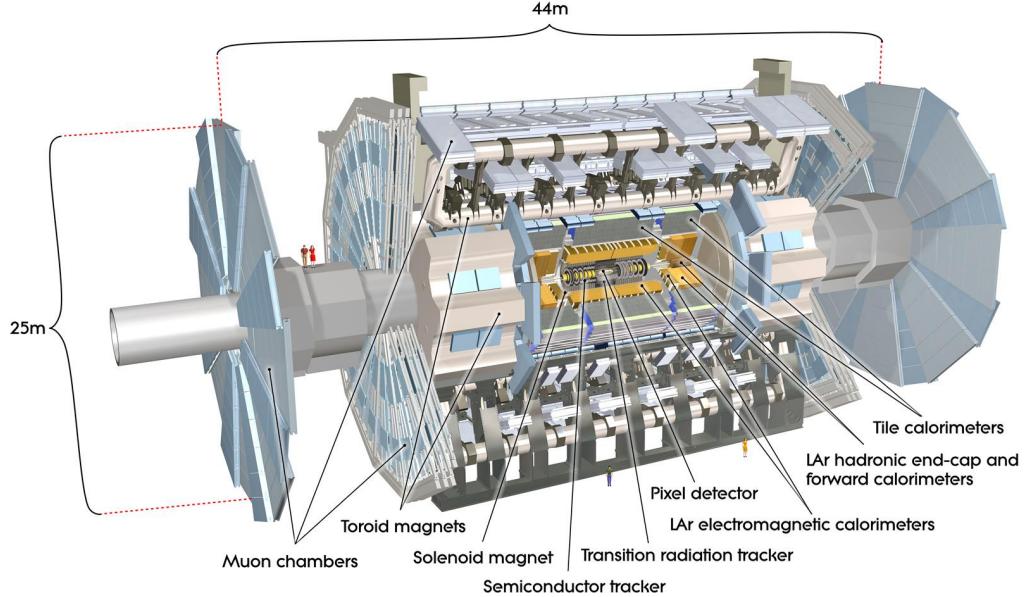
Figure 3.3: The construction of the ATLAS detector [10].

3.2 ATLAS Detector

The ATLAS experiment is one of the two general purpose experiment at the LHC. It is designed to measure the electroweak interactions, search for Higgs boson and new physics, study extra dimensions of space and dark matters. The ATLAS detector is 25m in height and 44m in length, weighting about 7000 tons. It is composed by four main sub-systems: the magnet system, the inner detector, the calorimeter and the muon spectrometer. An overall ATLAS detector layout is shown is Figure 3.3 [10].

The coordinate system and nomenclature used in ATLAS experiment are briefly described here. The z-axis is the beam direction while x-y plane is transverse to the beam direction. x-axis is defined as the direction pointing from the interaction point to the center of the LHC ring and y-axis is pointing upwards. ϕ refers to the azimuthal angle in x-y plane, range $[-\pi, \pi]$. θ is the polar angle from the z-axis. η is called pseudorapidity which is calculated from θ:

$$\eta = -ln[\tan(\frac{\theta}{2})].$$

The distance in the pseudorapidity-azimuthal angle space is defined as:

$$\Delta R = \sqrt{(\Delta \eta)^2 + (\Delta \phi)^2}.$$

To reach its physics goal, the ATLAS detector is required to have fast electronics and sensor elements, large acceptance in pseudorapidity, good momentum resolution and particle reconstruction efficiency, precise measurements of the energy and high efficiency triggers. The main performance goals of the ATLAS detector are listed in Table 3.3 [10].

Detector Component	Required Resolution	η Coverage	
		Measurement	Trigger
Tracking	$\sigma_{p_T}/p_T = 0.05\% p_T \oplus 1\%$	± 2.5	
EM calorimetry	$\sigma_E/E = 10\%/\sqrt{E} \oplus 0.7\%$	± 3.2	± 2.5
Hadronic calorimetry			
barrel and end-cap	$\sigma_E/E = 50\%/\sqrt{E} \oplus 3\%$	± 3.2	± 3.2
forward	$\sigma_E/E = 100\%/\sqrt{E} \oplus 10\%$	$3.1 < |\eta| < 4.9$	$3.1 < |\eta| < 4.9$
Muon spectrometer	$\sigma_{p_T}/p_T = 10\%$ at p_T=1TeV	± 2.7	± 2.4

Table 3.3: General performance goals of the ATLAS detector [10]. The units for E and p_T are in GeV.

3.2.1 Magnet System

The magnet system of ATLAS detector consists of a central solenoid (CS), one barrel toroid (BT) and two end-cap toroids (ECT). It is 22 m in diameter and 26 m in length. The positions of these four magnet system in ATLAS detector can be seen in Figure 3.3.

The central solenoid is placed outside the inner detector and before the electromagnetic calorimeter [78]. It is aligned with the beam axis and provides a 2 T axial magnetic field for the inner detector. The position of the central solenoid requires it to be as thin as possible to reduce its effects on the particles before they reach the calorimeter. The parameters for all the four magnet systems are shown in Table 3.4 [10].

Property	Feature	Unit	Solenoid	Barrel toroid	Endcap toroid
Size	Inner diameter	m	2.46	9.4	1.65
	Outer diameter	m	2.56	20.1	10.7
	Axial length	m	5.8	25.3	5.0
	Number of coils		1	8	2×8
Mass	Conductor	t	3.8	118	2×20.5
	Cold mass	t	5.4	370	2×140
	Total assembly	t	5.7	830	2×239
Coils	Turns per coil		1154	120	116
	Nominal current	kA	7.73	20.5	20.5
	Magnet stored energy	GJ	0.04	1.08	2×0.25
	Peak field in the windings	T	2.6	3.9	4.1
	Field range in the bore	T	0.9-2.0	0.2-2.5	0.2-3.5
Conductor	Overall size	mm^2	30 x 4.25	57 x 12	41 x 12
	Ratio Al:Cu:NbTi		15.6:0.9:1	28:1.3:1	19:1.3:1
	Number of strands(NbTi)		12	38-40	40
	Strand diameter(NbTi)	mm	1.22	1.3	1.3
	Critical current(at 5T and 4.2k)	kA	20.4	58	60
	Operatingcritical-current ratio at 4.5K	%	20	30	30
	Residual resistivity ratio(RRR) for Al		> 500	> 800	> 800
	Temperature margin	K	2.7	1.9	1.9
	Number of units $\times$ length	m	4 x 2290	8x4x1730	2x8x2x800
	Total length(produced)	km	10	56	2 x 13
Heat load	At 4.5 K	W	130	990	330
	At 60-80 K	kW	0.5	7.4	1.7
	Liquid helium mass flow	g/s	7	410	280

Table 3.4: The main parameters for the magnet system [10].

The barrel toroid is composed by 8 coils assembled radially and symmetrically around the beam axis [79]. It generates a magnetic field 3.9 T (peak value) for the muon spectrometer. The two end-cap toroids are similar as the barrel toroid but inserted in the two ends to ensure a full range bending power. They provide a peak magnetic field 4.1 T for the muon spectrometer [80]. Figure 3.4 shows the 8 coils of the barrel toroid during the setup of the ATLAS detector [10].
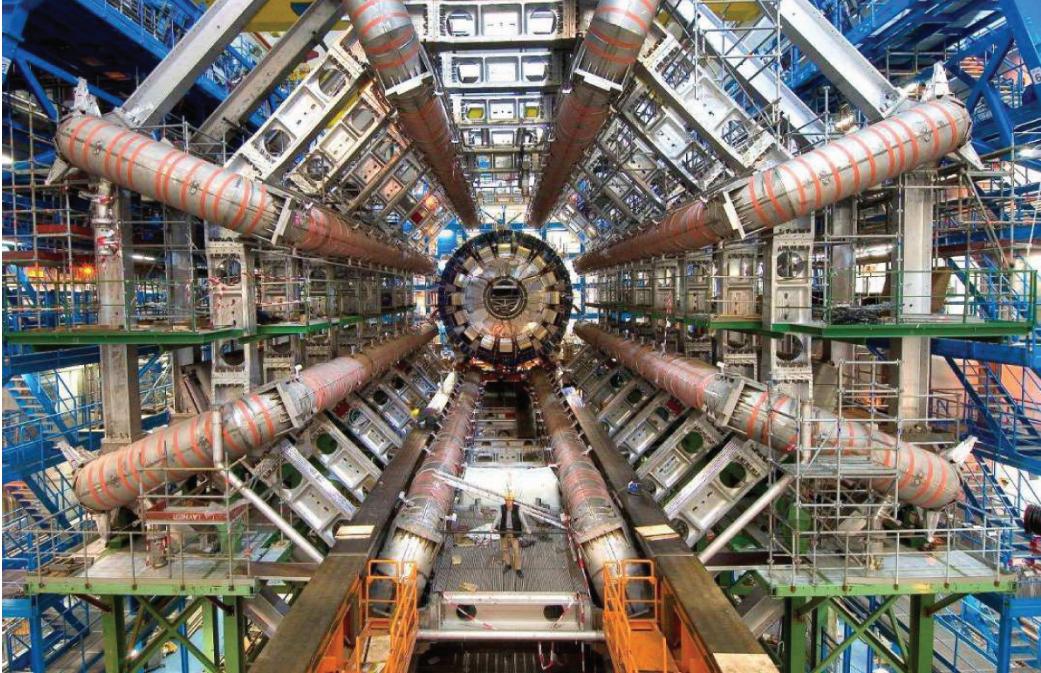
Figure 3.4: The barrel toroid in ATLAS detector [10].

3.2.2 Inner Detector

The ATLAS Inner Detector (ID) is the detector closest to the beam pipe. It is designed to provide highly efficient track reconstruction, excellent momentum resolution and a good measurement of the primary and secondary vertices for the charged tracks. The inner detector is about 7 meters long and of radius 1.15 m, located within the 2 Tesla solenoidal magnetic field. It covers the pseudorapidity range $|\eta| < 2.5$. The inner detector is composed by three independent but complementary sub-detectors, the Pixels, Semi-Conductor Tracker (SCT) and the transition radiation tracker (TRT). An overview of the inner detector is shown in Figure 3.5 [10]. while the basic overall parameters are summarized in Table 3.5 [10].

The pixel detector has very good position recognition capability of charged particles due to its highly modular, containing approximately 1500 barrel modules and 700 disk modules. It consists of three barrel layer and three disks in two end-caps. All the layers contain 140 million detector elements in total. The size of each elements is $\Delta_{R-\phi} \times \Delta_z = 50\mu m \times 400\mu m$.
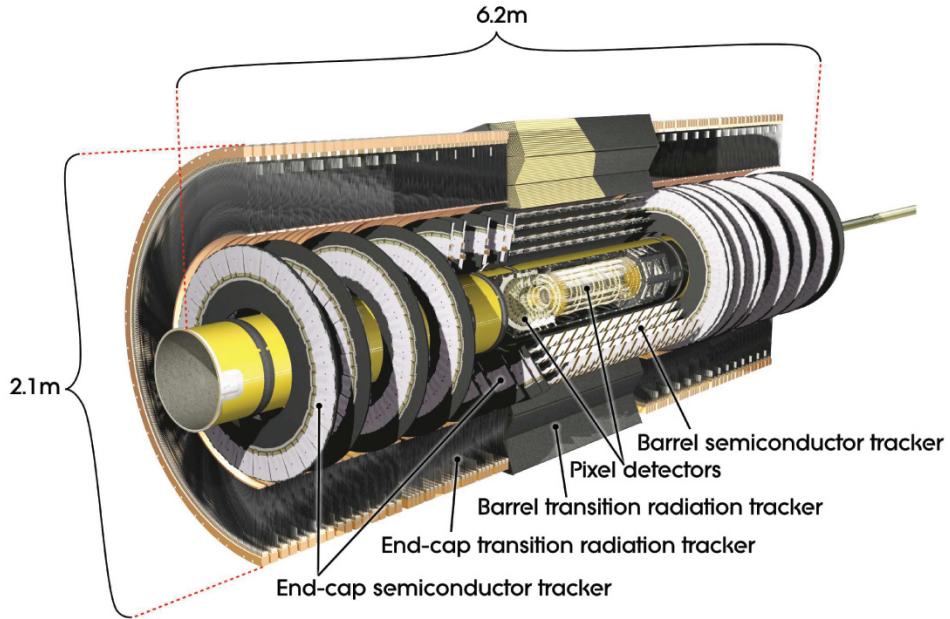
Figure 3.5: Overview of ATLAS inner detector [10]

	Item	Radial extension (mm)			Length (mm)		
Pixel		45.5	< R <	242	0	$<\mid z \mid<$	3092
SCT	(barrel)	255	< R <	549	0	$<\mid z \mid<$	805
	(end-cap)	251	< R <	610	810	$<\mid z \mid<$	2797
TRT	(barrel)	554	< R <	1082	0	$<\mid z \mid<$	780
	(end-cap)	617	< R <	1106	827	$<\mid z \mid<$	2744

Table 3.5: Main parameters of the ID overall envelope [10].

The resolution in $R - \phi$ plane can reach $10\mu m$ and in the z direction it is $115\mu m$.

The SCT also has quick electronic response and good pattern recognition capability. It provides additional momentum and position measurements for the tracks in the intermediate radial range. The SCT is composed of four barrel layers and two end-caps, each with nine wheels [81]. There are 4088 modules in SCT with each size $\Delta_{R-\phi} \times \Delta_z = 6.36cm \times 6.40cm$. The SCT covers acceptance range $|\eta| < 2.5$, with resolution $16\mu m$ in $R - \phi$ plane and $580\mu m$ in z direction.

The TRT system is based on the straw drift tubes with a diameter of 4 mm each. The TRT can operate at very high rates and gives a combined accurate measurement in $R - \phi$ plane with resolution better than $50\mu m$, due to its large number of straws. The TRT contains 73 layers of straws interleaved with fibres (barrel) and 160 straw planes interleaved with foils (end-cap) [82] [83]. The charged tracks with $p_T > 0.5$ GeV in range $|\eta| < 2.0$ traverse at least 36 straws, except in range $0.8 < |\eta| < 1.0$ the minimum number is 22 straws due to the barrel-end-cap transition. The TRT also provides the measurement of the transition radiation, which can be used to discriminate electrons from other charged particles.

3.2.3 Calorimeters

The calorimeters are used to detect and identify the electrons, photons, jets, and to measure their energies. In ATLAS detector, there are two parts of calorimeter, the electromagnetic calorimeter (EM) and the hadronic calorimeter [84] [85]. The electromagnetic calorimeter is close to the inner detector and consists of the electromagnetic barrel calorimeter ($|\eta| < 1.475$) and the electromagnetic end-cap calorimeter ($1.375 < |\eta| < 3.2$). The hadronic calorimeter is placed outside the electromagnetic calorimeter, composed of the tile calorimeter ($|\eta| < 1.7$), the hadronic end-cap calorimeter ($1.5 < |\eta| < 3.2$) and the forward calorimeter which is located closest to the beam and covers the range $3.1 < |\eta| < 4.9$. The overall calorimeter system is shown in Figure 3.6 [10].

In general, the calorimeter is made of the absorber and detection medium. The particles meet the absorber and produce secondary particles showers which are detected by the
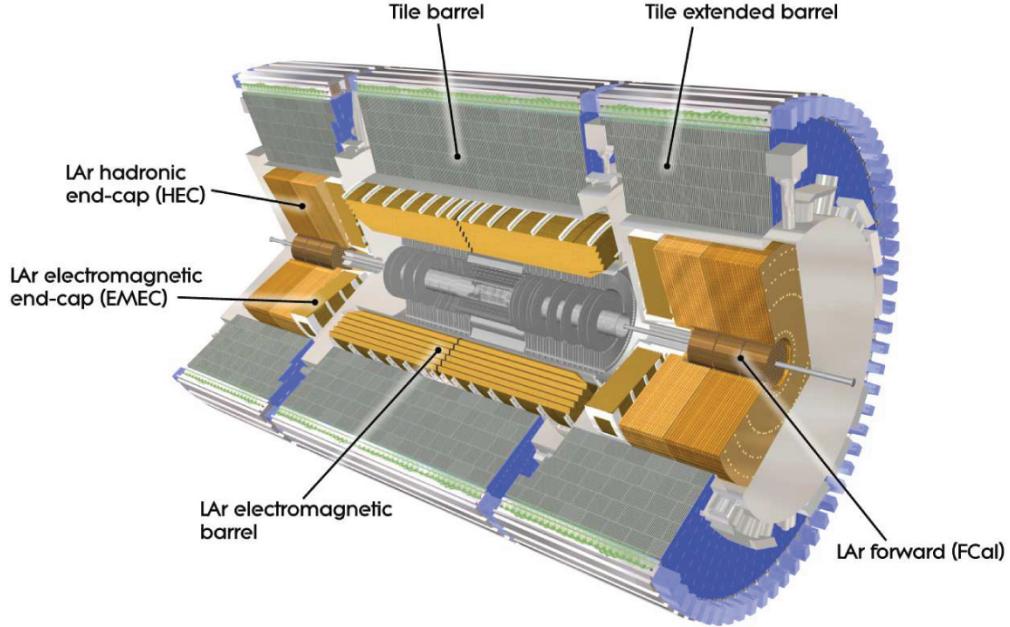
Figure 3.6: Overview of ATLAS Calorimeter [10]

detection medium. In ATLAS calorimeter, the electromagnetic calorimeter, the hadronic end-cap calorimeter and the forward calorimeter use lead as absorber and liquid argon as the active detection medium due to its intrinsic linear behavior, its stability of response over time and its intrinsic radiation-hardness. For the tile calorimeter, the iron is used as absorber and the plastic scintillator is used as the detection medium.

The cryostat systems is composed of one barrel cryostat and two end-cap cryostats. The barrel cryostat contains the electromagnetic barrel calorimeter. And the two end-cap cryostats contain the electromagnetic end-cap calorimeters, the hadronic end-cap calorimeters and the forward calorimeter.

Electromagnetic Calorimeter

The electromagnetic calorimeter uses the accordion shape absorbers and electrodes, providing a full coverage in ϕ without any cracks and a fast extraction of the signal at the rear or at the front of the electrodes [84]. The accordion waves are axial and run in ϕ in the barrel.

In the end-caps, the waves are parallel to the radial direction and run axially. To keep the liquid-argon gap constant, the folding angles of the waves vary with radius.

The barrel electromagnetic calorimeter consists of three layers with different granularity in the longitudinal direction, the first layer, the middle layer and the back layer. Figure 3.7 shows the barrel module and the granularity of the three layers [10]. The first layer is finely segmented along η, while less and less segmented in the middle layer and the back layer. Most of energy of electrons and photons will deposit in the middle layer, while the back layer collects only the tail of the electromagnetic shower. There is also a presampler in the region of $|\eta| < 1.8$, which is used to correct the energy loss of electromagnetic calorimeter.
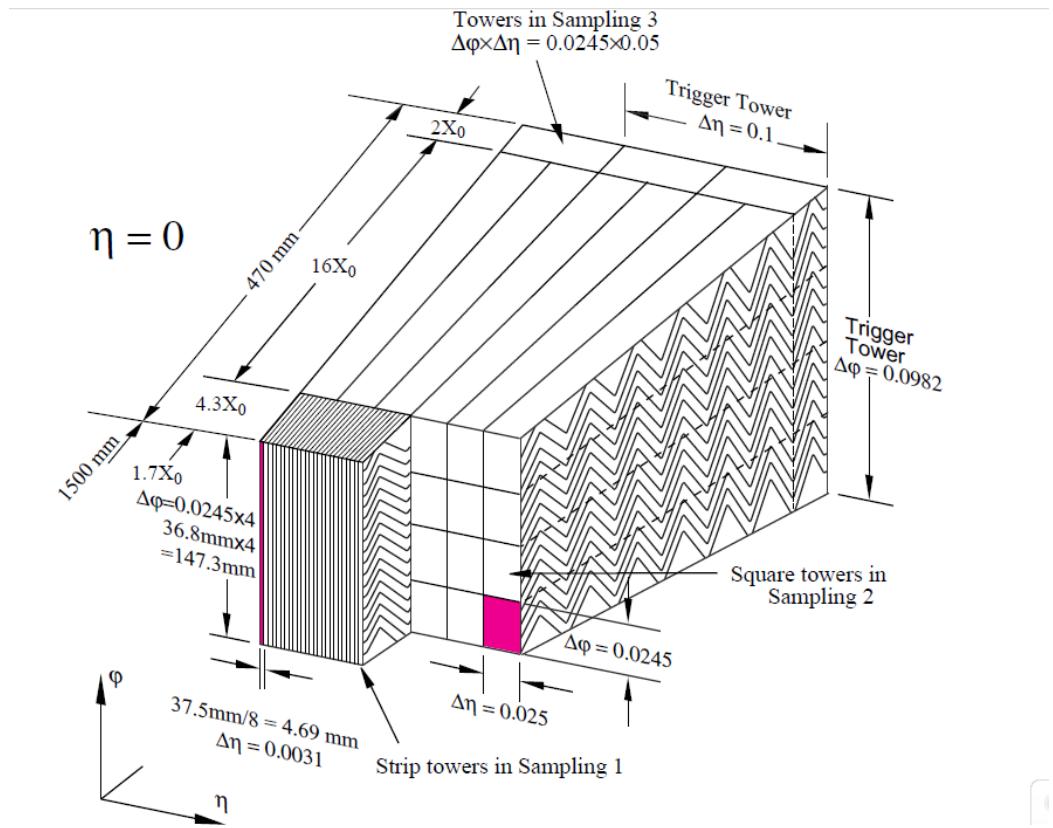
Figure 3.7: Sketch of a barrel module of the electromagnetic calorimeter [10]. The granularity in η and ϕ of the cells of each of the three layers and of the trigger towers is also shown.

The electromagnetic end-cap calorimeter has an inner wheel ($2.5 < |\eta| < 3.2$) and an

outer wheel ($1.375 < |\eta| < 2.5$). The region $1.5 < |\eta| < 1.8$ in end-cap calorimeter is also divided into three layer as the barrel electromagnetic calorimeter. The granularity for the middle cell in end-cap calorimeter is the same $\Delta\eta \times \Delta\phi = 0.025 \times 0.025$. And The presampler is used as well in the region of $1.5 < |\eta| < 1.8$.

Hadronic Calorimeters

The goal of the hadronic calorimeter is to measure the energy of hadrons with good resolution. It is required to be relatively thick to hold all hadronic showers and to reduce the leakage to the muon system.

The barrel hadronic calorimeter is also called tile calorimeter. It uses iron as absorber and scintillating tiles as the detection medium. It consists of a central barrel and two extended barrel calorimeters. The central tile calorimeter covers range $|\eta| < 1.0$ with 5.8 m in length and 7.4λ in radial depth, while the λ is the interaction length. The tile extended barrel calorimeters in the region $0.8 < |\eta| < 1.7$ have the inner radii 2.28 m and outer radii 4.25 m. The tile calorimeter is sampling calorimeter divided into three longitudinal layers. In the first two layers the granularity is $\Delta\eta \times \Delta\phi = 0.1 \times 0.1$ while in the third layer it is $\Delta\eta \times \Delta\phi = 0.1 \times 0.2$.

The hadronic end-cap calorimeters consist of two wheels, a front wheel and a rear wheel. Each wheel contains two longitudinal sections, with outer radii of 2.3 m. The end-cap calorimetry extends the pseudorapidity coverage of hadronic calorimeter to $|\eta| < 3.2$.

The forward calorimeter is placed about 4.7 m away from the interaction point, covering the region of $3.1 < |\eta| < 4.9$. As illustrated in Figure 3.8, the forward calorimeter is composed of one electromagnetic module and two hadronic modules [10]. The forward calorimeter provides a uniformity of the calorimetric coverage and limits the backgrounds reach to the muon spectrometer. It also brings challenge due to the exposure to high particle fluxes.
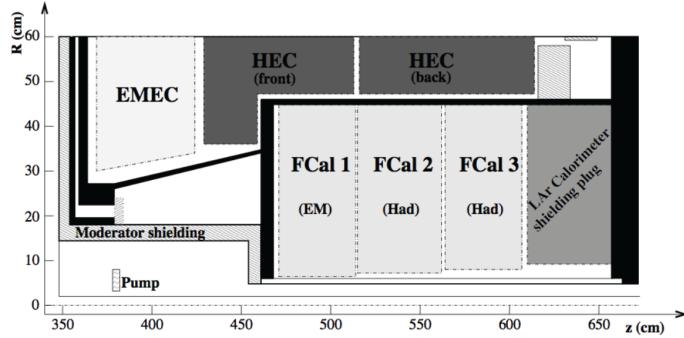
Figure 3.8: Layout of the forward calorimeter modules [10].

3.2.4 Muon Spectrometer

The muon spectrometer (MS) is designed to measure muons with good momentum resolution, high detection efficiency and large fake track rejection. It also serves as the trigger system to trigger on muons. The muon spectrometer is placed at the outermost of the ATLAS detector. It consists of four parts, the monitored drift tubes (MDT), resistive plate chambers (RPC), thin gap chambers (TGC) and cathode strip chambers (CSC) [86]. The layout out the muon spectrometer is shown in Figure 3.9 [10].

The Monitored Drift Tube chambers (MDT) provide the precision momentum measurement of the muons. It is located at the barrel and end-cap of the detector, covering a region of $|\eta| < 2.7$. The MDTs contain three to eight layers of drift tubes, operated with a non-flammable mixture of Argon and CO_2 at an absolute pressure of 3 bar. It can reach an average resolution of $80\mu m$ per tube, or about $35\mu m$ per chamber.

The Cathode Strip Chambers (CSC) are multi-wire proportional chambers with cathode strip readout and with a symmetric cell. They have higher granularity and can provide a better time resolution. Thus they are used in the innermost tracking layer in the forward region $2 < |\eta| < 2.7$. The resolution of a chamber in the bending plane can reach $40\mu m$ while in the transverse plane the resolution is about 5 mm.

While the MDTs and CSCs perform as the precision-tracking chambers, Resistive Plate Chambers (RPCs) and Thin Gap Chamber (TGCs) serve as the trigger chamber, another
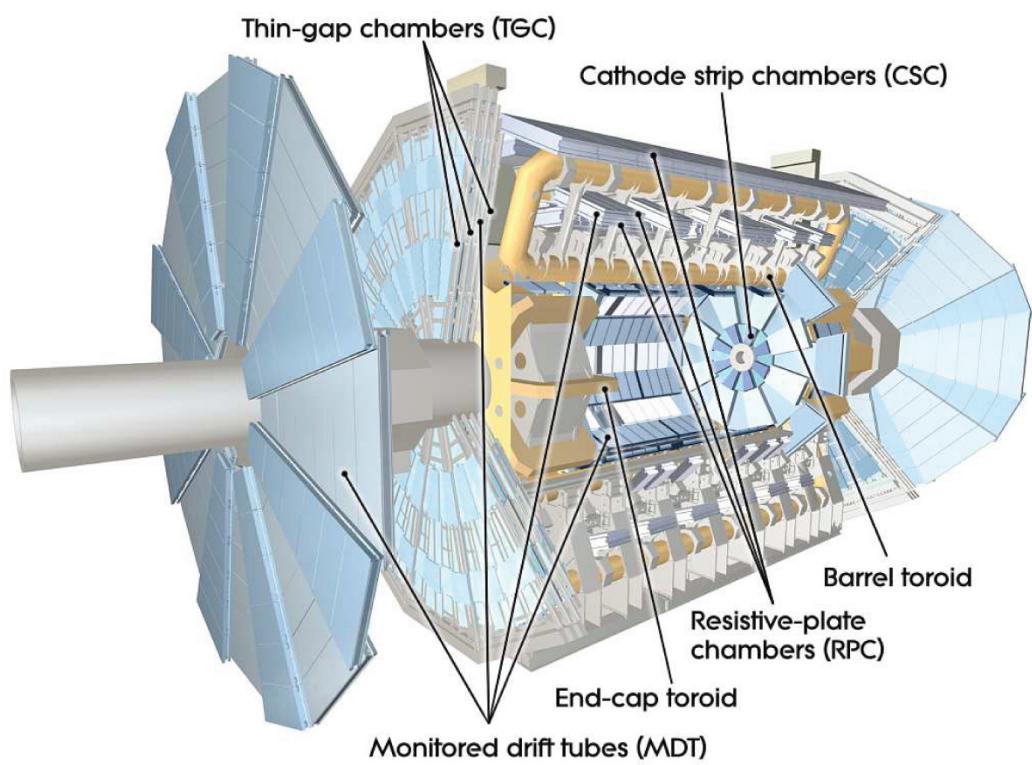
Figure 3.9: Overview of the muon system [10].

critical part of the muon system. The RPCs cover the barrel region $|\eta| < 1.05$. They are gaseous detectors with the gas mixture of $C_2H_2F_4$ and SF_6, providing a typical space-time resolution of $1cm \times 1ns$. The TGCs are multi wire proportional chambers with a graphite cathode, covering the end-cap region $1.05 < |\eta| < 2.4$. RPCs and TGCs are also used to provide second coordinate information for through going particles.

3.2.5   Trigger and Data Acquisition

As designed, at the LHC there are 40 millions of bunch crossing in one second with 23 collision events in each. It is impossible and not necessary to record all the events. The trigger system is used to reduce the event rates and to select the interesting events for physics analysis. In ATLAS, there are three level of triggers, the L1 trigger, the L2 trigger and the Event Filter (EF) trigger. The L2 trigger and the EF trigger are also called Hight Level Trigger (HLT). The overview of the trigger system is show in Figure 3.10 [10].

L1 trigger is a hardware based system. It selects the objects with a transverse momentum exceeding a certain threshold, including the sections for muons, electrons, photons, tau, jets, missing transverse energy $(E_T{}^{miss})$ and total transverse energy. The L1 trigger threshold of different candidates used in ATLAS in 2011 run are listed in Table 3.6. L1 trigger consists of three parts, the Calorimeter Trigger (L1Calo), the Muon Trigger (L1Muon) and the Central Trigger Processor (CTP). L1Calo uses the information from all the calorimeters with a reduced-granularity $\Delta\eta \times \Delta\phi = 0.1 \times 0.1$ to select high-energetic objects, while L1Muon uses RPC and TGC trigger chamber as introduced in Section 3.2.4 for the selection of the muons. The trigger selections are combined to a trigger "menu" by the CTP. One or more Regions-of-Interest (RoIs) are defined by L1 trigger, which is a $\Delta\eta \times \Delta\phi$ region of 0.4×0.4 for L1Calo and about 0.1×0.1 for L1Muon. L1 trigger reduces the event rate from 40 MHz to about 75 kHz within a fixed latency of less than 2.5 μs.

During the latency of the Level 1 trigger selection, the complete event data is kept in the pipeline memories of the sub-detector front-end electronics. Only the data selected by the L1 trigger are transferred to the Readout Drivers (RODs) and are stored temporarily in Readout Buffers (ROBs).
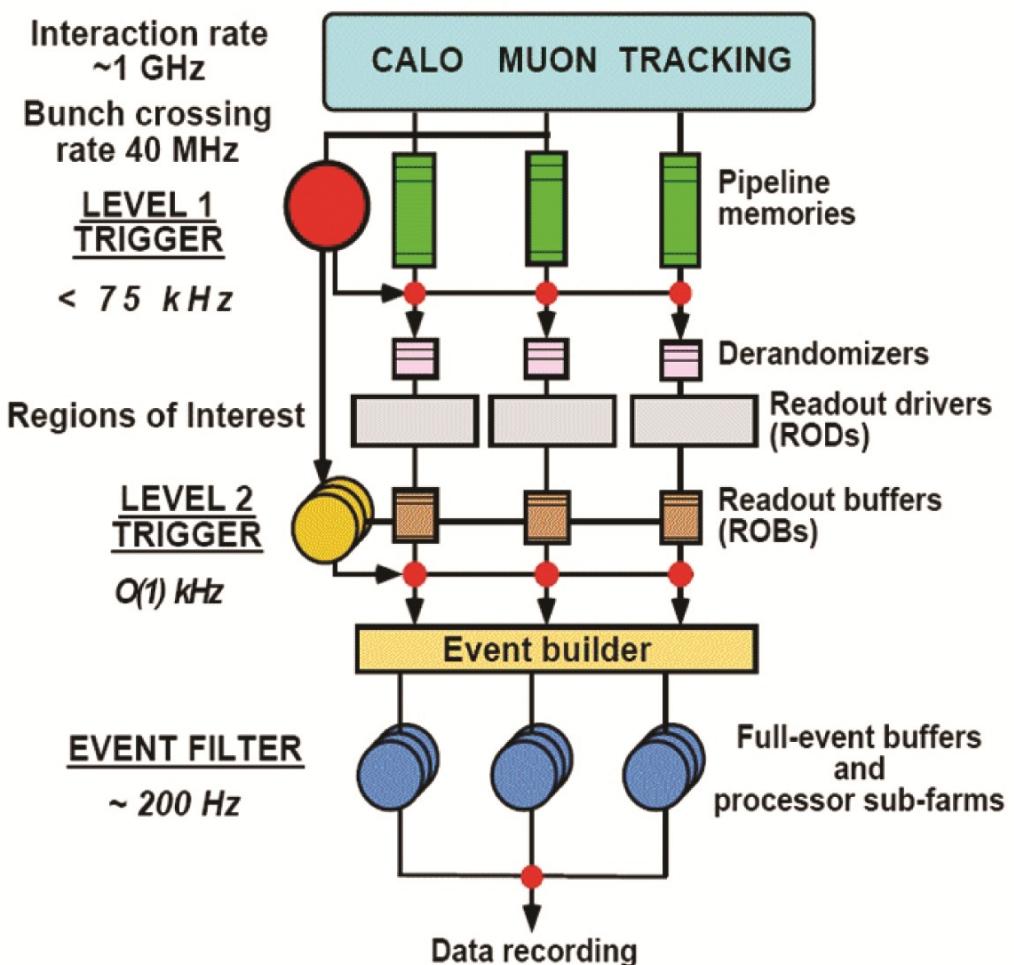
Figure 3.10: Overview of the trigger system [10].

Trigger Objects	Trigger Threshold		Event Rate	
	L1 (GeV)	EF (GeV)	L1 (kHz)	EF (Hz)
Single muon	11	18	8	100
Single electron	16	22	9	55
Two muons	11	15,10	6	5
Two electrons	10	12	2	1.3
Two taus	15,11	29,20	7.5	15
Two photons	12	20	3.5	5
$E_T{}^{miss}$	50	70	0.6	5
Multi-jets (5 jets)	10	30	0.2	9
Single jet plus $E_T{}^{miss}$	50,35	75,55	0.8	18
Total Rate			55	500

Table 3.6: Trigger threshold and rates of L1 trigger and EF trigger in ATLAS. The event rates corresponding peak luminosity $3 \times 10^{33} \mathrm{cm}^{-2}\mathrm{s}^{-1}$ [10].

L2 trigger, which is software-based, requires all the available data that associate to RoIs (about 2% of the total event data) from the ROBs. It uses full-granularity information from all detectors and refines the selection of candidate objects. The events rates can be reduced to below 3.5 kHz with the L2 trigger selection in about 10 ms.

Those events selected by the L2 trigger are then transferred to the event-building system and subsequently to the event filter for final selection. The EF trigger has access to the full event data and uses offline reconstruction algorithms and tools. Event selection and classification will be done within a few seconds by EF trigger, giving a further reduction of event to $\sim 200 Hz$. Table 3.6 shows the main trigger objects and their threshold used in 2011 ATLAS data taking, as well as the corresponding event rate after L1 and EF trigger [9].

Events selected by the event filter are moved to permanent storage at the CERN computer center. The system that receives, transfers and stores data between the three levels of trigger is called data acquisition system (DAQ). In addition, it provides the configuration,

control and monitoring of the hardware and software components during the data taking. While another important component of the ATLAS detector is the Detector Control System (DCS), which supervises and controls the ATLAS detector hardware like power-supply voltages, gas and cooling systems, magnetic field, temperatures, and humidity to ensure a safe operation.

3.3 Objects Reconstruction in ATLAS

The stored data after trigger are called RAW data. They contain the information from all sub-detectors in ATLAS. The RAW data are further processed by offline reconstruction algorithms and tools to reconstruct the physics objects such as tracks, electrons, muons, jets and missing transverse energy, which could be used in physics analyses. This reconstruction procedure is done based on a software framework called Athena. In this section, the reconstruction and subsequential identification of electrons, muons, jets and transverse missing energy are described in details.

3.3.1 Electrons

The information from calorimeters and inner detector are used to reconstruct and identify electrons. The performance of electron reconstruction and identification is essential to physic analysis since electrons contribute as final state particles to many SM and new physic processes.

Reconstruction

The reconstruction of central electrons $|\eta| < 2.47$ uses the information from both the EM calorimeter and the inner detector. In general, there are four steps [87] [11],

- First step is searching seed clusters. Sliding-window algorithm is used to search the seed clusters of longitudinal towers with total transverse energy above 2.5 GeV. The window size is 3×5 in units of 0.025×0.025 in $\eta \times \phi$ space.

- Second, the best track which can be associated to the seed cluster is found. The tracks are reconstructed by extrapolating their last measurement point to the middle layer of the calorimeter. They are then associated with the seed cluster if the distance between the track impact point and the cluster position satisfies $\Delta\eta < 0.05$. An electron is reconstructed if at least one track is matched to the seed cluster. In case of more than one track associated with the seed cluster, the track with silicon hits and with smallest $\Delta R = \sqrt{\Delta\eta^2 + \Delta\phi^2}$ is chosen as the best track .

- Third, the cluster energy is determined. The electron cluster is rebuilt using 3×7 (5×5) longitudinal towers of cells in the barrel (end-caps) to take into account the different overall energy in the barrel and end-cap calorimeters. Then the cluster energy is determined [88] by summing four different contributions: (1) the estimated energy deposit in the material in front of the EM calorimeter, (2) the measured energy deposit in the cluster, (3) the estimated external energy deposit outside the cluster, and (4) the estimated energy deposit beyond the EM calorimeter.

- Finally, the four-momentums of central electrons are calculated. The energy is the cluster energy $E_{cluster}$, the η and ϕ are the parameters η_{track} and ϕ_{track} of the best track at the vertex, the transverse momentum p_T is calculated as $p_T = E_{cluster}/cosh(\eta_{track})$.

In the front region, $2.5 < |\eta| < 4.9$, the electron candidates are reconstructed only from energy deposits in the calorimeters. It will not be introduced in detail since only the central electron is used in this analysis.

Identification

The identification of the electron uses selections on the calorimeter, tracking information and some combined variables [11]. There are three kind of selections, the *loose*, *medium* and *tight* selections, to identify electrons with different background rejection powers,

$$\text{rejection} = \frac{1}{\text{electron fake rate}}. \tag{3.4}$$

The *loose* selection uses the shower shape variables of the EM calorimeter as well as the hadronic leakage variables. The *medium* selection includes *loose* selection and adds requirements on the variables from the EM calorimeter strip layer, track quality and track-cluster matching. Based on the *medium* selection, more variables from track-cluster matching, track quality, TRT hits and conversion requirements are added to *tight* selection. The detailed definitions of all variables used in the three level selections are shown in Figure 3.11. The cuts used on these variables are determined and optimized to have an expected jet rejection of 500, 5000 and 50000 for the *loose*, *medium* and *tight* selections respectively.

Type	Description	Name
Loose selection		
Acceptance	$|\eta| < 2.47$	
Hadronic leakage	Ratio of E_T in the first layer of the hadronic calorimeter to E_T of the EM cluster (used over the range $|\eta| < 0.8$ and $|\eta| > 1.37$)	R_{had1}
	Ratio of E_T in the hadronic calorimeter to E_T of the EM cluster (used over the range $|\eta| > 0.8$ and $|\eta| < 1.37$)	R_{had}
Middle layer of EM calorimeter	Ratio of the energy in 3×7 cells over the energy in 7×7 cells centered at the electron cluster position	R_η
	Lateral width of the shower	$w_{\eta2}$
Medium selection (includes loose)		
Strip layer of EM calorimeter	Total shower width	w_{stot}
	Ratio of the energy difference between the largest and second largest energy deposits in the cluster over the sum of these energies	E_{ratio}
Track quality	Number of hits in the pixel detector (≥ 1)	n_{pixel}
	Number of total hits in the pixel and SCT detectors (≥ 7)	n_{Si}
	Transverse impact parameter ($|d_0| < 5$ mm)	d_0
Track – cluster matching	$\Delta\eta$ between the cluster position in the strip layer and the extrapolated track ($|\Delta\eta| < 0.01$)	$\Delta\eta$
Tight selection (includes medium)		
Track – cluster matching	$\Delta\phi$ between the cluster position in the middle layer and the extrapolated track ($|\Delta\phi| < 0.02$)	$\Delta\phi$
	Ratio of the cluster energy to the track momentum	E/p
	Tighter $\Delta\eta$ requirement ($|\Delta\eta| < 0.005$)	$\Delta\eta$
Track quality	Tighter transverse impact parameter requirement ($|d_0| < 1$ mm)	d_0
TRT	Total number of hits in the TRT	n_{TRT}
	Ratio of the number of high-threshold hits to the total number of hits in the TRT	HT_{frac}
Conversions	Number of hits in the b-layer (≥ 1)	n_{BL}
	Veto electron candidates matched to reconstructed photon conversions	

Figure 3.11: Definition of the variables used in the *loose*, *medium* and *tight* electron selection [11].

3.3.2   Muons

In ATLAS detector, a produced muon hits in the Inner Detector (ID), passes through the electromagnetic and hadronic calorimeters, and finally reaches the Muon Spectrometer (MS). Its track is deflected by the magnet system. Muon track reconstruction is performed independently in the ID and MS, while its momentum can be obtained by combining information from the ID, calorimeters and MS.

Reconstruction of Muid Muons

The muon reconstruction chain is called "muid" and contains four different algorithms [89]:

- The Standalone algorithm extrapolates the MS track back to the beam line to determine the direction of flight and the impact parameter of the muon at the interaction point. The muon momentum is measured in MS and corrected by taking into account the energy loss of the muon in the calorimeter.

- The Combined algorithm creates a muon by combining an ID track with a MS track using a global fit of the two tracks.

- The MuGirl algorithm identifies an ID track as a muon if the track extrapolated to the MS can be associated with track segments in the muon chambers. The muon momentum and position are taken from the ID track parameters.

- The MuTagIMO algorithm extrapolates ID tracks to the MS and searches for segments defined by another muon reconstruction algorithm, the Moore algorithm [90]. The MuTagIMO algorithm performs tagging in all three layers (Inner-Middle-Outer) of muon chambers.

Then the results of the four algorithms are merged to reconstruct muid muons, following procedures below:

- All Combined muons are added.

- MuGirl muons that have a combined track are added if they do not share the ID track with one of the Combined muons.

- MuTagIMO muons are added if they do not share the ID track with one of the Combined muons and there is no hit overlap between the segments of the MuTagIMO muon and the MS hits of a combined or a Standalone muon.

- MuGirl muons without a combined track are added if they satisfy the same criteria as used for MuTagIMO muons.

- Standalone muons are added if they are not already part of a Combined muon and if there is no MS hit overlap with the added MuGirl or MuTagIMO muons.

Identification

Some selections are applied on the reconstructed muons to identify muons with different qualities. There are three levels of selections, corresponding *tight*, *medium* and *loose* muons.

- *loose* muons: *Medium* muons and all MuTagIMO muons in muid muons.

- *medium* muons: *Tight* muons plus all Standalone muons in muid muons.

- *tight* muons: all Combined and MuGirl muons in muid muons that have a successful combined fit.

3.3.3 Jets

Due to the QCD confinement (See Section 2.2.2), the colour-charged quarks and gluons produced by the collision at the LHC will fragment into a spray of hadrons before they can be directly detected, becoming jets. The kinematic properties of the jet reflect pretty well the initial properties of the quarks or gluons. In ATLAS detector, a jet creates electromagnetic and hadronic showers in the calorimeter. These showers are measured in calorimeter clusters, which are groups of calorimeter cells. These calorimeter clusters are used by the jet finding algorithms to reconstruct the jet objects. The jets used in this thesis are reconstructed

by the anti-k_T algorithm [91] with a distance parameter 0.4, using topological calorimeter clusters (topo-clusters) as input for the jet finding. In ATLAS nomenclature such jets are termed AntiKt4TopoJets. Below the formation of the topological calorimeter clusters and the jet reconstruction using the anti-k_T algorithm are introduced.

Topological calorimeter clusters

Topological clusters are groups of calorimeter cells that are designed to follow the shower development [92]. The topocluster formation algorithm starts from a seed cell, whose signal/noise ratio (S/N) is above a threshold $S/N > 4$. The noise is estimated as the absolute value of the energy deposited in the calorimeter cell divided by the Root Mean Square (RMS) of the energy distribution measured in events triggered at random bunch crossings. Cells neighboring the seed cell are included iteratively if they have a signal-to-noise ratio $S/N \geq 2$. A topological calorimeter cluster is formed by including all calorimeter cells satisfying the requirement.

A topo-cluster is defined to have zero mass. Its energy equals to the energy sum of all the included calorimeter cells. Its direction is calculated from the weighted averages of the η and ϕ of the constituent cell.

The anti-k_T algorithm

The topological calorimeter clusters defined above are used as "objects" in the anti-k_T jet finding algorithm, which recombines the objects sequentially to be jets [91]. The anti-k_T algorithm uses d_i defined by the squared transverse momentum of a i object $d_i = \frac{1}{p_{T,i}^2}$, and d_{ij} defined by the relative squared transverse momentum of a pair of objects i, j,

$$d_{ij} = min(\frac{1}{p_{T,i}^2}, \frac{1}{p_{T,j}^2})\frac{\Delta R_{ij}^2}{R^2}. \tag{3.5}$$

Here R is the distance parameter which represents a cone size. It can be set to 0.4 or 0.6. ΔR_{ij} which has been introduced in Section 3.2 is the distance between two objects i and j. d_{min} is the minimum value between d_i and d_{ij}. If d_{min} is d_i, the object i is considered as a jet and is removed from the object list. If d_{min} is d_{ij}, object i and j are merged to a new object k. i and j are removed from the object list and k is added in for

sequential identification. The object list will change and the object values will update with the identification procedure going on until there is no object left.

Jet Quality

Some reconstructed jets are not originated from hard scattering events. They could come from the beam-gas events, cosmic rays and large calorimeter noise. Such jets are tagged as "bad" jets using selections on the energy fractions in the electromagnetic and hadronic endcap calorimeters, the pulse signal shape from the calorimeter cell, the jet time comparing to beam collision, as well as the track information. Another category of jets are "ugly" jets, which are the jets recontracted in problematic calorimeter regions that are not well measured. A jet not "bad" neither "ugly" is classified as "good" jets, which will be used in the physics analysis.

3.3.4   B-jet

B-jet identification, also called b-tagging, is important for top-quark studies since one of the top-quark decay products is a b quark. In top-quark analysis, distinguishing the b jets from other jets would help to reduce the background processes which have few b jets. This is done by b-tagging algorithms which explore the unique properties of b quark and its hadronization [93]. The b-hadron from b-quark hadronization remains about 70% of the original b-quark momentum and it has a relatively large mass above 5 GeV. These make the decay products of the b hadron having large transverse momentums and a large opening angle. In addition, the b hadron travels with a relatively long distance before decaying due to its relatively long life time, making the primary vertex of the b-quark hadronization distinct from the secondary vertex of b-hadron decay. As a result, the distances between b-jet tracks and the b-jets primary vertex are larger than the ones between light-jet tracks and a light-jet primary vertex. Such distance is characterized by the impact parameters (IP) of a track, including the transverse impact parameter d_0 and longitudinal impact parameter z_0. d_0 is the distance of closest approach of the track to the primary vertex point in x-y plane while z_0 is the z coordinate of the track at the point of closest approach. Also the

decay length between primary vertex and secondary vertex is larger for a b jet than a light jet. Furthermore, the b-hadron decay topology such as large charged decay multiplicity and leptonic decay products can be used for b-jet identification.

B-tagging Algorithm

Many b-tagging algorithms have been developed in ATLAS, such as the impact parameter-based algorithms JetProb, IP1D, IP3D [94], the secondary vertex-based algorithms SV0, SV1 [93], and the algorithm using topology of b-hadron decay such as JetFitter [95]. In this analysis one combined b-tagging algorithm is used, named JetFitterCombNN tagger [13], which is the combination of JetFitter algorithm and IP3D algorithm based on artificial neural network techniques.

The JetFitter algorithm exploits the topology of weak b- and c-hadrons decays inside the jet, such as number of vertices, number of the tracks associated to the vertex, invariant mass of decayed charged particle tracks, energies information of decayed charged particle and flight length significance. A likelihood function containing probability density functions of condensed term for different jets flavours is build as the discrimination between b, c and light jets.

$$\mathcal{L}^{b,c,l} = \sum (coeff) PDF(mass) PDF(energy) PDF(significance) \qquad (3.6)$$

where coeff represents how probable it is to find a certain topology for a given flavour. The details about this algorithm can be found in reference [95].

The IP3D algorithms uses transverse and longitudinal impact parameter significance, $S_{d_0} = d_0/\sigma_{d_0}$, $S_{z_0} = z_0/\sigma_{z_0}$, where σ is their resolution. The measured S_i $(i = d_0, z_0)$ is compared to pre-defined smoothed and normalized distributions for both the b-jet and light jet hypotheses, $b(S_i)$ and $l(S_i)$, obtained initially from Monte Carlo. Two sets of two-dimensional probability density functions are constructed for each track, the probability from a b-jet $P_b(S_{d_0}, S_{z_0})$ and the probability from a light jet $P_l(S_{d_0}, S_{z_0})$. The weight of a i track in a jet is defined by the ratio,

$$w_i = P_b(S_{d_0}, S_{z_0})/P_l(S_{d_0}, S_{z_0}). \qquad (3.7)$$

The weight of the jet is used as the discriminant variable for b-jet identification,

$$w_{\text{jet}} = \sum_{N_{\text{track}}} \ln w_i. \tag{3.8}$$

A b-jet is identified by applying the selection on the weight of the jets. An example of the JetFitterCombNN weight distribution for different flavour jets is show in Figure 3.12 (a).

(a)   (b)
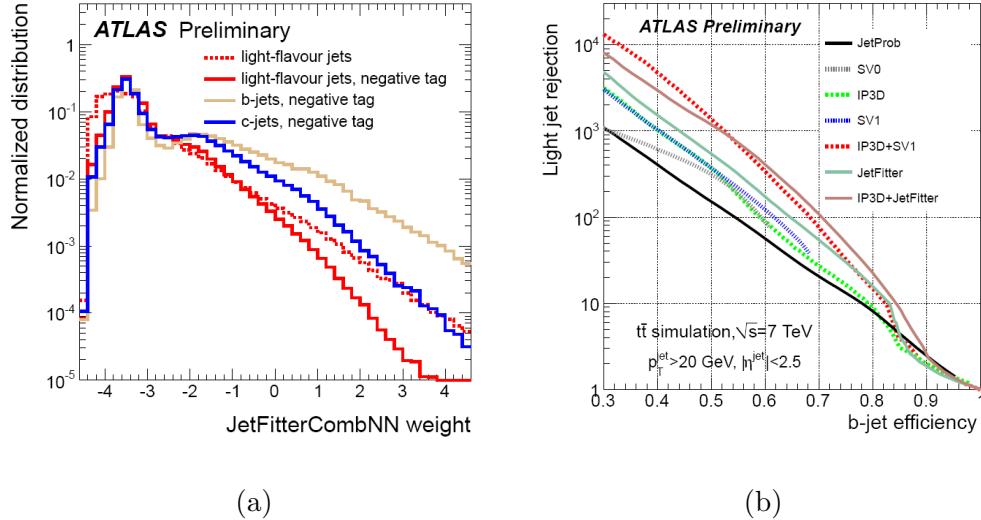
Figure 3.12: (a) The normalized JetFitterCombNN weight distribution for different jet flavour [12]. (b) Light-jet rejection as a function of the b-jet tagging efficiency, based on $t\bar{t}$ simulated events [13]

.

B-tagging Efficiency and Light Jet Rejection

The performance of the b-tagging algorithm is characterized by the b-tagging efficiency and the light jet rejection power. The b-tagging efficiency is defined by,

$$\epsilon_{\text{b-tagging}} = \frac{N_{\text{b tagged}}}{N_{b\,total}}, \tag{3.9}$$

where $N_{\mathrm{b\,tagged}}$ is the number of b jets identified by the b-tagging algorithm, and $N_{b\,total}$ denotes the total number of b jets. The light jet rejection power is given by,

$$\text{rejection} = \frac{1}{\epsilon_{\text{l-tagging}}}, \qquad \text{with } \epsilon_{\text{l-tagging}} = \frac{N_{\mathrm{l\,tagged}}}{N_{l\,total}}. \tag{3.10}$$

Here $N_{\mathrm{l\,tagged}}$ is the number of light jets passed by the b-tagging selection, and $N_{l\,total}$ is the total number of light jets. Figure 3.12 (b) shows a comparison of the performance of different tagging algorithms, obtained from Monte Carlo simulated $t\bar{t}$ samples.

The b-tagging efficiency and light jet rejection can be estimated from data using data-driven methods. Two most popular methods used to measure b-tagging efficiency are the p_T^{rel} method and the System8 method [13], while for light jet rejection measurement the negative weight method and the sv0mass method are used [12]. More information about these measurements can be found in the references [13, 12].

3.3.5 Missing Transverse Energy

The missing transverse energy (E_T^{miss}) is a measure of the momentum of the escaping neutrinos. It also includes corrections for energy losses due to detector inefficiencies and resolution that lead to the mis-measurement of the true E_T of the final interacting objects. In this analysis, the E_T^{miss} is reconstructed by the Cell-based algorithm, including contributions from transverse energy deposits in the calorimeters, corrections for energy loss in the cryostat and measured muons [96]:

$$E_{x(y)}^{miss} = E_{x(y)}^{miss,calo} + E_{x(y)}^{miss,cryo} + E_{x(y)}^{miss,muon}. \tag{3.11}$$

The x and y components of the calorimeter $E_{x(y)}^{miss,calo}$ term are calculated from the transverse energies measured in the calorimeter cells (TopoCells) that belong to the reconstructed topo-cluster,

$$E_{x(y)}^{miss,calo} = -\sum_{TopoCells} E_{x(y)}. \tag{3.12}$$

The $E_{x(y)}^{miss,muon}$ muon term is calculated from the momenta of muons that are reconstructed in the muon spectrometer with a matched track in the inner detector,

$$E_{x(y)}^{miss,muon} = -\sum_{Muons} E_{x(y)}. \tag{3.13}$$

The $E_{x(y)}^{miss,cryo}$ reconstruction recovers this loss of energy in the cryostat using the correlation of energies between the last layer of the liquid argon calorimeter and the first layer of the hadronic calorimeter, as well as the correction for the end-cap cryostats.

The $E_{\mathrm{T}}^{\mathrm{miss}}$ is then obtained,

$$E_{\mathrm{T}}^{\mathrm{miss}} = \sqrt{(E_x^{miss})^2 + (E_y^{miss})^2} \tag{3.14}$$

$E_{\mathrm{T}}^{\mathrm{miss}}$ is further refined by applying object level corrections for the contributions which arise from identified electrons, muons and jets.

3.4   Luminosity Measurement

An accurate measurement of the delivered luminosity is a key component of the ATLAS physics program [14]. The luminosity is essential to evaluate the background levels in the cross section measurements of Standard Model processes and in the searching of new physics. The uncertainties of the luminosity measurement constitute as one source of the systematics in these measurements and determines the sensitivity to new physics signatures. In ATLAS, the luminosity is measured independently using several detectors and multiple algorithms, each having different acceptance, response to pile-up (multiple pp interactions within the same bunch crossing), and sensitivity to backgrounds. The measured luminosity are then calibrated by beam separation scans, also called van der Meer (vdM) scans. This section briefly introduces the luminosity measurement and calibration in ATLAS, while more details about the procedure can be found in reference [14] [97].

The luminosity of a proton-proton collier can be given by,

$$L = \frac{\mu n_b f}{\sigma_{inel}} \tag{3.15}$$

where μ is the average number of inelastic interactions per bunch crossing (BC), n_b is the number of bunch pairs colliding at the interaction point (IP), f is the LHC revolution frequency, and σ_{inel} is the total inelastic proton-proton collision cross section.

ATLAS monitors the delivered luminosity by measuring a visible number of interactions per BC, denoted by μ_{vis}, using a variety of detectors and different algorithms. The luminosity can then be expressed as

$$L = \frac{\mu_{vis} n_b f}{\sigma_{vis}}, \tag{3.16}$$

where $\sigma_{vis} = \epsilon \sigma_{inel}$ is the visible cross section, obtained by the predicted total inelastic cross section σ_{inel} times the efficiency ϵ of a particular detector and algorithm from Monte Carlo simulation. The measured luminosity is calibrated by vdM-scan technique, which determines σ_{vis} without a priori knowledge of the inelastic pp cross section or of detector efficiencies.

3.4.1 Measurement of μ_{vis}

There are two primary detectors used to measure μ_{vis} bunch-by-bunch: LUCID (LUminosity measurement using a Cerenkov Integrating Detector) [98] and BCM (Beam Condition Monitoring) [99]. LUCID consists of two gas Cerenkov detectors that surround the beampipe on each side of the IP. The BCM detector has four diamond detectors arranged around the beampipe on each side of the IP, which are split into two horizontal and two vertical detectors called BCMH and BCMV. Both LUCID and BCM record signals of interactions for each BC with a preset threshold. EventOR and EventAND algorithms use these signals to determine the μ_{vis}.

During a given time, the total number of BCs is N_{BC}. The BCs with at least one signal are counted to N_{OR}. The μ_{vis} is given by the EventOR algorithm,

$$\mu_{vis}^{OR} = -ln(1 - \frac{N_{OR}}{N_{BC}}) \tag{3.17}$$

In the case of EventAND algorithm, a BC is counted in N_{AND} if there is at least one signal on both sides of the IP. μ_{vis} is determined by

$$\frac{N_{AND}}{N_{BC}} = 1 - 2e^{-(1+\sigma_{visOR}/\sigma_{visAND})\mu_{vis}^{AND}/2} + e^{-(\sigma_{visOR}/\sigma_{visAND})\mu_{vis}^{AND}} \tag{3.18}$$

where σ_{visOR} and σ_{visAND} are corresponding visible cross sections.

The BCMH and BCMV are read out separately, leading to different luminosity measurements. In addition, the Forward Calorimeter (FCal) and the Hadronic Tile Calorimeter (Tile) of ATLAS detector are also used to measure the luminosity by monitoring the currents drawn in the different parts of the detector due to inelastic collisions. A comparison of the average number of interactions per bunch crossing $< \mu >$ measured by different detectors and algorithms is shown in Figure 3.13. More information about additional detectors and algorithms used for the luminosity measurement can be found in reference [97].

3.4.2 Calibration of σ_{vis}

The calibration of σ_{vis} is performed using dedicated vdM scans where the LHC machine parameters can be directly measured. Comparing to normal physics operations, the beam
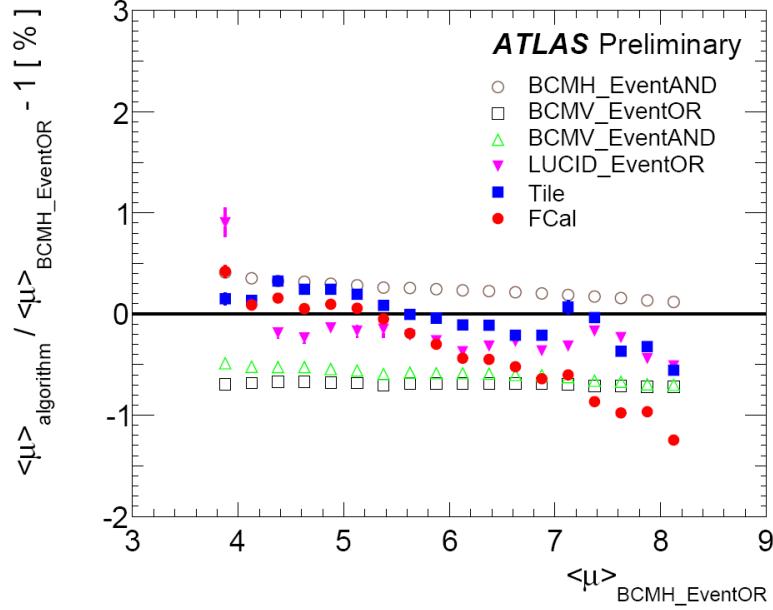
Figure 3.13: Fractional deviation in $< \mu >$ measured by different detectors and algorithms with respect to the one measured by EventOR algorithm using BCMH detector. Statistical uncertainties per point are negligible [14].

conditions during the dedicated vdM scans are with fewer bunches colliding, no bunch trains, and lower bunch intensities. Table 3.7 shows a summary of the main characteristics of the May 2011 vdM scans (numbered VII and VIII) used for the luminosity calibration.

As introduced in Section 3.1, the luminosity inferred from measured accelerator parameters is given by

$$L = f_r \frac{n_b n_1 n_2}{2\pi \Sigma_x \Sigma_y}. \tag{3.19}$$

where n_1 and n_2 are the numbers of protons per bunch in beam 1 and beam 2 respectively, together forming the bunch charge product. Σ_x and Σ_y characterize the horizontal and vertical profiles of the colliding beams. Comparing Equation 3.16 and Equation 3.19, the σ_{vis} can be determined from the peak luminosity with the peak interaction rate μ_{vis}^{MAX} observed by a given detector and algorithm during the vdM scan,

$$\sigma_{vis} = \mu_{vis}^{MAX} \frac{2\pi \Sigma_x \Sigma_y}{n_1 n_2}. \tag{3.20}$$

In a vdM scan, the beams are separated by steps of a known distance which allows a direct

	$vdMScan$ VII-VIII
	15 May, 2011
Scan Directions	2 sets of horizontal plus vertical scans
Total Scan Steps per Plane	25
Scan Duration per Step	20s
Number of bunches colliding in ATLAS	14
Total number of bunches per beam	38
Number of protons per bunch	$\sim 0.8 \times 10^{11}$
β^*	~ 1.5m
Normalized Transverse Emittance	$\sim 40\mu$m
Typical luminosity/bunch	0.38μb^{-1}/s
μ (interactions/crossing)	2.3

Table 3.7: Summary of the main characteristics of the 2011 vdM scans performed at the ATLAS interaction point [14]. The values of luminosity/bunch and μ are given for zero beam separation.

measurement of Σ_x and Σ_y. The bunch charge product n_1 and n_2 can be measured by eight Bunch Current Transformers (BCTs) in multi-step process. Since the beam sizes and the bunch charge product can vary bunch-to-bunch, their measurements must be performed independently for each BC.

3.4.3   Total Luminosity Uncertainty

The total uncertainty in the measurement of the luminosity by ATLAS in 2011 consists of four main components, the uncertainty of μ determination, the σ_{vis} calibration uncertainty from vdM scans, the long-term stability of the detector and the corrections due to background effects. As a summary, a total relative uncertainty of 3.7% is found. Table 3.8 lists the contributions of different sources to the total systematic uncertainty on luminosity measurement.

Uncertainty Source	$\delta\mathcal{L}/\mathcal{L}$
μ Dependence	1.0%
vdM Scan Calibration	3.4%
Long-term consistency	1.0%
Background Correction	0.2%
Total	3.7%

Table 3.8: Relative uncertainty on the luminosity measurement in 2011, broken down by source [14].

3.5 ATLAS Data Distribution and Data Quality

The ATLAS distributed computing system consists of three classes, named as Tier-0, Tier-1 and Tier-2 [100]. The recorded raw data acquired with the ATLAS detector are stored into tape immediately at the Tier-0. In addition, the replica of data files are sent to 10 Tier-1 centers to be stored on tape, ensuring a long-term protection against a possible data loss. The objects reconstruction is carried out at the Tier-0, producing Event Summary Data (ESD) for the detector and reconstruction studies. ESD and the derived smaller Analysis Object Data (AOD) files are distributed to Tier-1 and Tier-2 centers for further analysis.

During 2011, ATLAS has recorded $5.6fb^{-1}$ data of pp collisions, with a peak luminosity of $3.6 \times 10^{33} \text{cm}^{-2}\text{s}^{-1}$. With the availability of collision data, it is essential for everyone to understand what datasets are good for physics analysis. The data quality (DQ) is determined by assessing the LHC status, the operational conditions of hardware and software elements of the detector, the trigger quality, the monitoring of the data acquisition systems, and some complex analysis of physics quantities on data reconstruction. Data quality decisions are made and recorded using green, yellow, and red flags corresponding to good, caution and bad data quality, supplemented by grey (unknown - usually due to insufficient statistics) and black (subsystem off) [101]. Final data quality flags are derived after full reconstruction, with experts converging on the "green" and "red" states. Figure 3.14 shows the fractions of good data from each components of the ATLAS [15]. In 2011 ATLAS data-taking, approximately 90% of the $5.6fb^{-1}$ of delivered luminosity is available for physics analysis.

ATLAS data-taking is divided into runs and luminosity blocks (LB). The luminosity blocks are discrete periods of time ($\sim$ 2 minutes) over which detector conditions are assumed to be constant. The runs and luminosity blocks with "green" data quality finally form the GoodRunList (GRL) to be used by each analysis group to select the good data from all recorded data.

Inner Tracking Detectors			Calorimeters				Muon Detectors				Magnets	
Pixel	SCT	TRT	LAr EM	LAr HAD	LAr FWD	Tile	MDT	RPC	CSC	TGC	Solenoid	Toroid
99.8	99.6	99.2	97.5	99.2	99.5	99.2	99.4	98.8	99.4	99.1	99.8	99.3

Figure 3.14: Luminosity weighted relative detector uptime and good quality data delivery during 2011 stable beams in pp collisions at $\sqrt{s} = 7$ TeV between March 13th and October 30th (in %), after the summer 2011 reprocessing campaign [15].

66

Chapter 4

PHENOMENOLOGY, SIMULATION AND DATA

With large amount of data collected by the ATLAS detector, the precise cross section measurements of single top-quark production processes are expected. For this purpose, a good understanding of the phenomenology of signal and background processes is necessary. The first part of this chapter discusses the kinematical properties of the signal and of other processes that could produce a similar signature. The second part describes the Monte-Carlo generations used to determine the event selection acceptance and to model the kinematics of signal and background events. In addition, the information concerning the data used in this analysis are introduced in the final part of this chapter.

4.1 Phenomenology

The knowledge of the properties of single top-quark events and of all contributing background is essential to define events selection criteria to enhance the signal purity and reduce the level of backgrounds. This section describes the final states of the t-channel single top-quark events and of the possible background processes.

4.1.1 Single top-quark Production

An illustration of single top quark t-channel production is shown in Figure 4.1. In W-gluon fusion process ($qg \rightarrow q't\bar{b}$), the produced top quark decays to a W boson, which can then decay leptonically to an electron, a muon or a tau, and the associated neutrino. In this channel the signal signature for a single top-quark consists of a charged lepton and a neutrino from the W decay, a b-quark from the top-quark decay, a light quark produced in the forward direction and a second b-quark coming from initial state gluon splitting. At the detector level this decay products result in a signature consisting of a lepton, at least two jets in which one is a b-jet and large transverse missing energy ($E_\mathrm{T}^\mathrm{miss}$) due to the undetected neutrino in the detector. The light quark in this channel often recoils softly against the quark top and ends up in the forward region of the detector. It is an important feature of t-channel single top-quark process to distinguish it from background processes. On the other hand, the b-jet from gluon splitting is produced collinearly to the beam direction and in general escapes detector identification.

The W boson in single top-quark production could also decay hadronically to quark-antiquark pair. This kind of process is difficult to be distinguished from QCD-multijet events. For this reason the leptonic decay which leads to lepton+jets final state and provides the cleanest event signature is used to perform cross section measurement in this analysis. According to the W boson decaying to a electron or a muon, the leptonic process can be further divided into electron channel and muon channel. The $W \rightarrow \tau\nu$ decay with a subsequent decay of the τ lepton to $e\nu_e\nu_\tau$ and $\mu\nu_\mu\nu_\tau$ are also accounted in the electron channel and muon channel respectively.

The single top-quark s-channel process consists of two b jets in the final states. The

Wt-channel single top-quark production has one associated W bosons and one W boson from top quark decay, resulting two leptons in the final states. These two processes are not expected to constitute large backgrounds due to their different final state signatures and lower production cross sections.

The cross sections of single top-quark production at NLO with NNLL corrections are listed in Table 4.1.
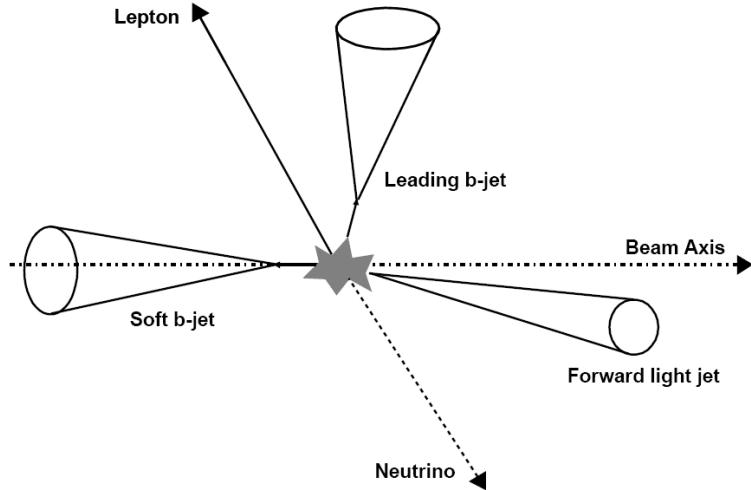
Figure 4.1: Signature of single top-quark t-channel production [16].

t-channel	64.57 + 2.71 - 2.01 pb
s-channel	4.63 + 0.19 - 0.17 pb
Wt	15.74 + 1.06 - 1.08 pb

Table 4.1: cross-sections of single top-quark production for $m_t = 172.5\,\mathrm{GeV}/c^2$ at NLO with NNLL corrections [52, 53, 20].
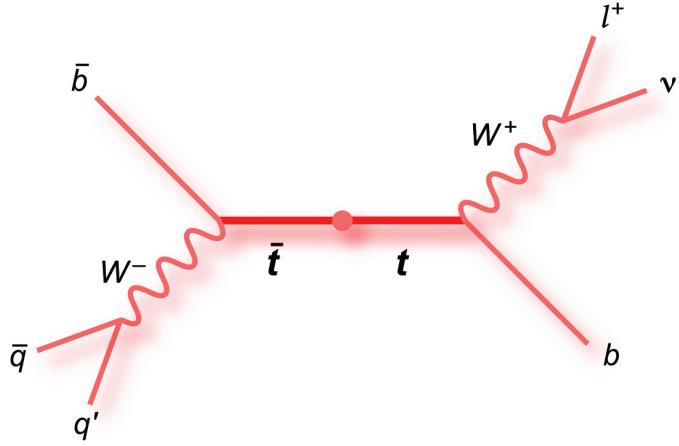
Figure 4.2: An illustration of top-quark pair semi-leptonic decay [17].

4.1.2   Top-quark Pair Background

Top-quark pair production constitutes an important background to single top-quark events. As shown in Figure 4.2, the two top quarks produced decay into two W bosons and two b quarks. The two W bosons can then decay leptonically or hadronically. Two modes of top-quark pair production contribute as the backgrounds to single top events, the semi-leptonic mode where one W boson decays into a lepton-neutrino pair and the other W boson decays into a quark-antiquark pair, and the dileptonic mode where both W bosons decay into lepton-neutrino pairs. The semi-leptonic mode of $t\bar{t}$ events have one lepton, four jets (two b-jets) and large missing energy. It contributes to the background of single top events if only two of the four jets are identified. Dileptonic $t\bar{t}$ events have two high p_T leptons, two b-jets and missing energy due to the neutrinos. It may mimic the t-channel single top-quark production final-state signature if one of the leptons is not identified.

At the LHC the total top-quark pair production cross-section is $\sigma(t\bar{t}) = 164.6\,\mathrm{pb}$ [42], about two times larger than the total single top-quark cross-section. The branching ratio of semi-leptonic mode is about 30% while the dileptonic mode has low branching ratio of 5%.
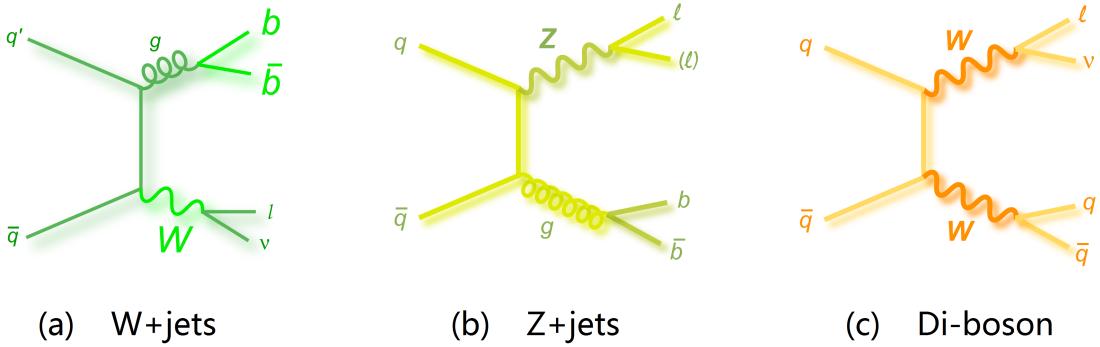
Figure 4.3: Feynman diagram of top-quark pair semi-leptonic decay [17].

4.1.3 W+jets, Z+jets, Diboson Backgrounds

Beside top-quark decay, W bosons can also be produced in many different ways in proton-proton collisions at the LHC. The Feynman diagram of an example W production from quark-antiquark annihilation is shown in Figure 4.3 (a). The W boson is produced in association with quarks, which could have same final states of single top-quark production. The associated quark can be light quark (u,d,s), b quark or c quark. This kind of production lead to W+jets events in data, which constitute a main source of background due to its cross-section several orders of magnitude above that of single top-quark production.

Figure 4.3 (b) shows an example of Z+jets production. If one of the two leptons from Z boson decay is not identified this process has a similar signature as single top-quark production, which makes Z+jets events another source of background. The Z+jets background is expected to be sizably smaller than W+jets background.

WW, WZ, and ZZ diboson events where at least one of the bosons decays leptonically constitute a small background to the single top-quark signal events. These events are also collectively called diboson backgrounds. An example of such background is shown in Figure 4.3 (c).

4.1.4   QCD Multijet Background

The QCD process has a huge cross section in LHC and manifests itself in multiple jets final states. These multijet events contribute to a background of single top-quark events if one jet is misidentified as an isolated lepton or a real non prompt leptons (coming from b/c-quark semileptonic decay for example) that appears isolated. Thus one key point to reduce QCD multijet background rests on the low lepton misidentification efficiency and good isolation between leptons and jets. In single top-quark study, some specific isolation criteria (see Section 5.1) are explored to make sure the strong rejection power of the QCD multijet background. In addition, the lack of W boson and its decay products neutrino in multijets events could be used to distinguish it from single top-quark production.

4.2 Monte Carlo Simulation

The event features of single top-quark t-channel production and its backgrounds can be simulated by Monte Carlo (MC) method. MC simulations of signal and background events are used to estimate the signal efficiency and background rates in data after certain selections. They are also used to model the distributions of kinematic variables in the events. The Monte Carlo simulation of a physics process starts from the generation of the physic process according to a theoretical model, then proceeds with full detector simulation where the interactions between physic process particles and the detector materials are simulated by a software toolkit called Geant4 [102]. After detector simulation, the MC raw data are produced, which are finally subjected to the same reconstruction and reprocessing as real raw data as introduced in Section 3.3 and Section 3.5.

Event generator are used for the generation of a physic process, producing events with the kinematics predicted by the theory. The parton distribution functions (PDFs) used in the event generator, describing the probability density for finding a parton inside the hadron, are derived from experimental data [103]. The leading order (LO) calculation of the cross section is based on hard process, while the radiation of extra particles and the hadronization effects require higher-order corrections. For this reason, the Leading Order (LO) matrix element generator such as AcerMC [104] and ALPGEN [105] and Next-to-Leading-Order (NLO) generator such as MC@NLO [106] and Powheg [107, 108] are normally interfaced with showering and hadronization generator such as Herwig [109] and Pythia [110] for event generation. The Jimmy generator [111] is also used with Herwig to model multiple interactions.

This section introduces the generators used for the Monte Carlo simulations of the single top-quark production and its backgrounds, as well as the corresponding cross sections. K-factors are used to correct the generator cross section to the theoretical calculation (NLO or NNLL or approximate NNLO, depending of the available calculation).

The QCD multijet process is difficult to model with MC due to its large theoretical cross section uncertainties. This process is modeled using side-band regions in the data, which will be introduced in following section.

4.2.1   Single Top-quark MC samples

The single top-quark production samples have been generated using the ACERMC generator coupled to PYTHIA for hadronization. The ISR/FSR samples are generated by varying the parameters controlling the initial state radiation (ISR) and final state radiation (FSR) by a factor of two up and down, to estimate the uncertainties in ISR/FSR modeling. The cross sections of subprocesses and k-factors of single top-quark production are summarized in Table 4.2.

	σ [pb]	k-factor	Generator
t-channel (e+jets)	6.94	1.0	ACERMC+Pythia
t-channel (μ+jets)	6.83	1.0	ACERMC+Pythia
t-channel (τ+jets)	7.26	1.0	ACERMC+Pythia
s-channel (e+jets)	0.498	1.0	ACERMC+Pythia
s-channel (μ+jets)	0.489	1.0	ACERMC+Pythia
s-channel (τ+jets)	0.521	1.0	ACERMC+Pythia
$W + t$-channel all decays	15.74	1.0	ACERMC+Pythia
t-channel (e) ISR/FSR up/down	6.94	1.0	ACERMC+Pythia
t-channel (μ) ISR/FSR up/down	6.83	1.0	ACERMC+Pythia
t-channel (τ) ISR/FSR up/down	7.26	1.0	ACERMC+Pythia
s-channel (e) ISR/FSR up/down	0.498	1.0	ACERMC+Pythia
s-channel (μ) ISR/FSR up/down	0.489	1.0	ACERMC+Pythia
s-channel (τ) ISR/FSR up/down	0.521	1.0	ACERMC+Pythia
$W + t$-channel ISR/FSR up/down	15.74	1.0	ACERMC+Pythia

Table 4.2: Single top-quark event Monte Carlo samples used for the analyses.The single-top processes already include the correction to approximate NNLO in the cross-section column.

4.2.2 Top-quark pair MC samples

Top-quark pair events have been generated using MC@NLO 3.41 coupled to HERWIG with JIMMY for hadronization, with the NLO parton density function CTEQ6.6, and a scale choice of $\mu_R = \mu_F = m_t$. For systematic studies, the POWHEG generator was used, and interfaced to both HERWIG and PYTHIA for hadronization modeling studies. Initial and Final State Radiation (ISR/FSR) effects on the acceptance have been studied with the ACERMC generator interfaced with PYTHIA for the hadronization. The associated cross-sections of the MC samples of top-quark pair production are summarized in Table 4.3.

	σ [pb]	k-factor	Generator
$t\bar{t}$ no fully hadronic	80.1	1.12	MC@NLO+Herwig
$t\bar{t}$ no fully hadronic	79.117	1.13	POWHEG+Herwig
$t\bar{t}$ no fully hadronic	79.117	1.13	POWHEG+Pythia
$t\bar{t}$ no fully hadronic ISR/FSR up/down	58.23	1.53	ACERMC+Pythia

Table 4.3: Top-quark event Monte Carlo samples used for the analysis. The single top-quark processes already include the correction to approximate NNLO in the cross-section column.

4.2.3 W+jets, Z+jets and Diboson MC samples

The ALPGEN generator along with the HERWIG parton shower algorithm was used for the generation of inclusive W+jets events. According to the jet flavour, W+jets event can be separated in W+light jet process, $Wb\bar{b}$ process, $Wc\bar{c}$ process and Wc process. Each of these process consists of several sub-processes with different numbers of partons in the final states. The cross sections differ quite a bit between all these different processes as shown in Table 4.4. These process are generated separately to have large enough statistics, allowing proper studies on the processes with high parton multiplicities and with different jet flavours.

However, there is a double counting problem because the phase space can be populated both by W+N partons events and W+(N-1) partons events with hard radiation from the parton shower. The MLM matching scheme [112] is used to remove this double-counting by vetoing some events from each sample.

Another problem is that the W+light jet sample may have contributions from Wbb, Wcc or Wc processes. Similar flavour overlap situation may also exist in Wbb, Wcc and Wc samples. A flavour overlap method is developed to deal with this problem. For every event in all those processes, a variable "HFOR", containing the information of quark flavour and heavy flavour multiplicity, is decided by matching the jets in the event with quarks in truth level after parton showering using $\Delta R = \sqrt{(\Delta\eta)^2 + (\Delta\phi)^2}$. It is used to identify the flavour of the event to be a W+light jet event or a Wbb event or a Wcc event or a Wc event. All W+jets samples are combined and re-classified to W+light samples, Wbb samples, Wcc samples and Wc samples by the variable "HFOR". In such way there is no flavour overlap between these samples.

Z+jets samples were simulated using the leading order ALPGEN generator, combined with HERWIG for the parton showering. Corresponding cross-sections are reported in Table 4.5.

WW, WZ, and ZZ diboson processes were simulated using HERWIG. Table 4.5 summarizes the relevant information for the MC samples of the $W+$ jets, $Z+$ jets, and diboson backgrounds used in this analysis.

4.3 Data

This analysis uses the data collected by the ATLAS detector between March and June in 2011 at the LHC with proton-proton collision at a center-of-mass energy of $\sqrt{s} = 7$ TeV. The data are recorded base on single lepton triggers (see Section 3.2.5). The good runs list as introduced in Section 3.5 is used to select the data with good quality. The final data size after these selections are integrated luminosity of 1.04 ± 0.04 pb^{-1}. The uncertainties on the luminosity calculation is about 3.7%, which contributes one source of the systematics in the cross section measurement in this thesis.

	Cross-section [pb]	k-factor	Generator
$W \to \ell\nu + 0$ parton	6,920	1.2	+Herwig
$W \to \ell\nu + 1$ partons	1,300	1.2	ALPGEN+Herwig
$W \to \ell\nu + 2$ partons	380	1.2	ALPGEN+Herwig
$W \to \ell\nu + 3$ partons	100	1.2	ALPGEN+Herwig
$W \to \ell\nu + 4$ partons	26	1.2	ALPGEN+Herwig
$W \to \ell\nu + 5$ partons	7	1.2	ALPGEN+Herwig
$W \to \ell\nu + b\bar{b} + 0$ parton	47	1.2	ALPGEN+Herwig
$W \to \ell\nu + b\bar{b} + 1$ partons	36	1.2	ALPGEN+Herwig
$W \to \ell\nu + b\bar{b} + 2$ partons	17	1.2	ALPGEN+Herwig
$W \to \ell\nu + b\bar{b} + 3$ partons	7	1.2	ALPGEN+Herwig
$W \to \ell\nu + c\bar{c} + 0$ parton	128	1.2	ALPGEN+Herwig
$W \to \ell\nu + c\bar{c} + 1$ partons	105	1.2	ALPGEN+Herwig
$W \to \ell\nu + c\bar{c} + 2$ partons	52	1.2	ALPGEN+Herwig
$W \to \ell\nu + c\bar{c} + 3$ partons	17	1.2	ALPGEN+Herwig
$W \to \ell\nu + c + 0$ parton	644	1.52	ALPGEN+Herwig
$W \to \ell\nu + c + 1$ partons	205	1.52	ALPGEN+Herwig
$W \to \ell\nu + c + 2$ partons	51	1.52	ALPGEN+Herwig
$W \to \ell\nu + c + 3$ partons	11	1.52	ALPGEN+Herwig
$W \to \ell\nu + c + 4$ partons	3	1.52	ALPGEN+Herwig

Table 4.4: Monte Carlo samples used for the presented analysis. The cross-section column includes any K-factors and branching ratios.

	Cross-section [pb]	k-factor	Generator
$Z \to \ell\ell + 0$ parton	668	1.25	ALPGEN+Herwig
$Z \to \ell\ell + 1$ partons	134	1.25	ALPGEN+Herwig
$Z \to \ell\ell + 2$ partons	41	1.25	ALPGEN+Herwig
$Z \to \ell\ell + 3$ partons	11	1.25	ALPGEN+Herwig
$Z \to \ell\ell + 4$ partons	2.9	1.25	ALPGEN+Herwig
$Z \to \ell\ell + 5$ partons	0.8	1.25	ALPGEN+Herwig
WW	11.5	1.48	Herwig
WZ	3.46	1.60	Herwig
ZZ	0.97	1.30	Herwig

Table 4.5: Monte Carlo samples used for the presented analysis. The cross-section column includes any K-factors and branching ratios.

Chapter 5

EVENT PRE-SELECTION AND BACKGROUND ESTIMATION

Single top-quark t-channel cross section measurement starts with the pre-selection of the data, which refers a set of selections established to select single top-quark t-channel signal events. Same pre-selection is also used on Monte Carlo simulated samples (MC samples) of single top-quark t-, s- and Wt-channels, $t\bar{t}$ process, W+jets process, Z+jets process and diboson process. The data set after pre-selection is a mix of signal t-channel single top-quark events and all backgrounds events. The QCD-multijets background contribution is estimated using a binned likelihood fit to the side-band region of $E_{\mathrm{T}}^{\mathrm{miss}}$distribution in the data, where the template of QCD process is obtained from data and the templates of all the other processes are from their MC samples. The normalization of W+jets backgrounds, including W+light jets process, Wbb process, Wcc process and Wc process, are derived from data and its kinematic distributions are taken from the Monte Carlo simulated samples. The contributions of $t\bar{t}$ background, diboson background, single top-quark s-channel and Wt-channel process are estimated using their MC samples.

The pre-selection, established based on the knowledge of the phenomenology of t-channel single top-quark production and its background processes, is described first in this chapter. Then the estimation of QCD-multijets background and W+jets background are introduced in detail. Finally the event yields of data and all Monte Carlo simulated samples after pre-selection are listed.

5.1 Object Selection

Based on the reconstructed objects as introduced in Section 3.3, additional selections are applied according to the features of the objects in single top-quark t-channel production, which are central lepton with high p_{T}, high p_{T} jets and the central b jet. High quality leptons are required with additional isolation criteria to reduce mainly the QCD-multijet background.

Electrons are selected with "Tight" quality and a $p_{\mathrm{T}} > 25$ GeV and $|\eta_{\mathrm{clus}}| < 2.47$ (η_{clus} denotes the electromagnetic cluster position). A veto is applied to electron candidates in the region $1.37 < |\eta_{\mathrm{clus}}| < 1.52$ corresponding to the calorimeter barrel-endcap overlap region with limited instrumentation. To reduce the backgrounds due to hadrons faking an electron signature, electrons from heavy-flavour decays or photon conversions, the isolation criteria of electrons are explored, which requires low calorimeter activity and few tracks within an η-ϕ cone surrounding the electron. Calorimeter activity is gauged using Etcone30, the total energy in an $\eta - \phi$ cone of 0.3 centered around the electron after the subtraction of the energy associated with the electron itself. Track isolation is determined using Ptcone30, which gives the scalar sum of p_{T} for all tracks within a cone of 0.3 around the electron, not including the p_{T} of the electron itself. The calorimeter isolation requirement selects electrons with Etcone30$/p_{\mathrm{T}} < 0.15$, while the track isolation demands Ptcone30$/p_{\mathrm{T}} < 0.10$.

Muons are required with "Tight" quality, $p_{\mathrm{T}} > 25$ GeV and the pseudo-rapidity region of $|\eta| < 2.5$. Muons must also satisfy a set of requirements on track quality in the inner detector [113]. The isolation criteria are applied in order to reduce background contamination from leptonic decays of heavy flavour quarks resulting in a muon inside a jet. The transverse energy within a cone of $R = 0.3$ about the muon direction, named Etcone30, is required Etcone30$/p_{\mathrm{T}} < 0.15$. While the scalar sum of transverse momenta of additional tracks inside a $R = 0.3$ cone around the muon, named Ptcone30, must satisfy Ptcone30$/p_{\mathrm{T}} < 0.10$. In addition, an overlap removal between jets and muons is applied, removing any muon whose momentum direction is within a $\Delta R < 0.4$ cone of a jet with $p_{\mathrm{T}} > 20$ GeV.

Jets are selected with $p_{T} > 25$ GeV and $|\eta| < 4.5$. Jets overlapping with identified electron candidates within a cone of $\Delta R < 0.2$ are removed from the list of jets, as the jet

and the electron are very likely to correspond the same physics object.

The b-tagging requires a JetFitterCombNN tagger weight above 2.40 which corresponds to a b-tagging efficiency of 56% and a light quark jet rejection factor of 520 (the rejection is defined in Section 3.3.4). The b-tagged jet is also required to have $p_T > 25$ GeV and $|\eta| < 2.5$.

5.2 Single Top-quark Event Pre-selection

Single top-quark event pre-selection includes event cleaning selections, selections to enhance signal and selections specialized to reject the QCD background.

5.2.1 Event Cleaning Cuts

First, several common filters are used to reject the uninterested events. These are:

- Use only data in good runs list.

  – This is used to select the data with good quality as mention in Section 3.5.

- Require no "bad" jet of $p_T > 20$ GeV in the event.

  – "bad" jets are defined in Section 3.3.3. This is to filter out the background events that are not originated from hard scattering process.

- Have at least one primary vertex reconstructed from at least 5 tracks

  – This is used to reject events from non-collision background.

5.2.2 t-channel Event Selections

These selections are established based on the knowledge of the final states of single top-quark t-channel production from Section 4.1.

- Exactly one selected electron or muon.

- $E_T^{\text{miss}} > 25$ GeV

- Have two or three selected jets.

- Exactly one jet is a b-tagged jet.

2-jet samples are required to have exactly two jets in the events and 3-jet samples have three jets in the events. In the following contexts of this thesis, the selections without requiring 1 b-tagged jet are called pretag selection, and after 1 b-tagged jet requirement are called b-tagged selection. The samples after corresponding selections are called pretag samples and b-tagged samples. According to the lepton being a electron or a muon, the samples can also be divided into electron channel events and muon channel events.

5.2.3 The QCD multijet veto

Fake electrons from QCD-multijet events tend to have low E_T^{miss} and low transverse W mass relative to single top-quark events, hence a triangular cut using these variables is an effective way to reduce this background. The cut applied is $M_T(W) + E_T^{miss} > 60$. The selection efficiency of the triangular cut on the observed data events is 85% and on single top-quark t-channel events is 95%.

5.3   Corrections on Data and MC

There are several corrections need to be done during the analysis to correct the energy scale in data and some mis-modeling effects in Monte Carlo simulation.

- The energy of electrons in data has to be scaled in order to center the Z peak to the Z mass. In addition, the electron and muon energy MC resolution has to be smeared so that MC describes the width of the data peak. Energy/momentum smearing as well as energy scaling shifts should be propagated into the $E_\mathrm{T}^\mathrm{miss}$. These corrections need to be done before any event selection and object selection. Associated uncertainties should also be taken into account in the systematic studies.

- Due to the mis-modeling of detector and lepton reconstruction and identification effects in MC with respect to data, scale factors will be used to re-scale the acceptance term entering the cross section measurement. This includes the electron and muon trigger, identification and reconstruction scale factors

- The b-tagging algorithm performance is also calibrated with data. The scale factors are derived to correct the b-tagging efficiency and mis-tag rate in Monte Carlo. These scale factors are parameterized as a function of their relevant kinematic variables.

- Since Monte Carlo samples are produced before or during a given data taking period, only a best-guess of the data pile-up conditions can be put into the Monte Carlo. Thus, a pile-up re-weighting is done to the Monte Carlo samples at the analysis level to re-weight the pile-up conditions in Monte Carlo simulation to what is found in the data. This ensures same average interactions per bunch crossing in MC and in data.

- Finally, a luminosity-weighted scale factor is applied for Monte Carlo samples to take into account a loss of acceptance region in the electromagnetic calorimeter and to reproduce data conditions for concerned runs.

5.4   QCD-multijet Background Estimation

Since the Monte Carlo can not model the QCD-multijet background precisely, this background contribution can only be estimated using data-driven techniques. For this purpose, jet-electron samples are selected from data to model the kinematic distributions of QCD-multijet background. Then the normalization of the QCD-multijet background is obtained by performing a binned maximum likelihood fit to the E_T^{miss} distribution in the data, with multijet templates from jet-electron samples and templates of other processes (single top-quark process, $t\bar{t}$ process, W/Z+jets processes and diboson process) from Monte Carlo simulated sample [114]. In addition, a cross-check method named matrix method is briefly introduced in the last part of this section.

5.4.1   Jet-electron Model

A QCD-multijet event that can pass the single top-quark t-channel pre-selection would have one misidentified lepton in the event. The jet-electron method selects the samples from data with each event having one jet-electron, which is used as an electron but is actually a jet that has similar kinematics as an electron. The used data are selected by the jet trigger with a threshold 20 GeV. The jet-electron in the event is required to have $E_T > 25$ GeV, $|\eta| < 2.47$ and with the crack regions $(1.37 < |\eta| < 1.52)$ removal as the electron selection. The jet-electron must also contain at least four tracks, to reduce the contributions from photon conversion. The fraction of the jet-electron energy that deposited in the electromagnetic calorimeter has to be between 80% and 95%, which ensures orthogonality of the jet-electron data set to the sample of events with electron candidates.

The jet-electron samples used to model the QCD-multijet background are required to have one jet-electron in the event, no additional lepton candidates, and to pass all the other selections in the pretag selection except the E_T^{miss} requirement.

5.4.2   Normalization of QCD-multijet Background

For both electron channel and muon channel, the E_T^{miss} distribution of the jet-electron model is fitted to the E_T^{miss} distribution of data to obtain the fractions of the QCD-multijet

background in the data. The fits are done separately on the pretag data sample and b-tagged data sample to get the normalization of the QCD-multijet background in pretag events and b-tagged events, while the same template of the QCD-multijet events that from jet-electron pretag samples is used for both cases. The fitted E_T^{miss} distributions for the electron and muon channel is shown in Figure 5.1 and Figure 5.2.

(a) (b)
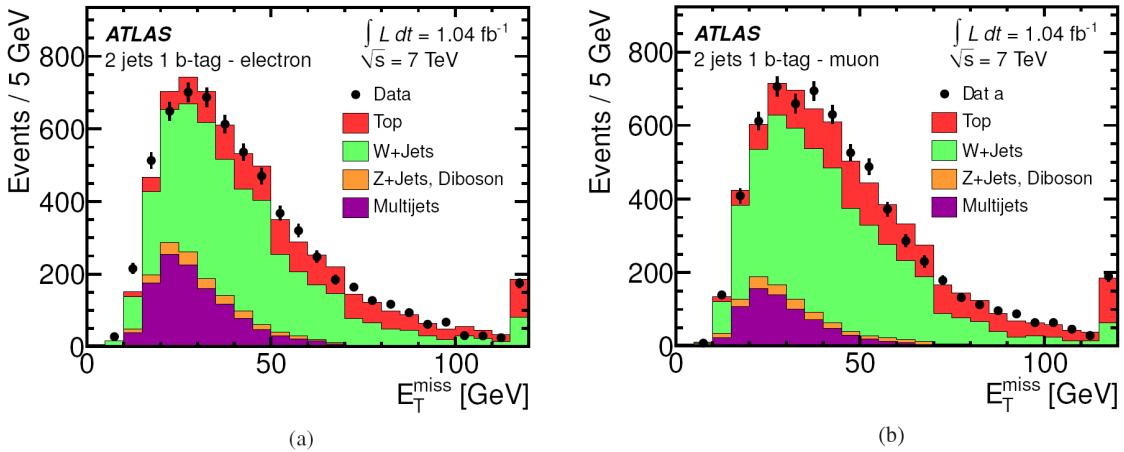
Figure 5.1: E_T^{miss} distribution for the 2-jet b-tag sample in the (a) electron and (b) muon channel [18]. A binned likelihood fit is performed to determine the fraction of multijet events in the sample. Events of $t\bar{t}$ and single-top production have been regrouped under the "Top" distribution. All processes are normalized to the fit values. The last histogram bin is the sum of the events in that bin and higher.

A summary of the QCD-multijet background estimation is given in Table 5.1.

Jet bin	Pretag events		Tagged events	
	e channel	μ channel	e channel	μ channel
1-jet	24000 ± 12000	12000 ± 6000	320 ± 160	290 ± 145
2-jet	15000 ± 7500	6800 ± 3400	710 ± 355	440 ± 220
3-jet	6000 ± 3000	1700 ± 850	580 ± 290	270 ± 135

Table 5.1: Summary of the QCD-multijet background in different jet bins of pretag and tagged events in the electron+jets and muon+jets data sets using the final uncertainty.
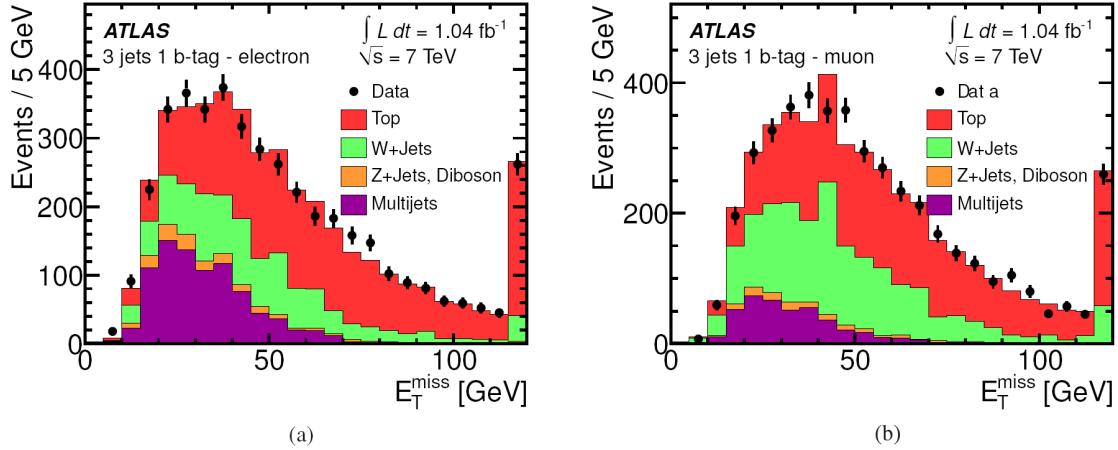
Figure 5.2: E_T^{miss} distribution for the 3-jet b-tag sample in the (a) electron and (b) muon channel [18]. A binned likelihood fit is performed to determine the fraction of multijet events in the sample. Events of $t\bar{t}$ and single-top production have been regrouped under the "Top" distribution. All processes are normalized to the fit values. The last histogram bin is the sum of the events in that bin and higher.

To evaluate the systematic uncertainty for the QCD estimation, the jet-electron data sample are divided into a high pile-up sample and a low pile-up sample based on the number of primary vertices more than 6 or less than 6. The method was reapplied to both samples to gauge the effect of pile-up on the procedure. The binned likelihood fit is also performed in a less sensitive variable, the transverse W mass, as another cross check. As a result of these studies a systematic uncertainty of 50% is assigned on the QCD-multijet rate.

5.4.3 Matrix Method Cross Check

In principle the jet-electron model should only be used to estimate the QCD-multijet background in electron channel. But it proves that the jet-electron model also fits well in the muon channel, giving good agreement between expected and the observed distribution of the kinematic variables [115]. Additionally, another approach, the matrix method, can be used to cross check the QCD-multijet background estimation in electron and muon channels.

The matrix method applies the same pre-selection on the data except the lepton definition. Two kind of leptons used in the pre-selection, named "loose" lepton and "tight"

lepton, are selected with different criteria. In the case of muon selection, the "tight" muon is the selected muon as introduced in Section 5.1, while the "loose" muon is the "tight" muon selection without the isolation requirements. Using these two kinds of muons in the pre-selection, two data samples are selected, the loose data sample and the normal data sample after pre-selection, here called the tight data sample. The number of selected loose data sample N^{loose} and the number of selected tight data sample N^{tight} can be counted and two equations are constructed as,

$$N^{loose} = N^{loose}_{real} + N^{loose}_{fake} \tag{5.1}$$

$$N^{tight} = N^{tight}_{real} + N^{tight}_{fake} = \varepsilon_{real} N^{loose}_{real} + \varepsilon_{fake} N^{loose}_{fake} \tag{5.2}$$

$$\tag{5.3}$$

In this, the muons come from W or Z decay are called real muon and muons from other sources are called the fake muon, which feature the muons in QCD-multijet events where the muons are mainly from the semi-decay of a b-hadron. ε_{real} is the real muon loose-to-tight rate and ε_{fake} is the loose-to-tight rate of the fake muon. The ε_{real} and ε_{fake} can be derived from data and will be introduce later. N^{loose}_{real} and N^{loose}_{fake} are the two unknown values in the equations that denote the number of event with a real muon and number of events with a misidentified muon in the loose data sample. In the data sample after pre-selection, the N^{tight}_{real} is the number of events with real muon and N^{tight}_{fake} is the estimation of QCD-multijet events that can be expressed by,

$$N^{tight}_{fake} = \frac{\varepsilon_{fake}}{\varepsilon_{real} - \varepsilon_{fake}} (N^{loose} \varepsilon_{real} - N^{tight}) \tag{5.4}$$

The $Z \rightarrow \mu\mu$ control sample is selected from data to derive the real muon loose-to-tight rate ε_{real}. The selections require two muons in the event with p_T above 25 GeV and different charges, the mass of the two muons satisfying 80.2 GeV $< M_{\mu\mu} <$ 100.2 GeV, the E_T^{miss} in the event below 20 GeV and one in the two muons must be "tight" muon (tagged muon). The rate of the other muon (probed muon) to be tight is used as the real muon loose-to-tight rate ε_{real}. The overall real muon loose-to-tight rate obtained with early data is close to 98%.

An iteration method is explored to estimate ε_{fake} using data. In this method, the loose data sample and tight data sample are selected as before but leave out the E_T^{miss} requirement. The control samples are selected by requiring $E_T^{miss} < 10$ GeV to these loose data sample and tight data sample. In this QCD-multijet enriched control sample, the fake muon loose-to-tight rate can be approximately given by,

$$\varepsilon_{fake}^0 = (\frac{N^{tight}}{N^{loose}})_{MET<10GeV} \tag{5.5}$$

Taking ε_{fake}^0 and ε_{real} derived before into Equation 5.4, an approximated QCD-multijet background estimation in the tight data sample in whole E_T^{miss} region can be obtained,

$$N_{fake}^{tight\,0} = \frac{\varepsilon_{fake}^0}{\varepsilon_{real} - \varepsilon_{fake}^0}(N^{loose}\varepsilon_{real} - N^{tight}) \tag{5.6}$$

The scale factor of W/Z production in the tight data sample can be calculated by,

$$k_{W/Z+jets}^1 = \frac{N^{tight} - N_{fake}^{0\,tight} - N_{t\bar{t},MC}^{tight} - N_{t,MC}^{tight}}{N_{W+jets,MC}^{tight} + N_{Z+jets,MC}^{tight}} \tag{5.7}$$

where $N_{t\bar{t},MC}^{tight}$, $N_{t,MC}^{tight}$, $N_{W+jets,MC}^{tight}$ and $N_{Z+jets,MC}^{tight}$ are the numbers of events in the Monte Carlo simulated samples of $t\bar{t}$, single top-quark t-channel, W+jets and Z+jets processes, after the same selection as the tight data sample. The scale factor can be used in Equation 5.5 and subtracting the W/Z contributions to get a refined fake loose-to-tight rate,

$$\varepsilon_{fake}^i = \frac{N^{tight} - k_{W/Z+jets}^i(N_{W+jets,MC}^{tight} + N_{Z+jets,MC}^{tight}) - N_{t\bar{t},MC}^{tight}}{N^{loose} - k_{W/Z+jets}^i(N_{W+jets,MC}^{loose} + N_{Z+jets,MC}^{loose}) - N_{t\bar{t},MC}^{loose}} \tag{5.8}$$

with $i = 1$. The ε_{fake}^1 can be taken into this loop again to get a better W/Z scale factor, resulting a more precise ε_{fake}^2. With more iteration, the ε_{fake}^i will become stable and finally gives the good approximation of ε_{fake}. Figure 5.3 illustrates the iterations of the overall loose-to-tight rate of fake muon in early data taken, where the last three iteration overlapped with each other.

The ε_{real} and ε_{fake} derived from data are using in Equation 5.4 and give the estimation of the QCD-multijet background N_{fake}^{tight}. The cross check using matrix method has been performed in early stage of the analysis with limited data. The results are compatible with the estimations using jet-electron model within 50% uncertainties.

Figure 5.3: The iterations of fake muon loose-to-tight rate calculation with different colors. The results are in one bin with y axis denoting the loose-to-tight rate of fake muons.
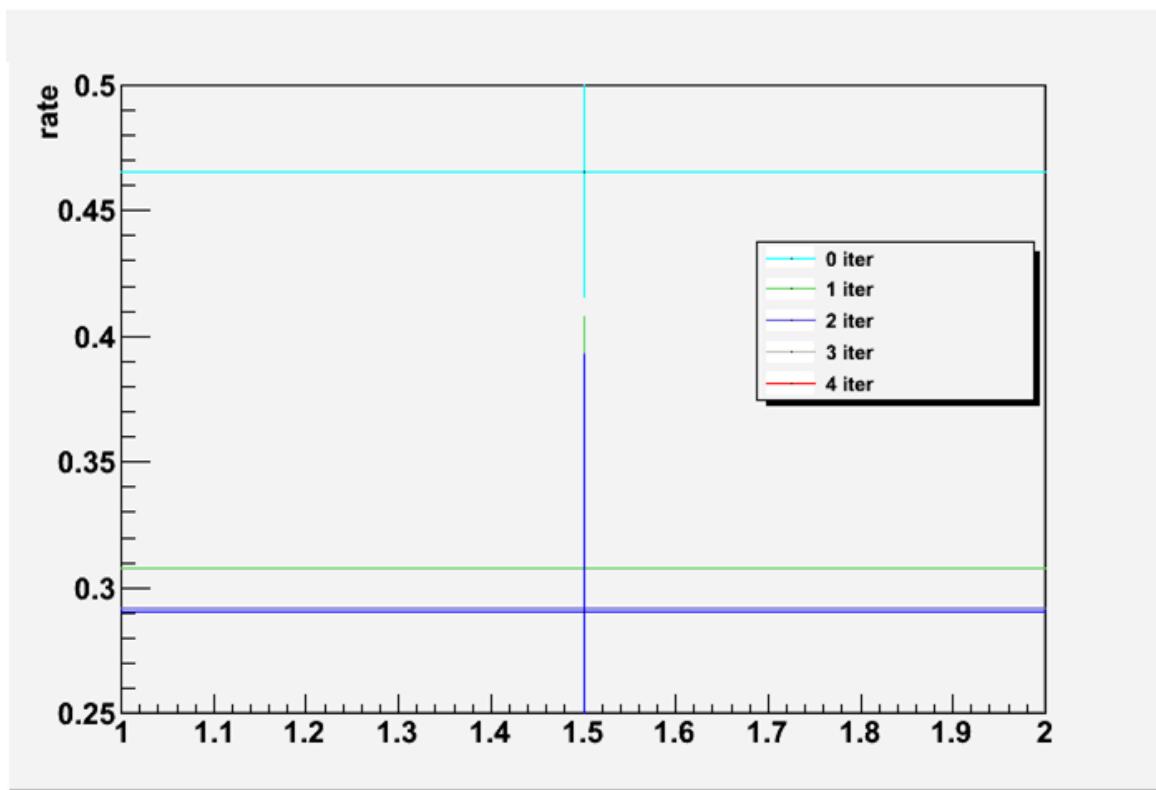
5.5   W+jets Background Estimation

W+jets events constitute a main source of background to the single top t-channel production, including the W+light jet events, Wbb events, Wcc events and Wc events. The Wbb events, Wcc events and Wc events are also collectively called W+heavy flavour jets events. The overall normalization of the W+jets background and the composition of each process with different jet flavour are derived from data, while the kinematic shape and acceptance of W+jets backgrounds are obtained from Monte Carlo simulated samples [116].

5.5.1   W+jets Total Normalization

In the pretag samples, the fraction of single top-quark t-channel signal events are negligible (less than 1%). With the QCD-multijet background estimated from data, the other contributions in pretag samples like $t\bar{t}$, Z+jets and diboson processes can be estimated using the Monte Carlo predictions by taking into account their theoretical uncertainties as the systematic uncertainties. Thus an event counting method is developed to estimate the number of W+jets events in pretag sample, which is simply taken as the data count minus all other backgrounds:

$$N_{W+jets}^{pretag} = N_{data}^{pretag} - N_{multijet}^{pretag} - N_{MC}^{pretag} \qquad (5.9)$$

N_{W+jets}^{pretag} is the number of events left after subtracting the estimated QCD-multijet and N_{MC}^{pretag} from the data. N_{MC}^{pretag} is the sum of other background events, including Z+jets, single top-quark, $t\bar{t}$, and diboson processes, estimated using Monte Carlo samples. The uncertainties of single top-quark t-channel estimated from Monte Carlo is taken as 100%.

The resulting normalization factors, calculated by dividing the estimated N_{W+jets}^{pretag} with the number predicted in W+jets Monte Carlo simulated samples, are shown in Table 5.2. The table only shows the statistical uncertainty.

5.5.2   Estimation of the W+jets Flavour Composition

The flavour composition of the W+jets sample is estimated using the pretag data samples in combination with the b-tagged data sample. The 1-jet b-tagged, 2-jet pretag and 2-jet b-tagged event samples are used as control samples to construct three equations with the

sample	normalization factor
	combined
W+1jet pretag	0.966 ± 0.001 (stat)
W+2jet pretag	0.914 ± 0.002 (stat)
W+3jet pretag	0.879 ± 0.004 (stat)

Table 5.2: Data/MC W+jets pretag normalization factors extracted from the muon and electron samples combined together with the uncertainty due to data statistics [116].

three unknown fractions of Wbb, Wc and W+light jets in 2-jet pretag sample, $F_{bb,2}^{pretag}$, $F_{c,2}^{pretag}$ and $F_{l,2}^{pretag}$, while the fraction of Wcc events is obtained by multiply a correction factor $k_{cc \to bb}^{pretag}$ with $F_{bb,2}^{pretag}$, where the $k_{cc \to bb}^{pretag}$ denoting $F_{cc,2}^{pretag,\,MC}/F_{bb,2}^{pretag,\,MC}$ is obtained from MC samples. The three equations are:

$$N_{data-bkg,2}^{pretag} = N_{data-bkg,2}^{pretag}(F_{bb,2}^{pretag} + k_{cc \to bb}^{pretag} F_{bb,2}^{pretag} + F_{c,2}^{pretag} + F_{l,2}^{pretag}),$$

$$N_{data-bkg,2}^{tag} = N_{data-bkg,2}^{pretag}(F_{bb,2}^{pretag} P_{bb,2}^{tag} + k_{cc \to bb}^{pretag} F_{bb,2}^{pretag} P_{cc,2}^{tag} + F_{c,2}^{pretag} P_{c,2}^{tag} + F_{l,2}^{pretag} P_{l,2}^{tag}),$$

$$N_{data-bkg,1}^{pretag} = N_{data-bkg,2}^{pretag}(F_{bb,2}^{pretag} k_{bb,2 \to 1}^{pretag} + k_{cc \to bb}^{pretag} F_{bb,2}^{pretag} k_{cc,2 \to 1}^{pretag} + F_{c,2}^{pretag} k_{c,2 \to 1}^{pretag}$$
$$+ F_{l,2}^{pretag} k_{l,2 \to 1}^{pretag}).$$

Here $N_{data-bkg,2}^{pretag}$, $N_{data-bkg,2}^{tag}$ and $N_{data-bkg,1}^{pretag}$ are the estimated W+jets event numbers in each control sample, which are obtained similar as Eq. 5.9. $P_{bb,2}^{tag}$, $P_{cc,2}^{tag}$, $P_{c,2}^{tag}$ and $P_{l,2}^{tag}$ are the acceptances of the individual flavour processes after b-tagged selection with respect to the pretag selection, calculated from MC samples. $k_{bb,2 \to 1}^{pretag}$, $k_{cc,2 \to 1}^{pretag}$, $k_{c,2 \to 1}^{pretag}$ and $k_{l,2 \to 1}^{pretag}$ are the projection factors derived from MC samples by dividing the fractions in 1-jet pretag MC sample to the fractions in 2-jet MC sample for each flavour process. The fractions $F_{bb,2}^{pretag}$, $F_{c,2}^{pretag}$ and $F_{l,2}^{pretag}$ are determined by solving the three equations.

The correction factors K_{bb} (same as K_{cc}), K_c and K_{light} are derive to be used in analysis, correcting the fractions in MC samples, $F_{bb,2}^{pretag,MC}$, $F_{c,2}^{pretag,MC}$ and $F_{l,2}^{pretag,MC}$ to the ones

estimated from data,

$$K_{bb} = \frac{F_{bb,2}^{pretag}}{F_{bb,2}^{pretag,MC}}, \qquad K_c = \frac{F_{c,2}^{pretag}}{F_{c,2}^{pretag,MC}}, \qquad K_l = \frac{F_{l,2}^{pretag}}{F_{c,2}^{pretag,MC}}, \qquad (5.10)$$

The resulting correction factors are shown in Table 5.3.

K-factor	K_{bb}	K_{light}	K_c
Value	1.371±0.082(stat)±0.964(sys)	0.914±0.004±0.106	1.282±0.036±0.327

Table 5.3: Flavour factor K for each W+jets flavour for the muon and electron samples combined, with statistical and systematic uncertainties [116].

5.5.3   Total W+jets Scale Factors

The total correction factors for each W+jets flavour sample are then derived from the above flavour factors and then multiplied by the overall normalization factor for each jet multiplicity bin from Table 5.2, including the projection factors for 1, and 3 jet events derived from the MC samples. The final correction factors are shown in Table 5.4.

jet bin	K_{bb}	K_{light}	K_c
W+1jet	1.361±0.090(stat)±0.950(sys)	0.908±0.004±0.260	1.273±0.040±0.390
W+2jet	1.252±0.080(stat)±0.860(sys)	0.835±0.004±0.210	1.172±0.040±0.290
W+3jet	1.182±0.070(stat)±0.870(sys)	0.788±0.004±0.330	1.106±0.040±0.400

Table 5.4: Final correction factor K for each W+jets flavour for the muon and electron samples combined, with statistical and systematic uncertainties [116].

The W+jets normalization and flavour composition estimate includes a 100% single top-quark cross-section uncertainty, as well as the theoretical cross-section uncertainties of $t\bar{t}$, Z+jets and diboson processes. An extra 25% systematic uncertainty is added to cover the projection factor uncertainty obtained from the effect of Alpgen variations on the heavy-flavour content of W+Jets events. The uncertainty of QCD-multijet background estimation,

the jet energy scale uncertainty, the b-tag and light tag rate uncertainties are also taken into account in the systematic uncertainties of W+jets estimations. The W+jets total uncertainties are the sum in quadrature of the statistical and systematic uncertainties and are shown in the event yields table in Section 5.6.

5.5.4 W+jets Scale Factor Checks

In the W+jets flavour composition estimation, the used 2-jet b-tagged control samples have been subtracted the contributions of single top-quark t-channel signal events that selected by cut-based analysis (See Chapter 6 for an introduction of cut-based analysis). The signal selection in cut-based analysis requires η of light jet above 2.0, total transverse energies in the event larger than 210 GeV, the reconstructed top mass 150 GeV $< M_{top} < 190$ GeV, and $\Delta\eta$ between the b-tagged jet and light jet satisfying $|\Delta\eta(b-jet, l-jet)| > 1.0$. While the boosted decision trees analysis selects signal events with the constructed multivariate discriminant as described in Chapter 6, resulting different signal region with respect to the cut-based selection. To make sure the boosted decision tree analysis are not biased by the W+jets scale factors, one simple check is made by re-calculating the W+jets scale factor using the 2-jet pretag control sample with the rejection of the signal events selected by the boosted decision trees discriminant. As a result, the new W+jets scale factors agree very well with the ones calculated for cut based analysis. The difference are within statistical uncertainties, as shown in table 5.5.

W+jets Scale Factor	K_{bb}	K_{light}	K_c
Cut based	1.252±0.090(stat)	0.835±0.004(stat)	1.172±0.004(stat)
BDT Analysis	1.229±0.082(stat)	0.836±0.003(stat)	1.178±0.037(stat)

Table 5.5: 2-jets channel correction factor K for each W+jets flavour for the muon and electron samples combined, with statistical uncertainties [116].

5.6 Event Yields after Pre-selection

Tables 5.6 and 5.7 list the event yields after event selection and background estimation for the electron channel and muon channel, respectively.

The multijet event yields and contributions from W+jets events are determined with data-driven techniques as introduce before. $t\bar{t}$, other top (single top-quark s- and Wt-channel), Z+jets, Diboson and the single top-quark t-channel signal expectation are normalized to theoretical cross sections. The event yields of all these processes are summed to the total expected event yields.

After btagged selection,the predicted single top t-channel fraction in the data is about 9% in 2-jet sample and 8% in 3-jet sample. The major backgrounds are $t\bar{t}$, W+jets and QCD-multijet backgrounds.

	Pretag electron		B-tagged electron	
	2-jets	3-jets	2-jets	3-jets
t-channel	908±34	614±23	452±17	298±11
$t\bar{t}$, Other top	1689±112	3462±253	787±53	1702±125
W+light jets	71005±21465	18803±8210	350±105	126±55
W+heavy flavour jets	30080±7813	9095±3004	2628±746	1109±405
Z+jets, Diboson	11257±6106	4428±2405	158±63	95±44
Multijets	15000±7500	6000±3000	710±355	580±290
TOTAL expected	129940±24786	42403±9551	5084±838	3910±518
DATA	129217	39750	5021	3592

Table 5.6: Predicted and observed event yields, after selection, in the electron 2-jet and 3-jet b-tagged samples. The uncertainties on the multijet and the W+jets yields are calculated including all systematic and statistic uncertainties in the estimation. Uncertainties on these predictions are only reflecting the uncertainties on the theoretical cross section prediction.

	Pretag muon		B-tagged muon	
	2-jets	3-jets	2-jets	3-jets
t-channel	999±37	651±24	488±18	319±12
$t\bar{t}$, Other top	1682±111	3481±256	787±52	1709±125
W+light jets	89633±27097	22481±9823	494±149	204±89
W+heavy flavour jets	35885±9375	10477±3505	3093±872	1248±473
Z+jets, Diboson	7964±3986	2423±1187	163±60	77±30
Multijets	6800±3400	1700±850	440±220	270±135
TOTAL expected	142963±29148	41173±10533	5464±916	3829±518
DATA	149941	42005	5592	3915

Table 5.7: Predicted and observed event yields, after selection, in the muon 2-jet and 3-jet b-tagged samples. The uncertainties on the multijet and the W+jets yields are calculated including all systematic and statistic uncertainties in the estimation. Uncertainties on these predictions are only reflecting the uncertainties on the theoretical cross section prediction.

Chapter 6

BOOSTED DECISION TREES AND CROSS SECTION MEASUREMENT

After the single top-quark event pre-selection, the predicted fraction of single top-quark t-channel signal is less than 10% in the selected data. It is impossible to perform a cross section measurement since the uncertainties of the background estimation are larger than the predicted number of signal events. More powerful discriminants are needed to further extract signal events and suppress backgrounds. For this purpose, three different approaches are explored, the cut-based (CB) analysis [116], the boosted decision trees [117, 118] (BDT) analysis [119] and the neural network [120, 121] (NN) analysis [115]. The cut-based approach applies additional selections on the b-tagged samples after pre-selection to enhance the signal significance, where in each selection one discriminating variable is used. In contrast BDT analysis and NN analysis explore the multivariate techniques, which simultaneously analyze multiple variables and combine them into a single discriminant. Even poorly discriminant variables can be exploited in a multivariate approach and thus contribute to improve the separation of the signal and the background. The correlations of different variables are also properly taken into account with multivariate techniques. Among many multivariate methods, boosted decision trees present a clear, logical model that can be understood easily and their performances are insensitive to the inclusion of poorly discriminating input variables. These give a transparent and flexible control of the method to achieve physics purpose.

This chapter first gives an introduction of the boosted decision trees technique. Then the details of the implementation of boosted decision trees method are described. Later section describes the methods of cross section measurement and systematic uncertainty estimation. The results of single top-quark t-channel cross section measurement and $|V_{tb}|$ determination are given in the following section. Finally the measurement are concluded and possible improvements in future are discussed.

6.1 Introduction of Boosted Decision Trees

In the present analysis, boosted decision trees discriminator is employed, using the ROOT Toolkit for Multivariate Data Analysis (TMVA) [122]. With this approach, a significantly improved sensitivity can be reached with respect to the pre-selection shown in chapter 5.

Boosted decision trees study a large number of input variables in the training samples, which are the Monte Carlo simulated samples with known knowledge of signal and background events. The performance of the trained boosted decision trees is then tested to with an independent set of MC samples. In this analysis, all MC samples that have passed b-tag pre-selection are divided in two independent parts of equal size for the training and test respectively[1]. Single top-quark t-channel simulated samples weighted to its prediction are used for signal. And a mixture of $t\bar{t}$, W+jets, dibosons and jet-electron samples all weighted according to their relative abundance as introduced in Section 5.6 are used as background. The total training and test samples are composed each from 50% signal events and 50% background events.

With the training samples, boosted decision trees perform sequential selections on the variables in the event to separate signal from backgrounds. At each step of the sequential selection, the variable that gives the best separation between signal and background is chosen and a threshold is determined on this variable value. The combination of all decisions form a tree structure classifier, named a decision tree. More decisions trees are generated to reduce the statistical fluctuations by reweighting the samples used. Finally, results from all decision trees are combined to construct a multivariate discriminant.

6.1.1 Decision Tree

A decision tree is a binary tree structured of nodes where each father node can have up to two child nodes. An illustration of a decision tree is shown in Figure 6.1. From the top node of the tree, repeated yes/no decisions are performed on a single variable at a time and split the father node into child nodes until some stop criterion is reached. The resulting terminal

---

[1]Ideally one should divide the sample in three parts of equal size: train, test and yield, but here due to limited MC statistics only two part were considered.

nodes are called leaves. With this method the phase space is split into regions that are eventually classified as signal or background, depending on the majority of training events that end up in the final leaf nodes.
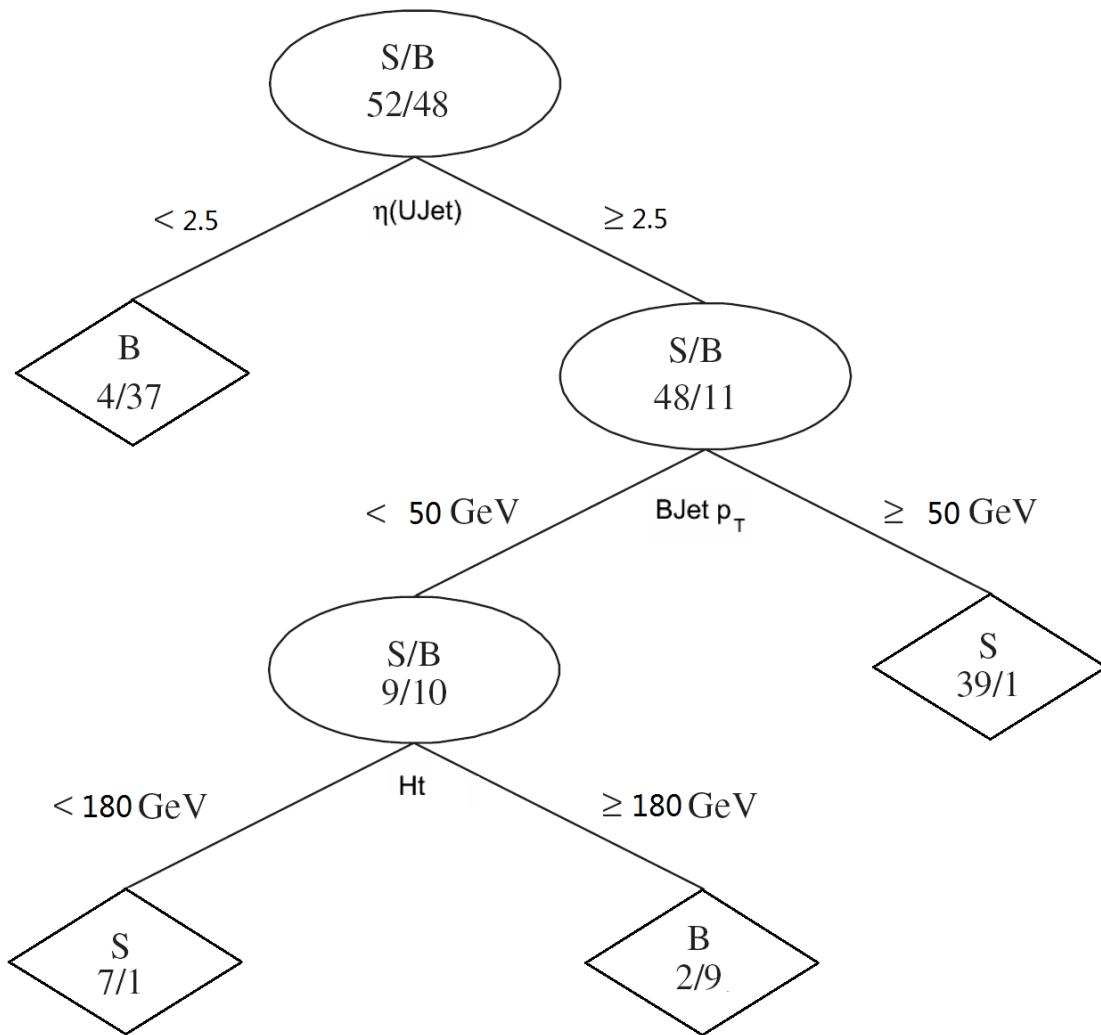

Figure 6.1: An illustration of a decision tree.

Splitting

The splitting criterion for each node is defined during the training of the tree. A variety of separation criteria can be configured to assess the performance of a variable and a specific selection. The criterion chosen in this analysis is the *Gini* index, defined by

$$Gini = (\sum_{i=1}^{n} W_i)p(1-p), \tag{6.1}$$

where p is the purity of a node, W_i is the weight of a event i, n represents the total event number in the node. The purity p of a node can be expressed by,

$$p = \frac{\sum_s W_s}{\sum_{i=1}^{n} W_i}. \tag{6.2}$$

Here $\sum_s W_s$ is the sum of weighted signal events. Note that *Gini* is 0 if the sample is pure signal or pure background. The training procedure selects the variable and cuts values that optimize the increase in the separation between the father and the child nodes. In the case of *Gini* index, it is maximize

$$Increase = Gini(\text{father}) - Gini(\text{left child}) - Gini(\text{right child}), \tag{6.3}$$

which is also referred as the goodness or gain of the split. In this optimization, all input variables are looped over and the cut values are scanned over the variable range with a granularity of preset *nCuts* bins.

Stop Criterion and Pruning

With the increasing number of splitting in the decision tree, the samples size is reduced and the relative statistical uncertainties are growing. A decision tree with too many nodes and leaves could lead to final leaves dominated by statistical fluctuations. Another risk of the training of a decision tree is called overtraining problem. Overtraining refers that the decision tree overfits training samples and its performance only features this specific training samples. While using another independent samples for the training would lead to very different outcomes. To reduce statistically insignificant nodes and reduce the overtraining of the trees, the stop criterions and pruning methods are explored.

One stop criterion of a decision tree is the $MaxDepth$, which denotes the maximum layers of a decision tree. The depth of a root node is 0. Another stop criterion is $nEventsMin$, which requires a minimum number of events in terminal leaves. Note that the event number used here is weighted event number.

The pruning method chosen here is the so-called Cost Complexity pruning [123]. It defines misclassification rate of a node with

$$R = 1 - max(p, 1 - p). \tag{6.4}$$

The misclassification rate of the subtree of the node is referred as R_{subtree}. The cost complexity for this node is then defined by

$$\rho = \frac{R - R_{\text{subtree}}}{N_{\text{nodes of subtree}} - 1} \tag{6.5}$$

The node with the smallest ρ value in the tree is recursively pruned away as long as $\rho < PruneStrength$, where $PruneStrength$ is a value set by users. If the $PruneStrength$ option is set to a negative value, an algorithm attempts to automatically detect the optimal strength parameter. The training sample is then divided into two subsamples, of which one is used for training with different $PruneStrength$, while the other one serves for validating the performance of the pruning.

6.1.2   Boosting

A single decision tree are extremely sensitive to the training samples. Slightly different training samples can lead to very different trees. This limitation can be overcame by using boosting methods. The boosting of a decision tree derives several decision trees (a forest) from the same training sample by reweighting misclassified events. All boosted decision trees are combined to form a classifier which is given by a weighted majority vote of the individual decision trees. The boosting algorithm used in the present analysis is an adaptive boost method called AdaBoost [124]. It calculates a boosting parameter for the mth tree,

$$\alpha_m = \beta ln(\frac{1 - \epsilon_m}{\epsilon_m}), \tag{6.6}$$

where β is a parameter default set 1 in AdaBoost, ϵ_m is the misclassification error rate of mth tree, defined as,

$$\epsilon_m = \frac{\sum_{i=1}^{n} W_i I_i}{\sum_{i=1}^{n} W_i} \tag{6.7}$$

where $I_i = 1$ if the i event is misclassified and 0 otherwise. The boosting changes the weight of event by

$$W_i \to W_i \times e^{\alpha_m I_i} \tag{6.8}$$

and renormalizes the event,

$$W_i \to \frac{W_i}{\sum_{i=1}^{n} W_i} \tag{6.9}$$

A new decision tree is boosted using the reweighted samples. The total number of boosted decision trees is controlled by BDT option $NTrees$.

6.1.3 Output of Boosted Decision Trees

At the end of a trained decision tree, if a leaf has purity $p > \frac{1}{2}$ ($\frac{1}{2}$ is default value), then it is called a signal leaf, otherwise, a background leaf. With a given event x, the trained decision tree will process the variables of this event and land the event on either a signal leaf or a background leaf, giving a score of the event $T(X) = 1$ or $T(X) = -1$ accordingly. For m decision trees boosted by AdaBoost method, The final BDT weight of event x is the weighted sum of each tree output,

$$T(X) = \sum_{m=1}^{M} \alpha_m T_m(X). \tag{6.10}$$

The BDT weights of data events are used as the multivariate discriminators to distinguish signal from backgrounds.

6.2 Application of Boosted Decision Trees

This section describes the selection of the variables used in boosted decision trees, the optimization of the BDT method and its validation. The sensitivity to high pile-up events of trained boosted decision trees is also checked in the final part of this section.

6.2.1 Selection of Discriminant Variables

The list of variables entering a BDT event classifier is derived from a procedure of optimization that selects only the variables that bring a significant discrimination between signal and the considered background.

The discriminating power of a given variable is computed using the separation power

$$S^2 = \frac{1}{2} \int \frac{(s(x) - b(x))^2}{s(x) + b(x)} dx,$$

where $s(x)$ and $b(x)$ are the probability density, for signal and background respectively, for this variable. A large set of kinematical variables was tested, including the 4 momentum variables of objects like b-tagged jet, light jet, lepton, E_T^{miss}, reconstructed W and reconstructed top quark, event kinematics such as $M_T(W)$, H and H_T of various object combination, angular correlation variables between all kinds of objects and some event variables like sphericity and aplanarity. In total, more than 70 variables are considered. Tables 6.1 and 6.2 list the 14 most discriminating variables, among those tested, that are used in the 2-jet and 3-jet channels, respectively.

- $M\_top(l\nu b)$: Top-quark mass reconstructed from the b-tagged jet, charged lepton and neutrino. The transverse momentum of the neutrino is given by the x- and y- components of the E_T^{miss}vector, while the unmeasured z-component of the neutrino momentum $p_z(\nu)$ is inferred by imposing a W-boson mass constraint on the lepton-neutrino system. The solution that gives smaller $p_z(\nu)$ is chosen in this calculation.

- $\eta(UJet)$: Pseudorapidity of the leading untagged jet.

- Ht: Scalar sum of the transverse momenta of the jets, the charged lepton and the missing transverse energy.

1	$M\_top(l\nu b)$	8	$\Delta\eta(UJet, Lepton)$
2	$\eta(UJet)$	9	$E_{\mathrm{T}}^{\mathrm{miss}}$
3	Ht	10	$E(Lepton)$
4	$p_T(BJet)$	11	$Ht\_Deviation$
5	$\Delta R(BJet, Lepton)$	12	$M(Jet1, Jet2)$
6	$M(BJet)$	13	$M_T(W)$
7	$\Delta\eta(W, BJet)$	14	$Sphericity$

Table 6.1: Variables ranking for 2-jet channel BDT training

1	$\eta(UJet)$	8	$\Delta\eta(W, BJet)$
2	$Sphericity$	9	$\Delta R(BJet, Lepton)$
3	$M\_top(l\nu b)$	10	$M(BJet)$
4	$\Delta\eta(UJet, Lepton)$	11	$Ht\_Deviation$
5	$E(Lepton)$	12	$p_T(BJet)$
6	$M_T(W)$	13	$E_{\mathrm{T}}^{\mathrm{miss}}$
7	Ht	14	$M(Jet1, Jet2)$

Table 6.2: Variables ranking for 3-jet channel BDT training

- $p_T(BJet)$: Transverse momentum of the b-tagged jet.

- $\Delta R(BJet, Lepton)$: The distance, $\Delta R = sqrt(\Delta\eta^2 + \Delta\phi^2)$, between the b-tagged jet and the charged lepton.

- $M(BJet)$: Invariant mass of the b-quark jet.

- $M_T(W)$: Transverse mass of the W-boson, reconstructed using the same neutrino and lepton as in $M\_top(l\nu b)$.

- $\Delta\eta(W, BJet)$: Difference in η between the reconstructed W-boson and the b-tagged jet.

- $\Delta\eta(UJet, Lepton)$: Difference in η between the untagged jet and charged lepton.

- E_T^{miss}: Reconstructed missing transverse energy.

- $E(Lepton)$: Energy of the charged lepton.

- $Ht\_Deviation$: Ratio of the scalar sum of the transverse momenta of the leading jet, the charged lepton and the missing transverse energy over Ht:

$$Ht\_Deviation = \frac{E_T^{\mathrm{miss}} + p_T\_leadingJet + p_T\_Lepton}{Ht}$$

- $M(Jet1, Jet2)$: Invariant mass of the two leading jets in the event.

- Sphericity: Sphericity is a measurement of the sum of squared transverse momentum, with respect to the event axis, of the lepton and jets in the event. Sphericity of an isotropic event tends to be 1.

    - The sphericity tensor: $S^{\alpha\beta} = \sum_i p_i^\alpha p_i^\beta / \sum_i |p_i|^2$, where i is an index running over the particles of the event, and $\alpha, \beta = 1, 2, 3$.
    - 3 eigenvalues λ_1, λ_2 and λ_3 are obtained by diagonalization of $S^{\alpha\beta}$, $\lambda_1 \geq \lambda_2 \geq \lambda_3$

– Sphericity= $1.5 * (\lambda_2 + \lambda_3)$.

– Aplanarity= $1.5 * \lambda_3$.

• Aplanarity: Aplanarity is an event shape variable. Aplanarity of a planar event is close to 0 and it is close to $\frac{1}{2}$ for an isotropic event.

Figures 6.2 and 6.3 shows the normalized distribution of 4 most discriminant variables used in boosted decision tree, for signal and background 2-jet and 3-jet events. More distributions are shown in Appendix A.
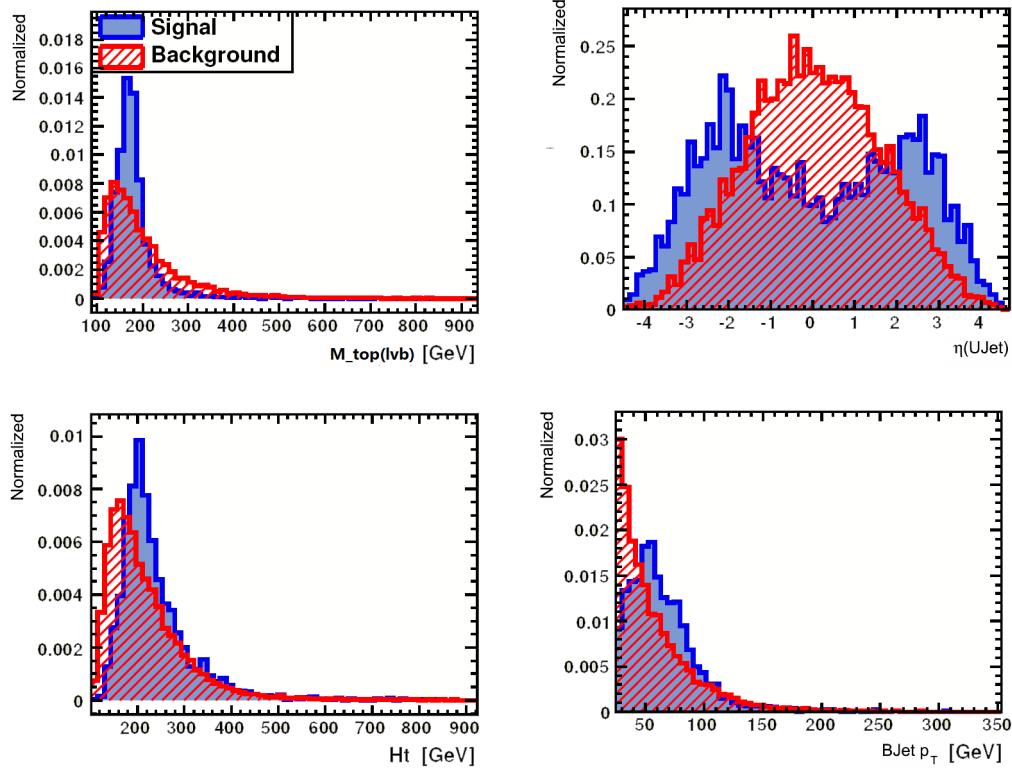

Figure 6.2: Normalized distribution of the most discriminant variables for signal (blue) and background (red) for 2-jet events.
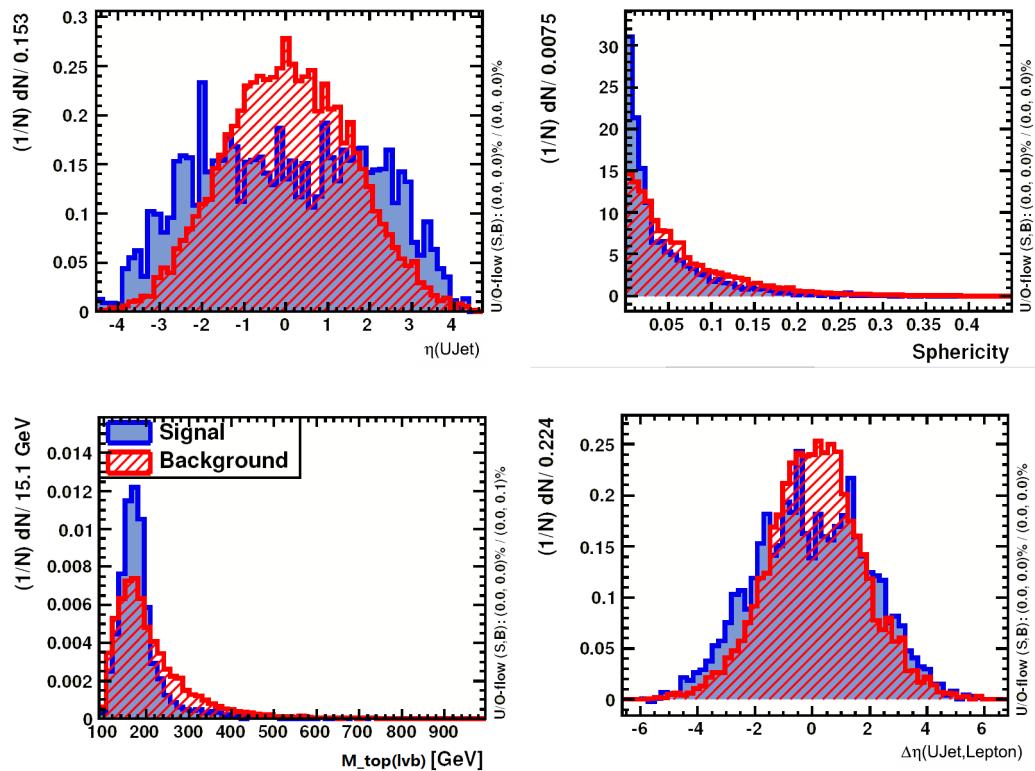
Figure 6.3: Normalized distribution of the most discriminant variables for signal (blue) and background (red) for 3-jet events.

6.2.2   Variable Correlations

One of the advantage of the boosted decision trees analysis is that all well modeled variables can be used as input, even if they have low separation power or high correlations. As introduced in Section 6.1.1, in each split of the decision tree all input variables will be looped and only the best variable will be used. Including more variables gives more choice for the boosted decision trees to make a better decision. But to keep analysis simple and easy to control, a reasonably short list of variables is preferred. Highly correlated variables that contribute little in improving BDT performance are removed from the list of variables used.

The linear correlations between variables are shown in Figure 6.4 and Figure 6.5. Some variables are quite correlated but are still used in BDT since they help to improve the BDT performance.
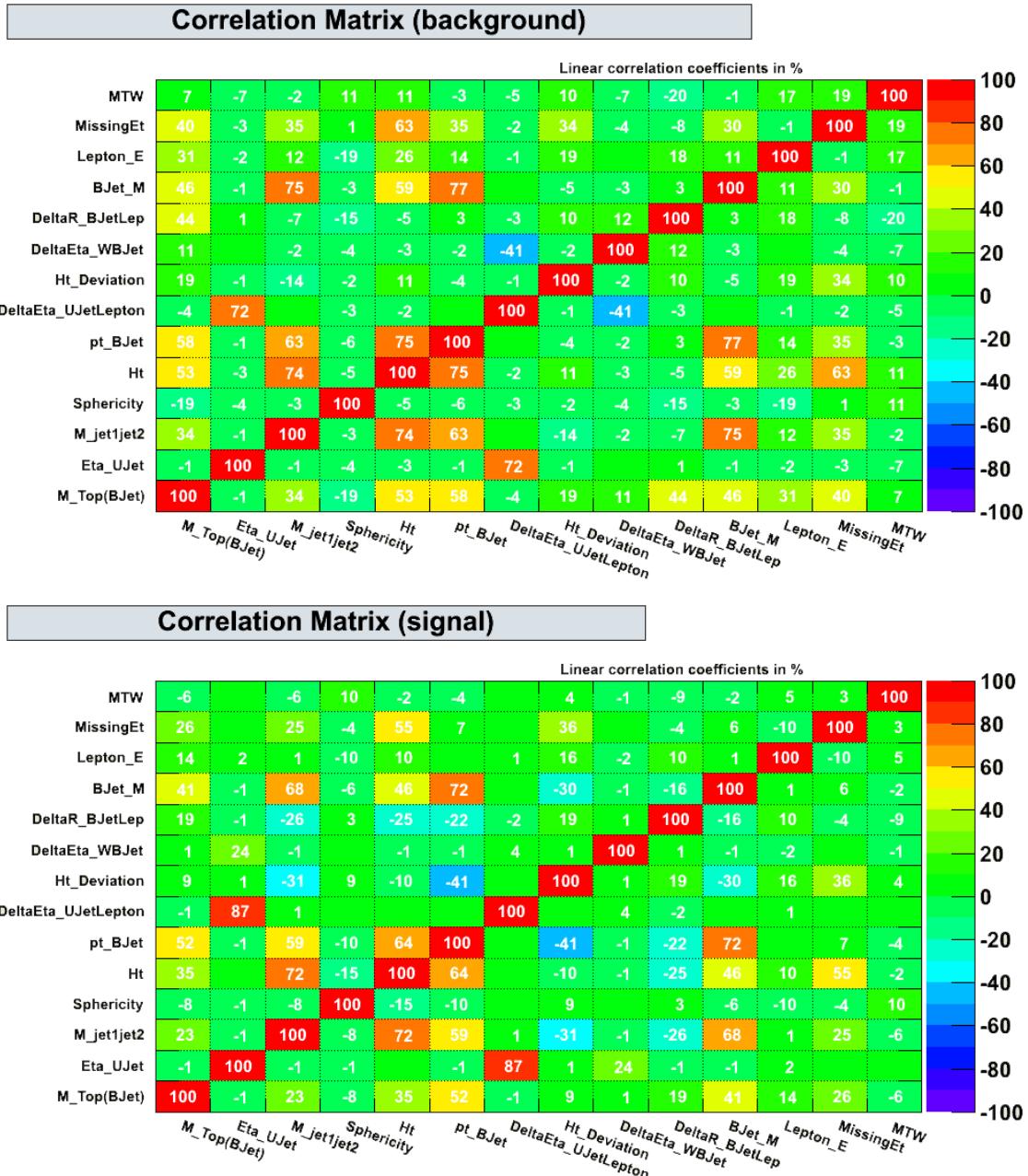
Figure 6.4: correlation matrices of input variables for signal and background in 2-jet channel.

110
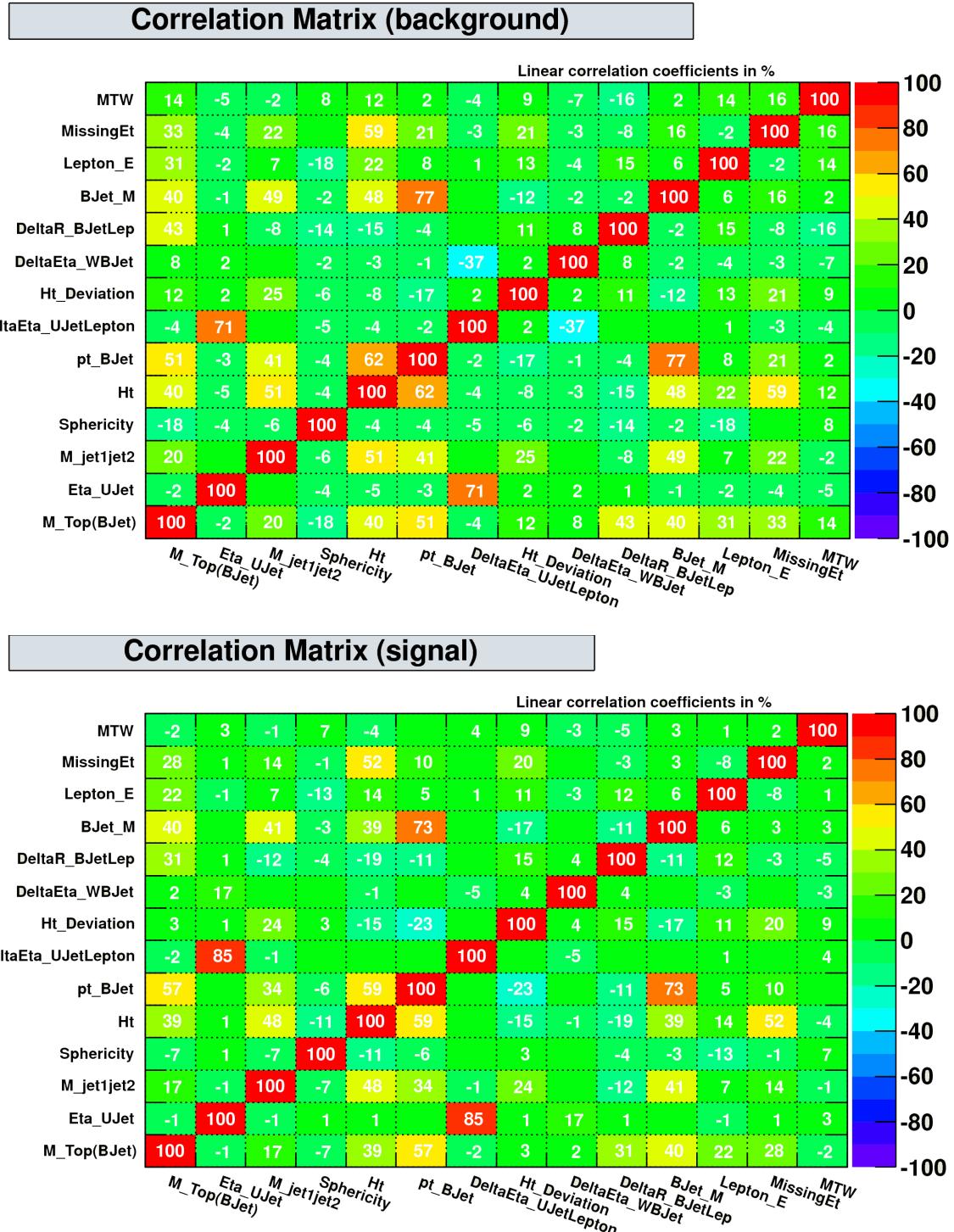
Figure 6.5: correlation matrices of input variables for signal and background in 3-jet channel.

6.2.3   Boosted Decision Trees Optimization

As introduced in previous sessions, there are several main configuration options in the training of boosted decision trees.

- *nCuts*: the number of bins used to optimize the cuts value on the variables in the splitting. Different choices of *nCuts* from 5 to 50 have been tested in the optimization.

- *nEventsMin*: minimum event number requirement in a terminal leaf node. In the optimization, the numbers from 5 to 100 have been used.

- *MaxDepth*: the maximum-layer limitation of a decision tree. The BDT performances with depths from 2 to 6 are examined.

- *NTrees*: the total number of boosted decision trees. Numbers of trees from 20 to 2000 are tested in the optimization.

- *PruneMethod* and *PruneStrength*: options to choose pruning and set pruning strength. *NoPruning* and *PruneStrength* from -1 to 10 have been tested.

The optimization of the BDT starts from examining the overtraining of the BDT and the continuity of the BDT output. The overtraining of the BDT is described by the Kolmogorov-Smirnov test results, which is the likelihood that the distribution obtained from the test sample could have been obtained from the training sample. The likelihood value is required to be larger than 0.1 to make sure of the compatibility between the BDT distribution of training sample and test sample. In the optimization it is discovered that the overtraining increase significantly if the *MaxDepth* is large than 3. The Kolmogorov-Smirnov test results of the BDTs for 2-jet channel and 3-jet channel are shown in Figures 6.6a and 6.7a. *NTrees* has to be larger than 50 to have a continuous BDT output and it is further tuned in next step of optimization.

Then different BDTs with different combination of configuration values are tested to achieve larger signal significance. It is done by checking the background rejections of dif-
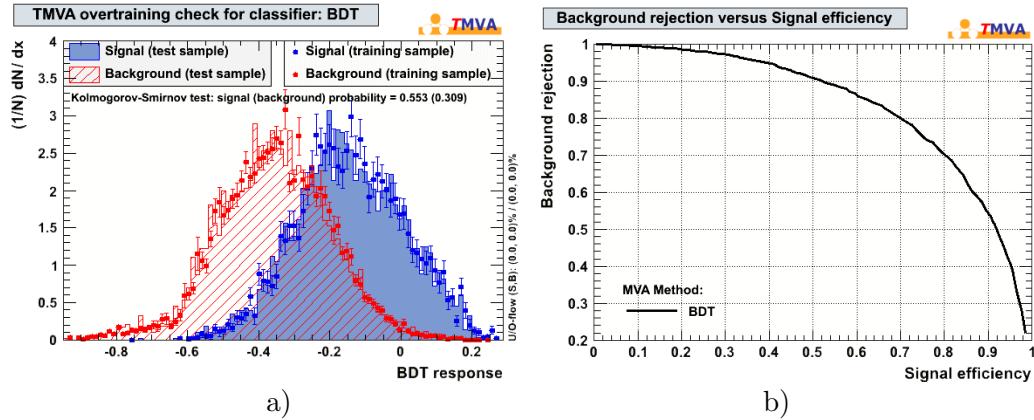
Figure 6.6: TMVA control plots for 2-jet events - a) Overtraining checks for signal (blue) and background (red) in the train and test samples, b) background rejection vs signal efficiency.
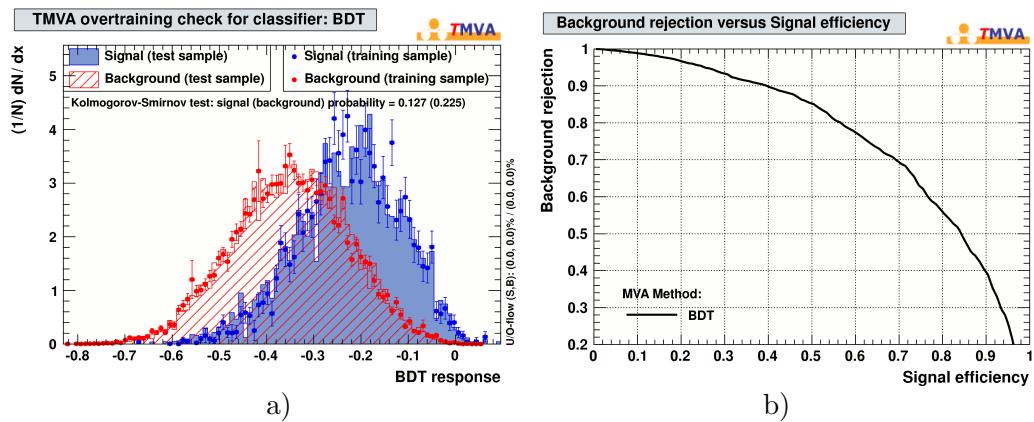

Figure 6.7: TMVA control plots for 3-jet events - a) Overtraining checks for signal (blue) and background (red) in the train and test samples, b) background rejection vs signal efficiency.

ferent BDTs with the same signal efficiency level. The signal efficiency and background rejection curves for 2-jet BDT and 3-jet BDT are shown in Figures 6.6b and 6.7b.

BDT settings are further optimized to make sure of the good agreements between BDT distributions of Monte Carlo simulated samples and of data samples. Too optimistic settings or including some variables that are not well modeled could lead to obvious deviations. The validation plots with final BDT options are shown in Section 6.2.4.

The impact of the different BDT configurations on systematic uncertainties are also examined. The final BDT optimization is the results of balancing overtraining, validation and systematic uncertainties. A summary of all BDT settings used for the 2-jet and 3-jet channels are shown in Tables 6.3 and 6.4. After training, the normalized BDT outputs of signal and backgrounds are shown in Figure 6.8. In this plot, "top" background includes $t\bar{t}$, single top-quark s-channel and Wt-channel backgrounds.

SeparationType=GiniIndex	nCuts=10
nEventsMin=50	MaxDepth=3
NTrees=100	BoostType=AdaBoost
PruneMethod=NoPruning	

Table 6.3: Boosted decision trees settings for 2-jet channel

SeparationType=GiniIndex	nCuts=20
nEventsMin=30	MaxDepth=3
NTrees=175	BoostType=AdaBoost
PruneMethod=CostComplexity	PruneStrength=-1

Table 6.4: Boosted decision trees settings for 3-jet channel
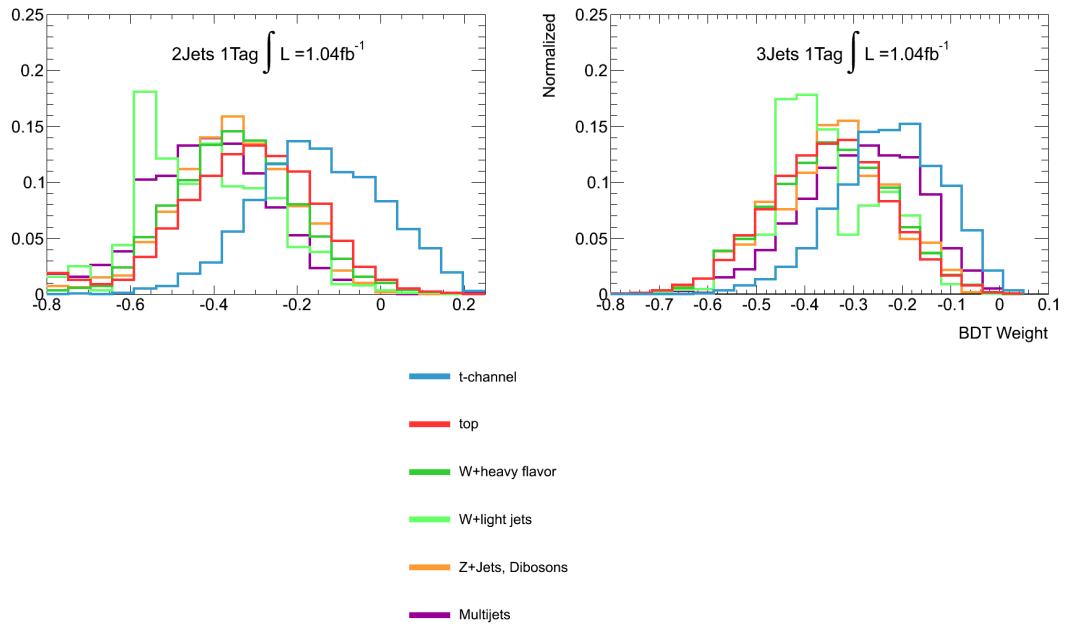
Figure 6.8: Normalized BDT output of signal and background for the 2-jet and 3-jet channel in the b-tagged sample (electron and muon samples combined).

6.2.4   Validation of the Variables

To make sure the reliability of the BDT performance, it is important to validate all input variables that they are well modeled. This is done by testing the variable distribution agreements between data and simulated samples. Here, single top-quark, $t\bar{t}$, Z+jets and diboson Monte Carlo samples have been normalized to their theoretical prediction, while multijet and W+jets backgrounds are normalized to their estimations using data-driven methods as introduced in Section 5.4 and Section 5.5.

The stacked distribution of the five most discriminant variables in the 2-jet and 3-jet pretag and b-tagged samples are shown in Fig 6.9, Fig 6.10 and in Fig 6.11, Fig 6.12, respectively. In these plots, "top" background includes $t\bar{t}$, single top-quark s-channel and Wt-channel backgrounds. All distributions of the variables used in the BDT are shown in Appendix A.

The stacked BDT distributions are shown in Figures 6.13 and 6.14 for the 2-jet and 3-jet b-tagged samples, respectively.

A reasonable agreement is achieved for all variables considered and for the combined BDT discriminant.

116
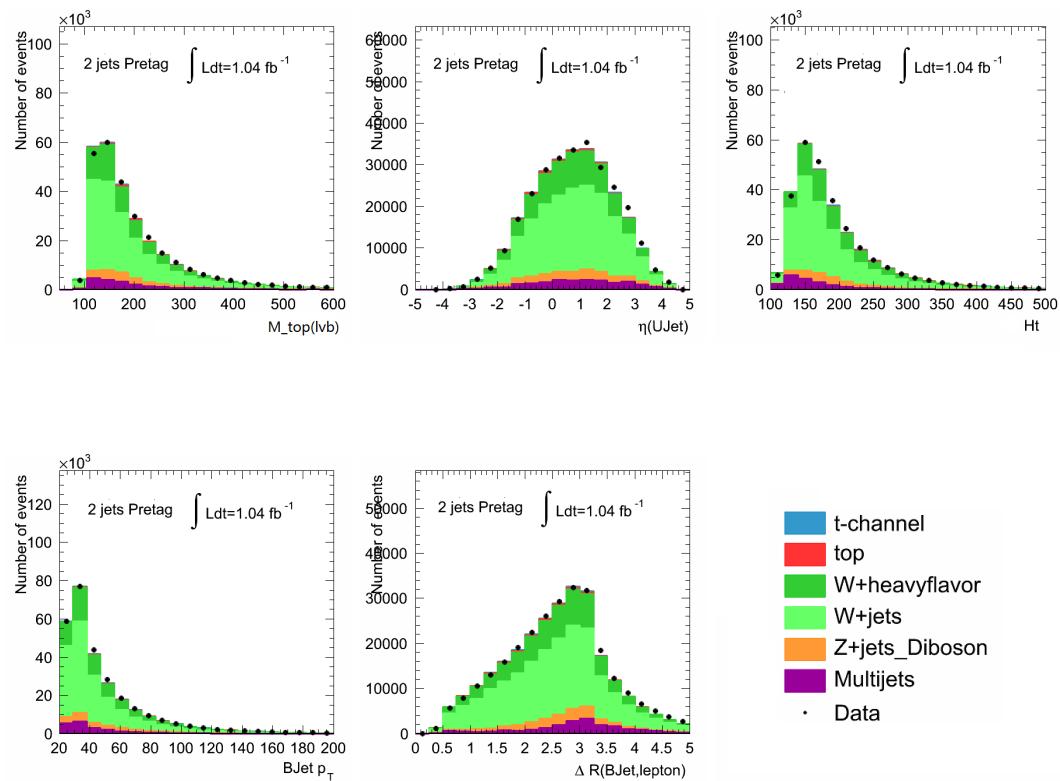
Figure 6.9: Most discriminant variables used as input of the BDT for the 2-jet pretag sample (electron and muon samples combined).
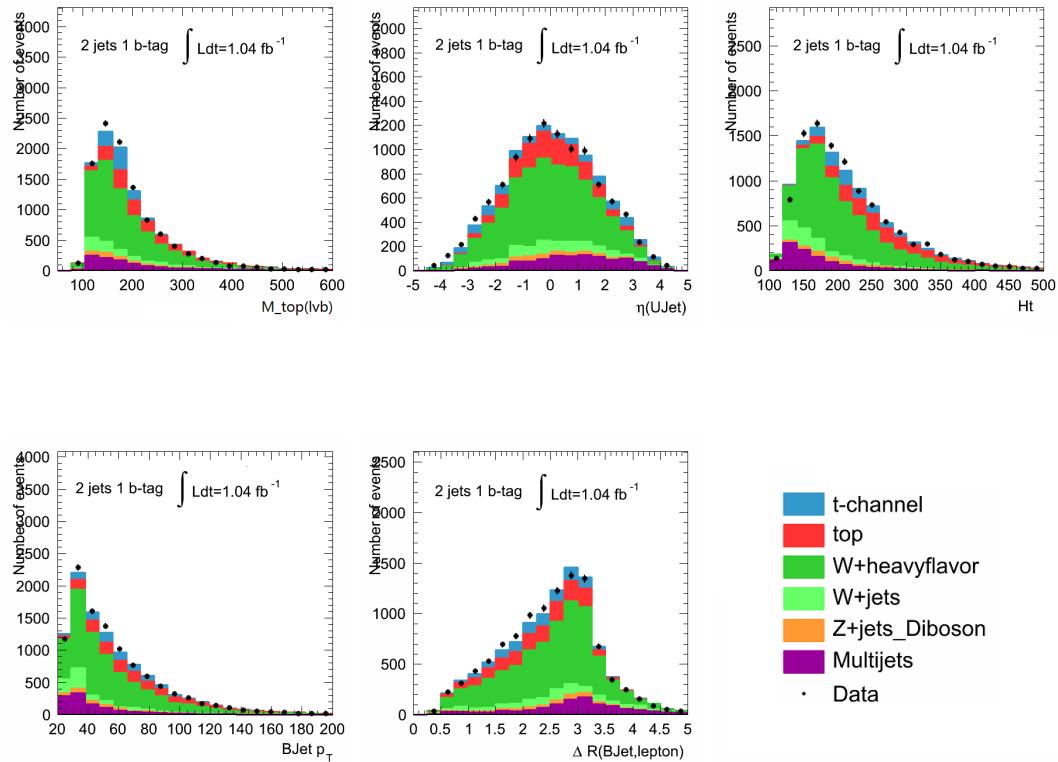
Figure 6.10: Most discriminant variables used as input of the BDT for the 2-jet b-tagged sample (electron and muon samples combined).
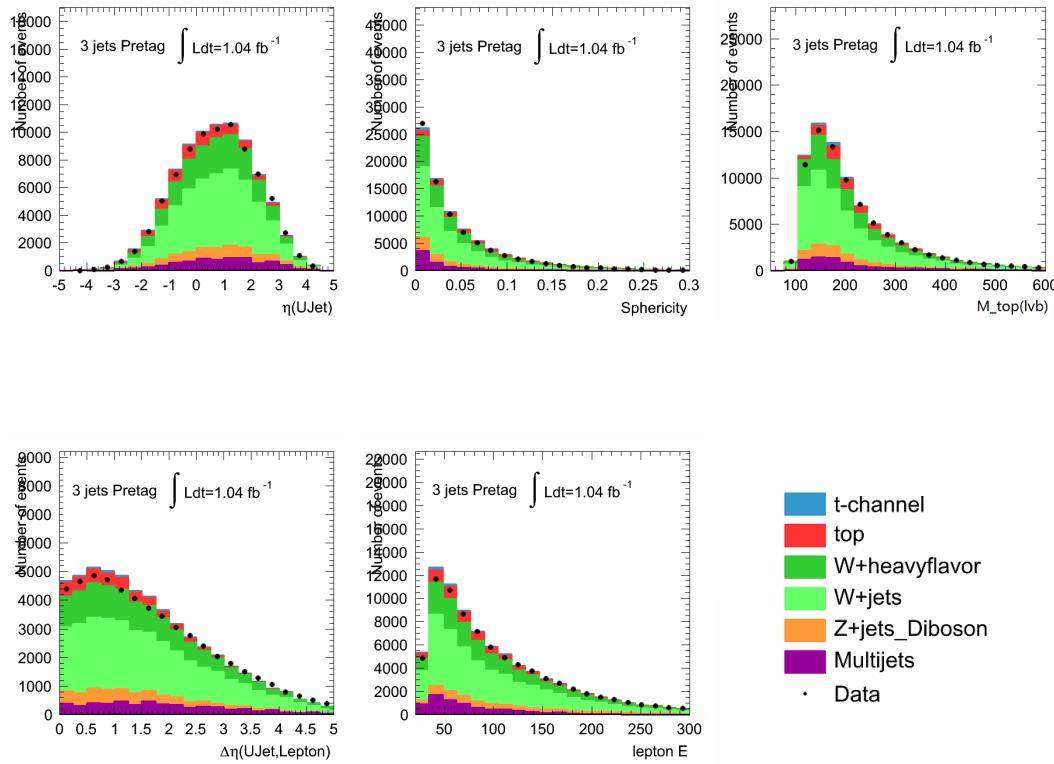
Figure 6.11: Most discriminant variables used as input of the BDT for the 3-jet pretag sample (electron and muon samples combined).
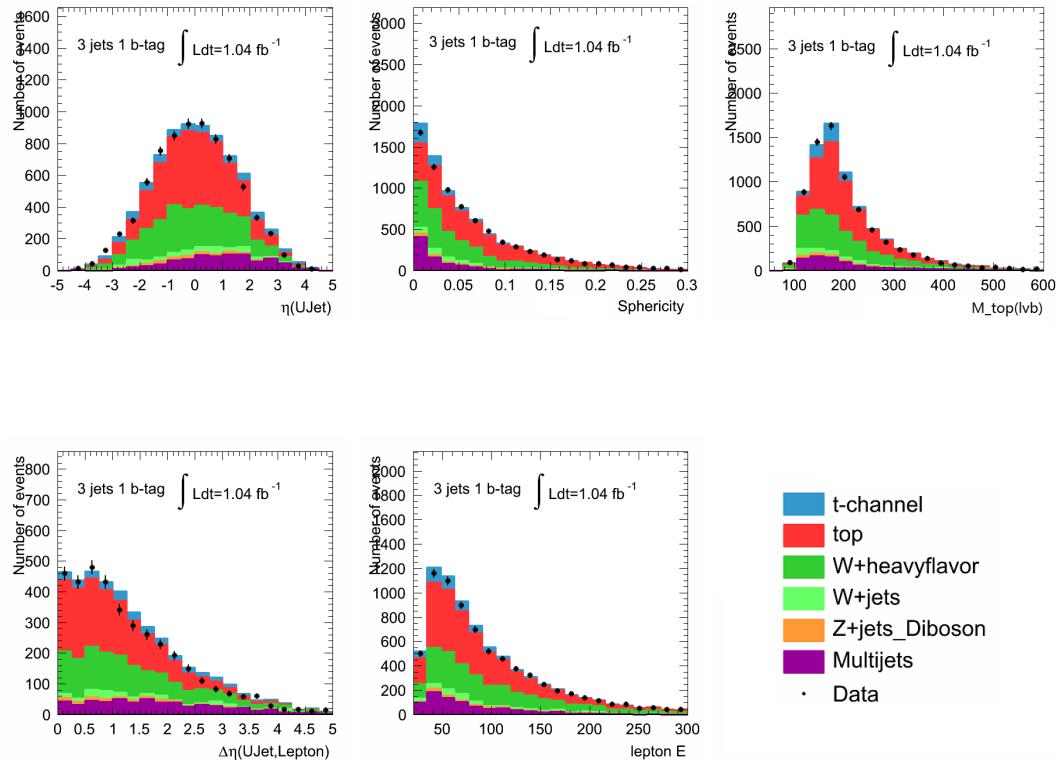
Figure 6.12: Most discriminant variables used as input of the BDT for the 3-jet b-tagged sample (electron and muon samples combined).
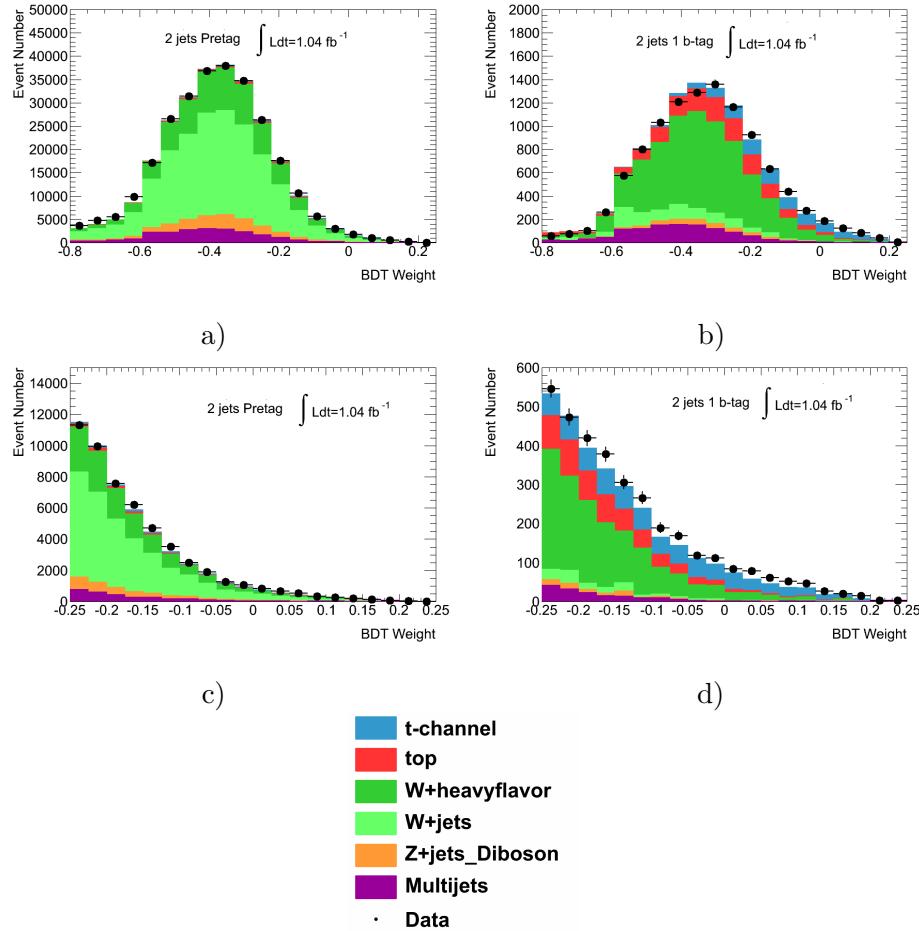
Figure 6.13: Boosted decision trees output for 2-jet events in a) pretag and b) b-tagged samples (electron and muon samples combined). Figures c) and d) show the upper tail of each distribution (BDT Weight> −0.25).
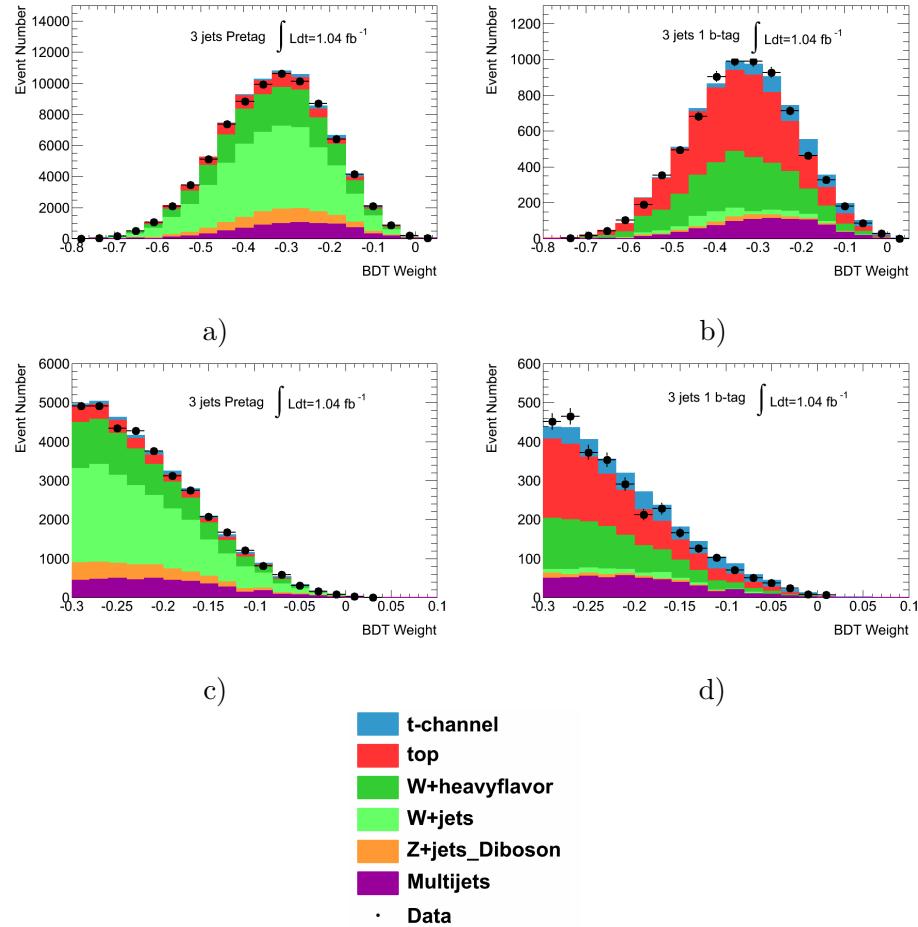
Figure 6.14: Boosted decision trees output for 3-jet events in a) pretag and b) b-tagged samples (electron and muon samples combined). Figures c) and d) show the upper tail of each distribution (BDT Weight> −0.30).

6.2.5 Pile-up Checks

Pile-up refers to the occurrence of multiple interactions in the same bunch crossing. The measured average number of interactions per bunch crossing $< \mu >$ in current data is shown in Section 3.4. Pile-up will affect the objects energy (jet, E_T^{miss}) measuring, the jet multiplicity in the event and the trigger rate. Unexpected pile-up condition could lead to mis-modeling of variables and loss of event selection efficiency. The LHC will have high levels of pile-up as luminosity increases. Thus it is important to study the impacts of high pile-up conditions on the analysis.

One observable directly associated with pile-up is the vertex multiplicity in a event. In BDT analysis, the BDT outputs of the dominate backgrounds and signal events are compared with the ones of hight pile-up events by requiring the number of primary vertices to be larger than six. Good agreement is observed as shown in Fig 6.15.
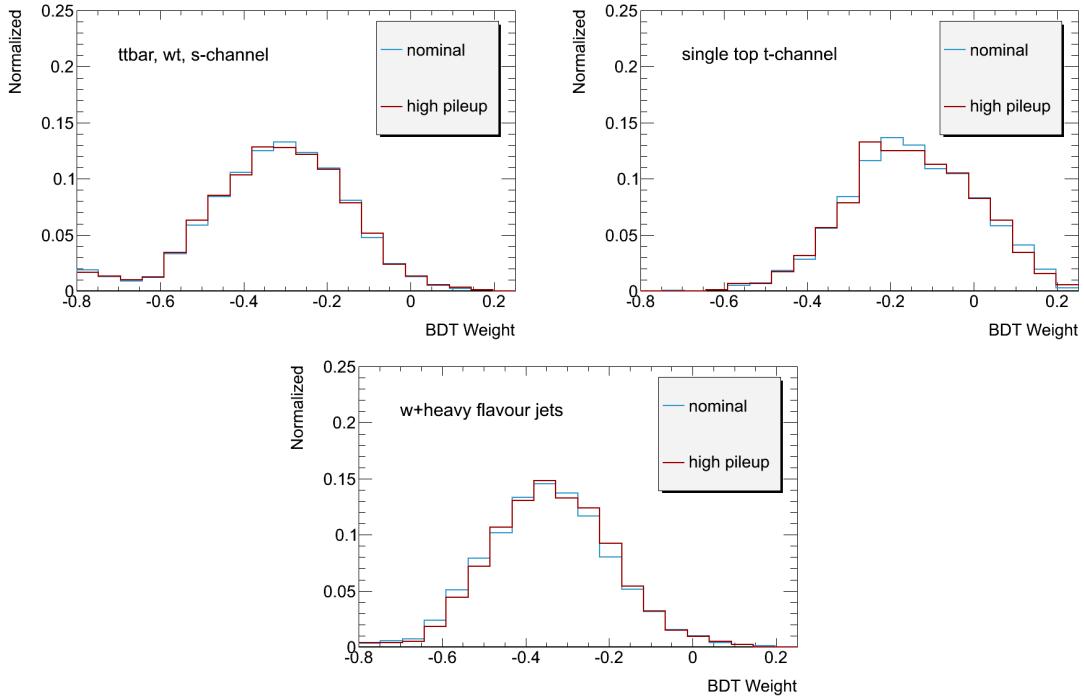

Figure 6.15: BDT outputs of hight pile-up events compare to the nominal ones, for the dominate backgrounds and signal events.

6.3 Event Yield after Selection on BDT outputs

To improve the signal purity, events are selected to have BDT output values above a certain threshold. These cuts are chosen, for both 2-jet and 3-jet channel BDT distribution, such as to minimize the total expected uncertainty on the cross-section determination.

For 2-jet channel, the BDT distribution of b-tagged samples are scanned over the range [-0.8,0.2] with a granularity of 20 bins and 21 cut values starting with -0.8 are chosen. The systematics sensitivities of different cut choice in the cross section measurement are estimated by performing pseudo experiments as introduced in Section 6.5. It is found that the best cut choice rests in the range [0,0.1]. Then a refined scan is done with a granularity of 0.01 in this range. The cut value that gives the minimum statistical and systematical uncertainties on the expected cross section measurement is found to be 0.02 for 2-jet channel cross section measurement. Similar procedure is performed for 3-jet channel measurement and the best BDT lower thresholds is chosen at -0.08.

Expected and observed event yields after the application of these additional cuts are show in table 6.5. "Other top" refers the single top-quark s-channel and Wt-channel events. Comparing to the event yields in Section 5.6, the ratio of signal events over background events (S/B) in the selected data has increased from less than 0.1 to 1.16 (combined), while the statistic of signal events remains relatively large. The major contributions of the backgrounds come from $t\bar{t}$ events and W+jets events.

	2-jet	3-jet	total
t-channel	139.1 ± 51.2	53.3 ± 17.6	192.4 ± 54.1
$t\bar{t}$, Other top	18.9 ± 7.4	35.1 ± 19.6	54.0 ± 21.0
W+light jets	2.3 ± 1.6	3.8 ± 3.9	6.1 ± 4.2
W+heavy flavour jets	61.8 ± 19.1	23.4 ± 8.2	85.2 ± 20.8
Z+jets, Diboson	1.6 ± 1.7	0.4 ± 0.6	2.0 ± 1.8
QCD	5.3 ± 3.4	12.9 ± 6.9	18.2 ± 7.7
TOTAL Expected	229.1 ± 55.3	128.9 ± 28.7	358.0 ± 62.3
S/B	1.55	0.71	1.16
DATA	320	126	446

Table 6.5: Event yield after the application of thresholds on the boosted decision trees discriminants outputs. The multijets and W+jets backgrounds are normalized to the data, all other samples are normalized to theory cross sections. Uncertainties shown are systematic uncertainties.

6.4   Cross Section Measurement with Likelihood Fit

After applying selections on the BDT output of data and MC samples, the expected numbers of single top-quark t-channel events and of all backgrounds are fitted to match the observed number of data [115]. The likelihood function used for the fit is given by the product of the Poisson likelihoods. The background rates are constrained by Gaussian priors.

$$L(\beta^s; \beta_j^b) = \frac{e^{-\mu} \cdot \mu^n}{n!} \cdot \prod_{j=1}^{B} G(\beta_j^b; 1.0, \Delta_j) \quad \text{with} \tag{6.11}$$

$$\mu = \mu^s + \sum_{j=1}^{B} \mu_j^b \ , \quad \mu^s = \beta^s \cdot n_s \ , \quad \text{and} \quad \mu_j^b = \beta_j^b \cdot n_j \ . \tag{6.12}$$

Here n_s is the predicted number of signal events in the selected data, while n_j is the predicted number of events of background j in the selected data set. n is the number of observed events in selected data. The index j runs over all background processes that are considered. The number of considered background processes is B. The scale factors β^s for signal and β_j^b for the backgrounds are the parameters of the likelihood function that are to be fitted to match the observed data. The background scale factors are constrained by Gaussian penalty terms to account for the *a-priori* knowledge on the backgrounds. The Gaussian functions of these priors have a mean of 1.0 and a width of Δ_j which is the relative uncertainty of the predicted background cross sections (See background cross section uncertainties in Section 6.5). The scale factors β^s and β_j^b are obtained by minimizing the negative log of the likelihood function $-logL(\beta^s; \beta_j^b)$.

With the observed number of single top-quark t-channel events in data, μ^s, the cross section of t-channel single top-quark production is given by,

$$\sigma_t = \frac{\mu^s}{\epsilon \mathcal{L}}, \tag{6.13}$$

where ϵ is the event selection acceptance of signal events and $\mathcal{L}$ is the integral luminosity of the data sample. ϵ is estimated using Monte Carlo simulated samples

$$\epsilon = \frac{n_s}{\sigma_t^{MC} \mathcal{L}}. \tag{6.14}$$

Combine Equation 6.13 and Equation 6.14, the cross section of single top-quark t-channel production can be obtained by

$$\sigma_t = \frac{\mu^s}{n_s}\sigma_t^{MC} = \beta^s \sigma_t^{MC}. \tag{6.15}$$

6.5   Systematic Uncertainties

The systematic uncertainties on the cross section measurement are determined using a frequentistic method based on pseudo experiments [115]. The uncertainties from various sources cause variations on the signal acceptance and the background rates, which are discussed in the second part of this section. These variations are propagated to the creation of the pseudo experiments. The entire set of pseudo experiments can thereby be interpreted as a replication of the sample space given our systematically limited knowledge of nature. An estimator denoting the probability density of all possible outcomes of the measurement is obtained from the cross section measurement using these pseudo experiments. The root mean square (RMS)^2 of this estimator distribution is an estimation of the uncertainty of the measurement. Performing the pseudo experiment based on the expected signal and background cross sections gives the expected uncertainty. Using the measured single top t-channel cross section and using the estimated nuisance parameters β_j on background cross section one can estimate the uncertainty of the actual measurement.

6.5.1   Creation of Pseudo Experiments

The pseudo experiments are created by varying the number of backgrounds events and signal events. For a background j, its expectation value $\tilde{\nu}_j$ is varied according its theoretical cross section uncertainty Δ_j and the uncertainties caused by all source of systematics. The signal expectation value $\tilde{\nu}_s$ is varied according the systematic uncertainties.

For the variation of $\tilde{\nu}_j$ due to cross section uncertainty Δ_j, it is done by throwing a random number β_j^{gen} according to a log-normal distribution with mean one and RMS Δ_j. The varied expectation value is then $\tilde{\nu}_j\beta_j^{\text{gen}}$. Using a log-normal distribution as prior has the advantage of avoiding unphysical negative values by construction.

For the variation of $\tilde{\nu}_j$ due to a systematic source i, it is technically done by throwing a Gaussian distributed random number δ_i using a mean of zero and a width of one. And the acceptance (event yields) positive shift ϵ_{ij+} and negative shift ϵ_{ij-} due to the i systematic

---

^{2}Physical scientists often use the term root-mean-square as a synonym for standard deviation when they refer to the square root of the mean squared deviation of a signal from a given baseline or fit.

source are also included in the variation.

Then in one generated pseudo experiment, the expectation value of background j is

$$\nu_j^{\text{gen}} = \tilde{\nu}_j \cdot \beta_j^{\text{gen}} \cdot \left\{ 1 + \sum_{i=1}^{S} |\delta_i| \cdot \left(\cdot H(\delta_i) \cdot \epsilon_{ij+} + H(-\delta_i) \cdot \epsilon_{ij+} \right) \right\} , \qquad (6.16)$$

where H denotes the Heaviside function. The number of the background events n_j in this pseudo experiment is based on a Poisson distribution with mean ν_j^{gen}. The expected number of signal events in the pseudo experiment is determined in similar way without taking into account the cross section uncertainties.

A large set of pseudo experiments are generated in this way to cover all possible variations due to all the systematics.

6.5.2 Sources of Systematic Uncertainties

The systematic uncertainties of the signal acceptance and the normalization of the individual backgrounds are from various sources. All these uncertainties finally cases variations on the event yields of signal and backgrounds and are then propagated in the creation of the pseudo experiments.

- **Lepton energy scale/resolution:** Lepton energy and lepton resolution in MC are corrected to data by applying scale factor and by smearing respectively (See Section 5.3). The impact of the lepton energy scale uncertainty on the selected sample is evaluated by scaling the p_T of the lepton up or down by 1σ and re-applying the object and event selections. The smearing of the lepton energy resolution is also shifted according to its uncertainties and selections are redone.

- **Lepton Identification (ID) and trigger efficiency scale factors:** The scale factors are applied to MC lepton trigger/ID efficiencies in order to reproduce the efficiencies seen in data. To assess their impact on the cross-section measurement, the scale factors that shifted according to their uncertainties are used to re-compute the predicted MC event yields and signal acceptance.

- **Jet energy scale:** In ATLAS, the measurement of the jets starts from signals recorded in the calorimeter cells (See Section 3.3.3). The jet energy measured at calorimeter level needs to be calibrated to the particle level, to correct calorimeter noncompensation, energy losses in dead material, shower leakage, "out of cone" energy, and pile-up. The jet energy scale (JES) is derived from these calibrations using data[125]. The energy of each jet are scaled up or down by 1σ, to estimated its uncertainties. The change is propagated to the missing transverse energy calculation, then the object and event selection are redone to measure the effect on the cross-section measurement. The pile-up uncertainty and b-tagged JES uncertainty are added in quadrature to the JES uncertainty.

- **Jet energy resolution:** The impact of the jet energy resolution is evaluated by smearing the jet energy in data [125].

- **Jet reconstruction efficiency:** The jet reconstruction efficiency impact is evaluated by randomly dropping jets from events according to its uncertainties. Event selections are re-applied to determine the variation from the nominal sample [125].

- **B-tagged heavy flavour and light flavour scale factor uncertainty:** The btagging efficiency and light jet mis-tag rate of btagging algorithms have been measured from data [13, 12]. Scale factors of data/MC are derived and corresponding uncertainties are evaluated. These uncertainties are propagated to the final event yields.

- **MC generator:** The dependence of signal acceptance on the MC generator used is determined by the difference between the standard AcerMC single top-quark events and single top-quark events generated by MCFM [126]. Systematic effects from Monte Carlo modeling for the $t\bar{t}$ process are estimated by comparing generators (MC@NLO + HERWIG vs POWHEG + HERWIG).

- **Parton shower modeling:** The dependence of the signal acceptance on the parton shower model is estimated by symmetrizing the difference between ACERMC + PYTHIA

and ACERMC + HERWIG using simulations of t-channel single top-quark processes. Systematic effects from Monte Carlo modeling for the $t\bar{t}$ process are estimated using Powheg + PYTHIA and Powheg + HERWIG.

- **Initial and final state radiation:** The dependence of the signal acceptance and the $t\bar{t}$ background uncertainty on the ISR/FSR model is estimated respectively from a set of single top-quark and $t\bar{t}$ ACERMC + PYTHIA samples generated with various ISR/FSR tunes which explore the full experimentally allowed parameter space. The largest deviations from the nominal samples coincide with the ISR and FSR combination shifted up or down, so this variation is used to determine the uncertainty. Correlations between different processes are also considered.

- **Parton distribution functions:** The signal and background MC samples are reweighted according to each of the PDF uncertainty eigenvectors and take the largest variation as the uncertainty.

- **Background cross section:** In this analysis, the event yields from the $t\bar{t}$, Z+jets and diboson background processes are estimated using the acceptance from MC and the theoretically predicted cross-sections. The cross section uncertainty on the $t\bar{t}$ cross section is $164.57^{+11.4}_{-15.7}$. An uncertainty of 5% is assigned to the diboson background and an uncertainty of 60% to the Z+jets background. For the Wt- and s-channel single top-quark processes, a 10% uncertainty is used on the cross-section.

- **QCD background normalization:** The QCD background is normalized to data through the fitting method in the electron channel and muon channel, as described in section 5.4. A systematic uncertainty of 50% is assigned.

- **W+jets background normalization and flavour composition:** Various systematic uncertainties on W+jets scale factors estimations as introduced in Section 5.5 are propagated to the final analysis. The W+jets flavour uncertainties are treated as fully correlated between Wbb and Wcc and uncorrelated with Wc+jets and with W+light jet processes.

- **Luminosity:** The luminosity uncertainty for 2011 data is 3.7%. This uncertainty is based on dedicated *van der Meer* scans taken in May 2011 with ongoing evaluation of this calibration using calorimeter-based techniques.

- **MC statistics:** The uncertainty due to the limited size of the Monte Carlo samples are included.

- **W+jets shape uncertainty:** A shape uncertainty to the W+jets background is assigned based on varying several parameters in the generation of the W+jets samples (ptjmin10, iqopt3). The W+jets samples are reweighted according to each of these parameters and take the largest variation as a systematic uncertainty.

- **Forward jet η reweighting:** To evaluate uncertainties due to the mis-modeled η distribution of the forward jet, especially for high η regions, alternative MC distributions are generated by reweighting. The reweighting histogram is obtained from the pretag data sample. The η distribution from observed events is divided by the distribution taken from MC simulation.

- **Missing Transverse Energy:** An "$E_{\mathrm{T}}^{\mathrm{miss}}$" uncertainty is included which accounts for uncertainties in the soft jets and cell-out terms. These are treated as fully correlated. The uncertainties in the $E_{\mathrm{T}}^{\mathrm{miss}}$ due to pile-up are also taken into account. The variation in the event yields due to each of these uncertainties is a few percent.

- **Liquid Argon Hole:** An uncertainty related to reconstruction issues due to the hole in the liquid argon calorimeter is included. The variation in the event yields due to this uncertainty is a few percent.

The uncertainties of main sources of systematics on the rates of all processes are given in Table 6.6 and 6.7 for 2-jet and 3-jet events, respectively. The impact that each systematic uncertainty on the expected and observed cross-section measurement is given in Table 6.9 in Section 6.6.

Uncertainties(%)		t	Other top	W+lightj	W+heavyj	Z+j, diboson
Jet energy scale	up	-4	-4	4	-10	-16
	down	2	11	-16	-22	-19
Jet energy resolution		< 1	±3	-	-	±14
Jet reconstruction		< 1	±1	±2	±2	±4
b tagging scale factor	up	10	7	11	11	17
	down	-11	-8	-10	-9	-16
Mistag scale factor		< 1	< 1	±18	±5	±6
Lepton scale factor		±4	±2	-	-	±4
Lepton energy resolution	up	-2	5	-	-	-12
	down	1	8	-	-	-10
MC Generator		±7	±13	-	-	-
Shower		±14	±11	-	-	-
ISR/FSR	up	-11	-28	-	-	-
	down	29	-16	-	-	-
PDF		±3	±8	-	-	-
Luminosity		±4	±4	-	-	±4
$E_{\mathrm{T}}^{\mathrm{miss}}$	up	-1	-1	-9	-1	-3
	down	1	1	-6	1	2
η reweighting		±4	±2	±2	±5	±8
Wc, cc, bb normalization		-	-	-	±6	-
Multijets		-	-	±3	±7	-
$t\bar{t}$ cross section		-	±6	±1	±4	-
Wt, s-channel cross section		-	±2	±2	±4	-
Z+jets cross section		-	-	±4	±2	±45
Diboson cross section		-	-	< 1	< 1	±1
MC Statistics		±4	±7	±55	±14	±48

Table 6.6: Rate uncertainties for the 2-jet channel.

Uncertainties(%)		t	Other top	W+lightj	W+heavyj	Z+j, diboson
Jet energy scale	up	25	-1	13	29	75
	down	-10	-12	53	7	-29
Jet energy resolution		1	< 1	-	-	±41
Jet reconstruction		4	< '	±11	±2	±37
b-tagging scale factor	up	7	7	9	7	11
	down	-8	-9	-11	-10	-13
Mistag scale factor		< 1	< 1	±25	±2	±5
Lepton scale factor		±2	< 1	-	-	±4
Lepton energy resolution	up	10	-1	-	-	67
	down	9	1	-	-	-89
MC Generator		±7	±13	-	-	-
Shower		±2	±21	-	-	-
ISR/FSR	up	7	-44	-	-	-
	down	12	-43	-	-	-
PDF		±3	±8	-	-	-
Luminosity		±4	±4	-	-	±4
η reweighting		±4	±4	±9	±3	±8
Wc, cc, bb normalization		-	-	-	±4	-
Multijets		-	-	±4	±8	-
$t\bar{t}$ cross section		-	±6	±1	±6	-
Wt, s-channel cross section		-	±1	±2	±3	-
Z+jets cross section		-	-	±6	±5	±45
Diboson cross section		-	-	< 1	±1	±1
MC Statistics		±5	±3	±81	±14	±44

Table 6.7: Rate uncertainties for the 3-jet channel.

6.6   Results of Cross Section Measurement

The β values obtained in the single top-quark t-channel cross section measurement using likelihood fit are given in Table 6.8. The observed (measured) cross-section is derived by multiplying the β value of the single top-quark t-channel process with its standard model cross-section. In the fit, the multijets and W+jets backgrounds estimated using data-driven methods are not allowed to vary, and other backgrounds are varied within their theoretical cross-section uncertainties. The 2-jet channel and 3-jet channel are fitted simultaneously to get the combined results.

Channels	t-channel	$t\bar{t}$, Other top	W+light	W+heavy	Z+jets, Diboson	Multijets
Combined	1.506551	0.962769	1.000000	1.000000	1.007525	1.000000
2-jet	1.653824	1.000000	1.000000	1.000000	1.000005	1.000000
3-jet	0.945393	0.999985	1.000000	1.000000	0.999997	1.000000

Table 6.8: The β values determined from fitting different processes for 2-jet channel and 3-jet channel and the combination of 2-jet and 3-jet channels.

The cross-section uncertainties are determined by generating pseudo experiments, 100,000 for each measurement using 2-jet, 3-jet and their combined samples. Each pseudo experiment gives a measured β of single top-quark t-channel cross section. By taking into account all systematics sources in the generation of pseudo experiments as introduced in Section 6.5, the measured factor β distribution reflects the probability density of all possible outcomes of the cross section measurement. Its RMS and $\sqrt{(1 - mean)^2 + RMS^2}$ give the estimated uncertainties on the cross section measurement. Figure 6.16 shows the β distribution of all pseudo experiments created for the observed cross section measurement, including all uncertainties and combining 2-jet and 3-jet channels. The mean is 1.063 and the RMS is 0.310, giving the uncertainties on the cross section measurement of +31.6% and -31.0%.

With the standard model cross-section of 64.6 pb, the measured (expected) cross section and uncertainty is $\sigma_t = 106.8^{+36.5}_{-36.2}$ ($64.6^{+24.2}_{-24.1}$) pb for the two jet channel BDT analysis.
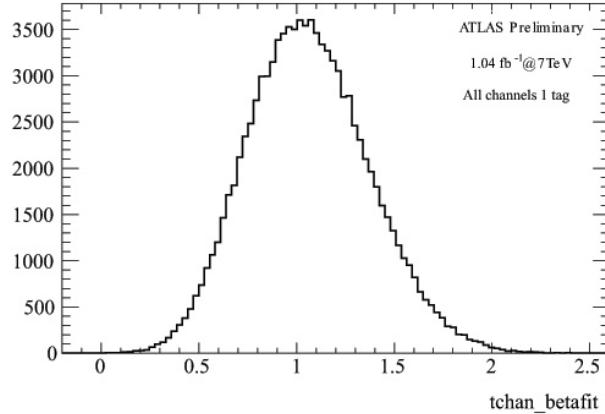
Figure 6.16: Pseudo-experiment distribution used for the final cross-section uncertainty determination. This distribution is for the observed cross-section uncertainty, for all channels combined.

For three jet channel BDT analysis, the measured(expected) cross-section is $\sigma_t = 61.1^{+32.6}_{-32.0}$ $(64.6^{+33.4}_{-32.6})$ pb.

Two jet and three jet are combined for the final cross section measurement. With the standard model cross-section of 64.6 pb, the measured (expected) cross section and uncertainty is $\sigma_t = 97.3^{+30.7}_{-30.2}$ $(64.6^{+22.0}_{-21.6})$ pb.

Table 6.9 shows a breakdown of the largest systematic uncertainties and their contribution to the final cross section measurements for expected data.

The impact of hight pile-up events to the cross-section measurement is also estimated. The events with larger number of primary vertices (> 6) are used to redo the whole analysis. As a results, a relative 5.7% shifts on the fitted observed cross-section is observed, with about 4% larger systematic uncertainties. As a conclusion, the t-channel single top-quark cross section measurement using boosted decision trees is not strongly affected by high pile-up condition.

Source	$\Delta\sigma_{\mathrm{exp}}/\sigma_{\mathrm{exp}}$ [%]	$\Delta\sigma_{\mathrm{obs}}/\sigma_{\mathrm{obs}}$ [%]
Data statistics	±9.7	±7.4
MC statistics	±7.2	±5.6
b-tagging scale factor	+16.7/-16.7	+14.6/-14.6
Mistag scale factor	+1.5/-1.5	+1.1/-1.1
Lepton scale factor	+4.9/-4.9	+4.7/-4.9
Lepton energy resolution	+2.7/-2.0	+1.7/-1.5
Jet energy scale	+8.8/-9.3	+6.3/-6.9
Jet energy resolution	+1.1/-1.1	+1.0/-1.0
Jet reconstruction	+1.9/-1.9	+1.3/-1.3
W shape	+0.3/-0.3	+0.5/-0.5
Wlj normalization	+0.3/-0.3	+0.7/-0.7
Wc, cc, bb normalization	+2.4/-2.4	+1.6/-1.6
η reweighting	+8.5/-8.5	+7.4/-7.4
$E_{\mathrm{T}}^{\mathrm{miss}}$	+0.1/-0.2	+0.4/-0.4
pile-up $E_{\mathrm{T}}^{\mathrm{miss}}$	+1.4/-1.4	+1.1/-1.1
LAr	+0.5/-0.6	+0.2/-0.3
PDF	+4.2/-4.2	+3.7/-3.7
Generator	+8,0/-8.0	+7.3/-7.3
Shower	+15.8/-15.8	+15.4/-15.4
ISR/FSR	+16.1/-16.1	+18.0/-17.6
Theory cross-section	+5.9/-5.9	+3.4/-3.4
Multijets	+3.6/-3.6	+2.2/-2.2
Luminosity	+4.6/-4.6	+4.2/-4.2
All Systematics	+32.6/-32.0	+30.8/-30.1
Total	+34.0/-33.5	+31.6/-31.0

Table 6.9: Breakdown of the major contributions to the systematic uncertainty on the expected t-channel single top-quark production cross-section measurement in the BDT analysis, expected and observed results for 2-jet and 3-jet channel combined.

6.7 $|V_{tb}|$ Measurement

In the Standard Model the CKM matrix element $|V_{tb}|$ is close to one, but new physics contributions could alter its value significantly. $|V_{tb}|$ can be directly determined from the measured single top-quark t-channel cross section since the cross section is proportional to $|V_{tb}|^2$. This $|V_{tb}|$ measurement makes no assumptions on the number of quark generations or on the unitarity of the CKM matrix. $|V_{tb}|$ is only assumed to be $|V_{tb}| \gg |V_{td}|, |V_{ts}|$ and W-t-b interaction is assumed to be a SM-like left-handed weak coupling.

$|V_{tb}|^2$ is calculated by dividing the observed single top-quark t-channel cross section with the SM expectation,

$$|V_{tb}|^2 = \frac{\sigma_t^{\text{measured}}}{\sigma_t^{MC}} = \beta_t. \tag{6.17}$$

β_t is the β value of single top-quark t-channel as discussed in Section 6.6. The result obtained is

$$|V_{tb}| = 1.23^{+0.20}_{-0.19}. \tag{6.18}$$

The experimental and theoretical uncertainties are added in quadrature.

The $|V_{tb}|^2$ measurement is modeled by a Gaussian likelihood. Restricting the range of $|V_{tb}|$ to the interval [0, 1], as required by the SM, the Gaussian likelihood is converted to have a integral of 1 in the range of [0, 1]. In a Bayesian view this corresponds to a flat prior between 0 and 1. The posterior probability density function of $|V_{tb}|^2$ measurement is shown in Figure 6.17. Integrating the posterior probability density function from 1 down to 0 until reaching 95% of the area, a lower limit on $|V_{tb}|$ at the 95% confidence level is obtained: $|V_{tb}| > 0.61$.

In the $|V_{tb}|$ measurement, the estimations of single top-quark s-channel, Wt-channel and the $t\bar{t}$ backgrounds are from theoretical prediction, where the $|V_{tb}|$ is assumed to be close to 1. Ignoring this assumption and giving $|V_{tb}|$ a value sizably different than 1.0 will not change the results of $|V_{tb}|$ measurement. Because the rate of $t\bar{t}$ background would not change since $|V_{tb}| \gg |V_{td}|, |V_{ts}|$ is assumed and other decays (to heavier 4th generation quarks) are prohibited by kinematics. In addition, the rate of background "$t\bar{t}$, other top is allowed to float within their cross section uncertainties during the measurement(See Section 6.4). The
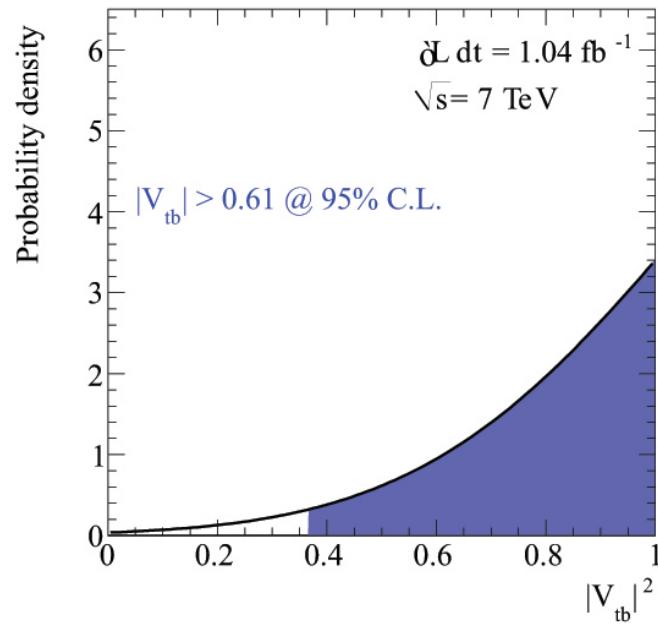
Figure 6.17: The posterior probability density function of $|V_{tb}|^2$.

variations caused by a different $|V_{tb}|$ is less than this uncertainties and thus negligible. In summary, the extraction of $|V_{tb}|$ is reliable under the assumptions in the measurement.

6.8 Conclusion

In this chapter, a multivariate discriminant is constructed by boosted decision trees to further extract single top-quark t-channel events from the data sets after pre-selection. The structures of boosted decision tress are easy to understand, which allows a transparent control of the method. The optimization of the training procedure is crucial to obtain a powerful and reliable BDT discriminator. All used variables are validated and are proved to be well-modeled. The selection using the constructed BDT discriminator significantly improves the signal purity in selected data with respect to the pre-selection.

After the BDT selection, the cross section of single top-quark t-channel production is measured by performing a likelihood fit of the expected number of signal and backgrounds to the observed data. The scale factors of signal and backgrounds are derived from the fit. The uncertainties of the cross section measurement are estimated by pseudo experiments, which are created according to the variations of the events yields due to different systematic sources. With the measured single top-quark t-channel cross section, the value of $|V_{tb}|$ and a lower limit are also extracted.

The uncertainties on the cross section measurement are dominated by systematic uncertainties. The largest systematic uncertainties are the modeling of ISR/FSR and the parton shower. Uncertainties from different generator choices and the modeling of η are also sizable. Another large uncertainty is the btagging scale factor uncertainty, which causes large variations on the acceptances of signal and backgrounds. JES uncertainty also constitutes one major systematic uncertainty on the cross section measurement. With more inputs from the experimental data available in the future, these systematic uncertainties are expected to be decreased.

In addition, the potential of the boosted decision trees can be further exploited to improve the measurements. Some solutions are discussed below:

- The choice on the BDT settings can be more aggressive. The optimization of BDT is a balance between overtraining, MC/data agreements and systematic uncertainties. Smaller systematic uncertainties could be achieved with the tolerance of larger overtraining or worse MC/data agreements.

- Alternative methods in BDT training can be used, such as using a different splitting criterion, different pruning method and different boosting method. Some simple tests have been performed and no significant improvements are shown. A detailed study is necessary.

- More subtle controls of the decision tree are possible, such as the normalization of the signal sample and background sample in the root node (normalized to equal size as default), definition of the signal/background node (default purity criterion is $\frac{1}{2}$), the β setting in AdaBoost method (default is 1).

- Fitting the full shape of BDT distributions to data instead of applying a selection will make maximal use of all signal events remaining after the pre-selection. It also allows for constraining the background rates from data. Preliminary study with the fit method have been performed, using the same trained BDT as presented in Section 6.2.3. It is found a reduction of 3% in total uncertainty of single top-quark t-channel cross section measurement. More improvements are expected with the utilization of a new BDT optimized for the fit method.

Chapter 7

SUMMARY AND OUTLOOK

This chapters gives a summary of the measurement results in this thesis. Some preliminary results on single top-quark t-channel cross section measurement from ATLAS and CMS experiment at the LHC are presented in the second section. The results are compared between different analyses and between different experiments. Possible single top-quark measurements and new physic searches in the future are discussed in the final part of this chapter.

142

7.1 Summary

The LHC has run smoothly and efficiently at center-of-mass $\sqrt{s} = 7$ TeV with an instantaneous luminosity larger than $10^{33} cm^{-2} s^{-1}$ in 2011. The integrated luminosity of 1.04 fb^{-1} data collected from ATLAS detector is used in this thesis to perform a single top-quark t-channel production cross section measurement. This measurement explored a boosted decision trees multivariate approach and combined the results of 2-jets and 3-jets channels. The measured cross section of single top-quark t-channel production is

$$\sigma_t = 97.3^{+30.7}_{-30.2} pb. \tag{7.1}$$

This results is compatible with the Standard Model prediction and stable with the high pile-up condition.

A measurement of the CKM matrix element $|V_{tb}|$ is also performed using the observed single top-quark t-channel cross section. This measurement is independent of assumptions about the number of quark generations or about the unitarity of the CKM matrix. Assuming $|V_{tb}| \gg |V_{ts}|, |V_{td}|$ and a SM-like left-handed Wtb coupling, the measured $|V_{tb}|$ is

$$|V_{tb}| = 1.23^{+0.20}_{-0.19}. \tag{7.2}$$

Constraining $|V_{tb}|$ to the Standard Model region $|V_{tb}| \leq 1$, a lower limit at 95% confidence level is obtained

$$|V_{tb}| > 0.61. \tag{7.3}$$

The measured $|V_{tb}|$ is compatible with the Standard Model prediction.

7.2 Preliminary Results from ATLAS and CMS

Cut-based (CB) analysis [116] and neural network (NN) analysis [115] in ATLAS use the same data sets and share the same pre-selection as boosted decision tree analysis. After pre-selection, CB analysis applies additional sequential selections to extract signal events, while the NN analysis exploits neural network multivariate discriminators.

7.2.1 Cut-based Analysis in ATLAS

The additional selection cuts in CB analysis were chosen in order to increase the expected significance of the t-channel single top-quark signal, taking into account systematic uncertainties on the background estimate [127]. These selection cuts are:

- 2-jet channel: $\eta(UJet) > 2.0$, $H_t > 210$ GeV, 150 GeV $< M\_top(l\nu b) < 190$ GeV, $\Delta\eta\_UJetBJet > 1$

- 3-jet channel: $\eta(UJet) > 2.0$, $H_t > 210$ GeV, 150 GeV $< M\_top(l\nu b) < 190$ GeV, $M\_AllJets > 450 GeV$.

Corresponding explanations for the variables used can be found in Section 6.2.1.

The cut-based analysis measures, by combining four different channels (positive and negative lepton charge, with two and three jets) a cross section of $\sigma_t = 92^{+29}_{-26}$ pb. The separation of candidate events according to the lepton charge allows individual measurements of the top-quark and top-antiquark cross sections, yielding the results $\sigma(t) = 59^{+18}_{-16}$ pb and $\sigma(\bar{t}) = 33^{+13}_{-12}$ pb, that can be compared to the theoretically predicted cross sections of $41.9^{+1.8}_{-0.8}$ pb and $22.7^{+0.9}_{-1.0}$ pb, respectively [20].

The data selected by CB selections and by BDT selections only partially (25%) overlapped. This allows examination of the signal in a different phase space region. The measured cross section in CB analysis is in good agreement with the one measured in BDT analysis.

7.2.2 Neural Network Analysis in ATLAS

NN analysis uses the NeuroBayes [128, 129] tool, which combines a three-layer feed-forward neural network with a complex preprocessing of the input variables. The variables used in NN are chosen according their separation performance in NN, which are not exactly the same with the ones used in BDT. Among 12 variables used in 2-jet channel in NN analysis, several most discriminating variables are $M\_top(l\nu b)$, $\eta(UJet)$, $E_T(UJet)$, $\Delta\eta(W, Bjet)$, $\Delta\eta(Bjet, Ujet)$, H_T, $M_T(W)$. 18 variables used in 3-jet channel, the most discriminating variables are $M(Jet1, Jet2)$, $M\_top(l\nu b)$ and $\Delta\eta(Jet1, Jet3)$.

In NN analysis, the signal event in selected data are extracted by performing a maximum likelihood fit to the entire NN output distributions in the 2-jet and 3-jet data set. Combining 2-jet and 3-jet channel, the measured cross section is

$$\sigma_t = 83 \pm 4 \,(\text{stat.}) \,^{+20}_{-19} \,(\text{syst.}) \text{ pb} = 83 \pm 20 \text{ pb.}$$

The value of $|V_{tb}|$ is extracted from the NN analysis. The result obtained is $|V_{tb}| = 1.13^{+0.14}_{-0.13} \,(\text{exp.}) \pm 0.02 \,(\text{theo.}) = 1.13^{+0.14}_{-0.13}$. Restricting the range of $|V_{tb}|$ to the interval $[0, 1]$, as required by the SM, a lower limit on $|V_{tb}|$ is extracted: $|V_{tb}| > 0.75$ at the 95% confidence level.

The measured cross section and $|V_{tb}|$ are in good agreements with BDT analysis. The estimated uncertainties is smaller than BDT analysis. A summary of the measured cross section results in BDT, CB and NN analysis in ATLAS are shown in Figure 7.1.

7.2.3 Results from CMS Experiment

The single top-quark t-channel cross section measurement in CMS uses $1.14 fb^{-1}$ data collected by CMS detector in 2011 [21]. CMS analysis applies event selections similar as the ATLAS analysis. These event selections are

- exactly one isolated muon (electron) candidate, with $p_T > 20$ GeV ($E_T > 30$ GeV) and $|\eta| < 2.1$ ($|\eta| < 2.5$).

- reject the events with additional muons (electrons) that pass the looser quality criteria, and $p_T > 10$ GeV (15 GeV), $|\eta| < 2.5$.
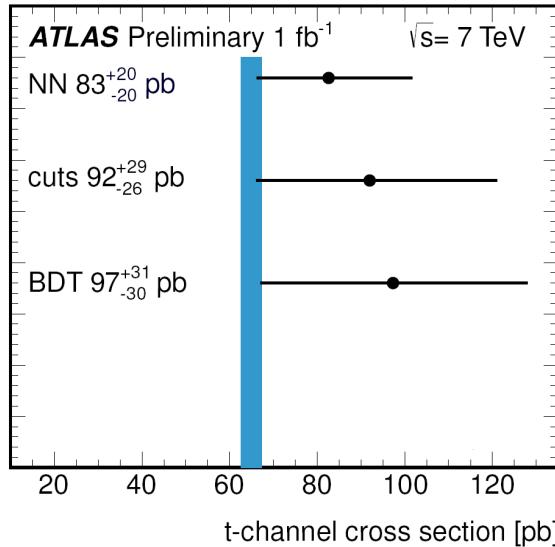
Figure 7.1: Summary of the ATLAS single top-quark t-channel cross-section results [19]. Theoretical predictions obtained from approximate NNLO calculation [20] are shown by the vertical bands.

- 2 or 3 jets with $p_T > 30$ GeV and $|\eta| < 4.5$.

- require $M_T(W) > 40$ GeV for muon channel to suppress the events with a muon does not come from a leptonically decaying W boson.

- require $E_T^{\text{miss}} > 35$ GeV for electron channel to reduce the QCD-multijet contamination.

The QCD-multijet background and W+jets background are also estimated using data-driven methods in CMS analysis. The signal content of the selected sample are extracted by performing a maximum likelihood fit to the distribution of the pseudorapidity of the light jet $\eta(UJet)$. The measured cross section with the muon and electron channel combined is

$$\sigma_t = 70.2 \pm 5.2(\text{stat.}) \pm 10.4(\text{syst.}) \pm 3.4(\text{lumi.})pb. \tag{7.4}$$

Assuming $|V_{tb}| \gg |V_{td}|, |V_{ts}|$, $|V_{tb}|$ is determined in CMS analysis,

$$|V_{tb}| = 1.04 \pm 0.09(\text{exp.}) \pm 0.02(\text{theo.}). \tag{7.5}$$

The results on single top-quark cross section measurement at the Tevatron have been introduced in Section 2.3.3. A comparison of the cross section measurements in CMS at the LHC and in D0 at the Tevatron is shown in Figure 7.2.
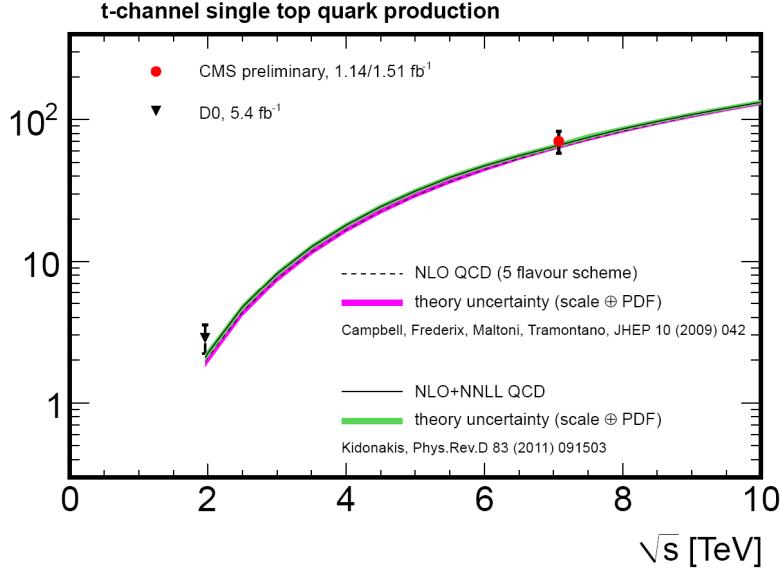
Figure 7.2: Single top cross section in the t-channel versus center-of-mass energy, comparing CMS measurement [21] with the dedicated t-channel cross section measurements in D0 experiment at the Tevatron [22, 23]. The results are also compared with the QCD expectations computed at NLO with MCFM in the 5-flavour scheme [24] and at approximate NNLO [20].

7.3 Single Top-quark Measurements in The Future

The studies on single top-quark have just begun. In the future, a large variety of single top-quark analyses are expected, including both SM measurements and searches for the possible new physics. All these studies could expand our knowledge of the particle physics and make us one step closer to the true nature of the universe.

7.3.1 Single Top-quark Wt-channel and s-channel Measurements

The cross section of single top-quark Wt channel production at the Tevatron is negligibly small. The first observation of the Wt associate single top production rests on the measurements at the LHC. In ATLAS, a search of the single top-quark Wt-channel production in dilepton final states is performed, observing a 3.3σ evidence [130]. In CMS, the single top-quark Wt associate production in dilepton channel is also measured, giving a significance of 2.7σ [131].

The studies on single top-quark s-channel and Wt-channel in lepton+jets final states have also started and results are expected in near future.

7.3.2 Flavor Changing Neutral Current (FCNC) Analysis

In the SM, FCNC processes are suppressed at higher orders, while extensions of the SM with new sources of flavour predict higher rates of FCNC top-quark productions [132]. A search of the FCNC single top-quark production is performed [133] in ATLAS. No evidence of FCNC production is found. Further constrains on the cross section of single top-quark FCNC production can be achieved in future analysis.

7.3.3 Top Polarization and W Polarization

In the Standard Model, the W boson couples only to fermions with left-handed chirality. As a results, the top quark produced in single top-quark t-channel and s-channel is 100% polarized along the direction of the d ($\bar{d}$) quark. The polarized top-quark decays into a W boson either left-handed or longitudinally polarized. The kinematics of the final state

particles in single top-quark production can be used to probe the polarization of top quark and W boson.

7.3.4 W' Measurement

Many new physic models such as techni-color [134], Kaluza-Klein extra dimensions [135], little Higgs models [136], have a common feature of existence of W'-like bosons. W' boson can contribute to the single top-quark s-channel production $q\bar{q}' \to W', W' \to t\bar{b}$. The distribution of the invariant mass of the $t\bar{b}$ system could shown a resonance effect around $M_{W'}$, which can be used to identify this type of new physics.

7.3.5   Search for Fourth Generation Quarks

The fourth generation bottom-like quark b' is possible in many physics scenarios. If $m_{b'} > m_t + m_W$, the b' is likely to decay into a top quark and a W^-. Thus the single b' production results in the same final states as single top-quark Wt-channel production. The studies on the single top-quark Wt-channel final states could search for the single b' production and constrain the mass of b'.

7.3.6   Many Other Measurements

Many other studies on the single top-quark production are very interesting but will not be discussed in detail here, such as the new final state of single top-quark production mono-tops [137], model-independent extraction of CKM matrix elements [138], anomalous tbW couplings in single-top production [139], searching for heavy resonance particles [140] and charged Higgs [141].

Appendix A

MODELING OF INPUT VARIABLES TO THE BOOSTED DECISION TREE
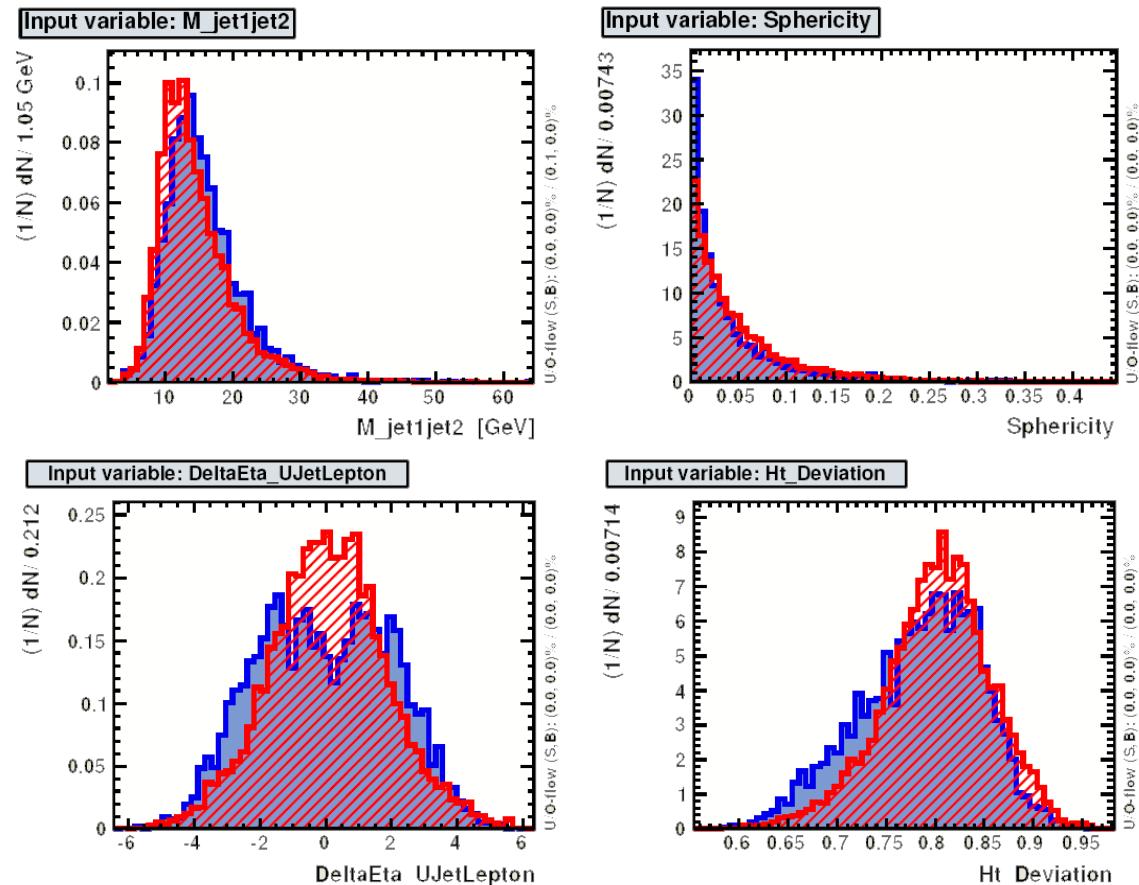
Figure A.1: Normalized distribution of the discriminating variables used as input of the boosted decision tree for signal (blue) and background (red) for 2-jets events.
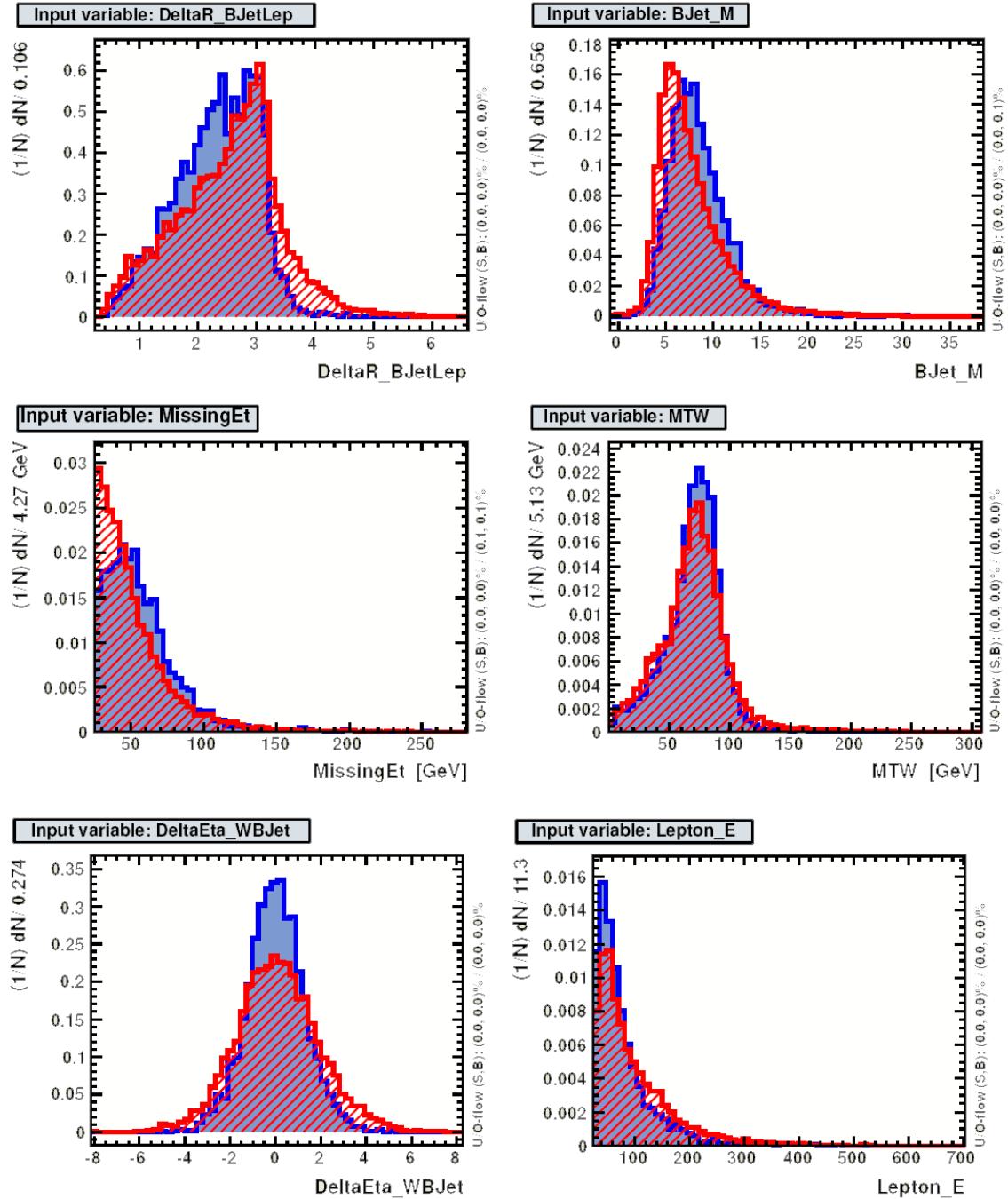
Figure A.2: Normalized distribution of the discriminating variables used as input of the boosted decision tree for signal (blue) and background (red) for 2-jets events.
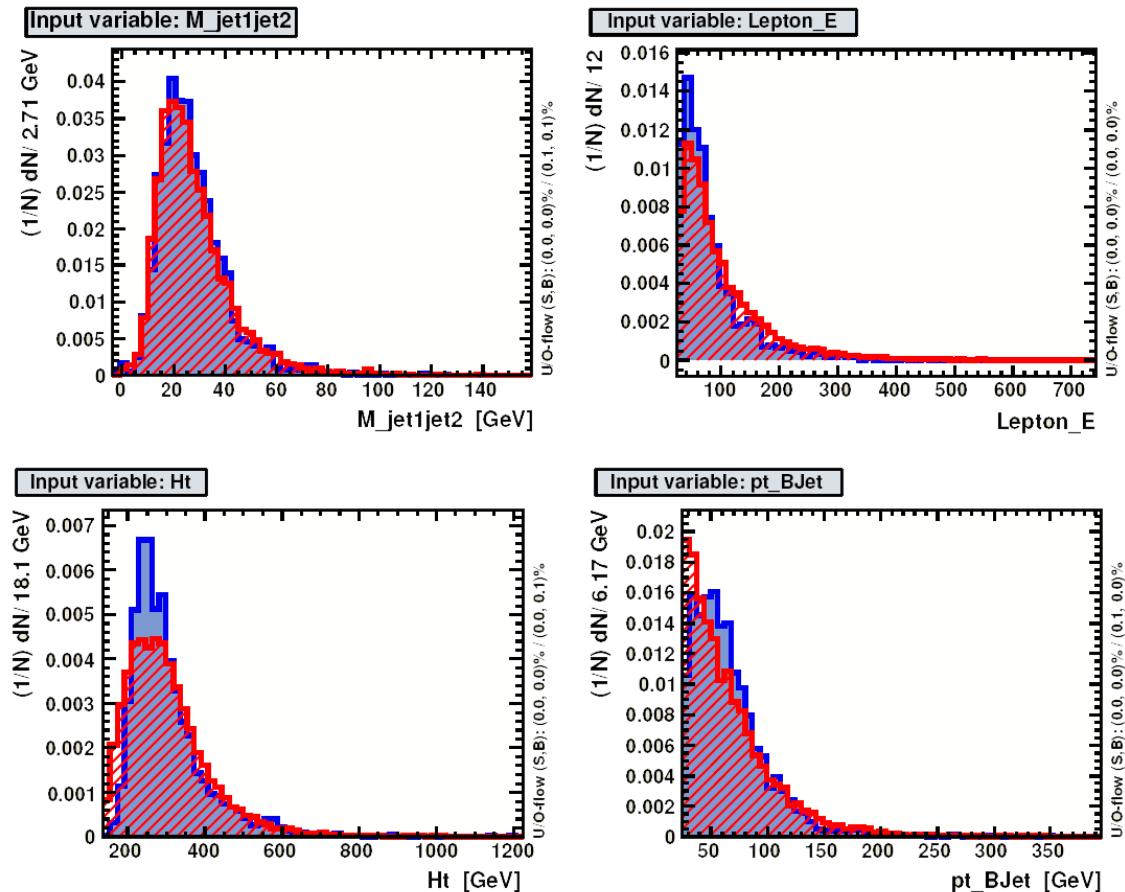
Figure A.3: Normalized distribution of the discriminating variables used as input of the boosted decision tree for signal (blue) and background (red) for 3-jets events.
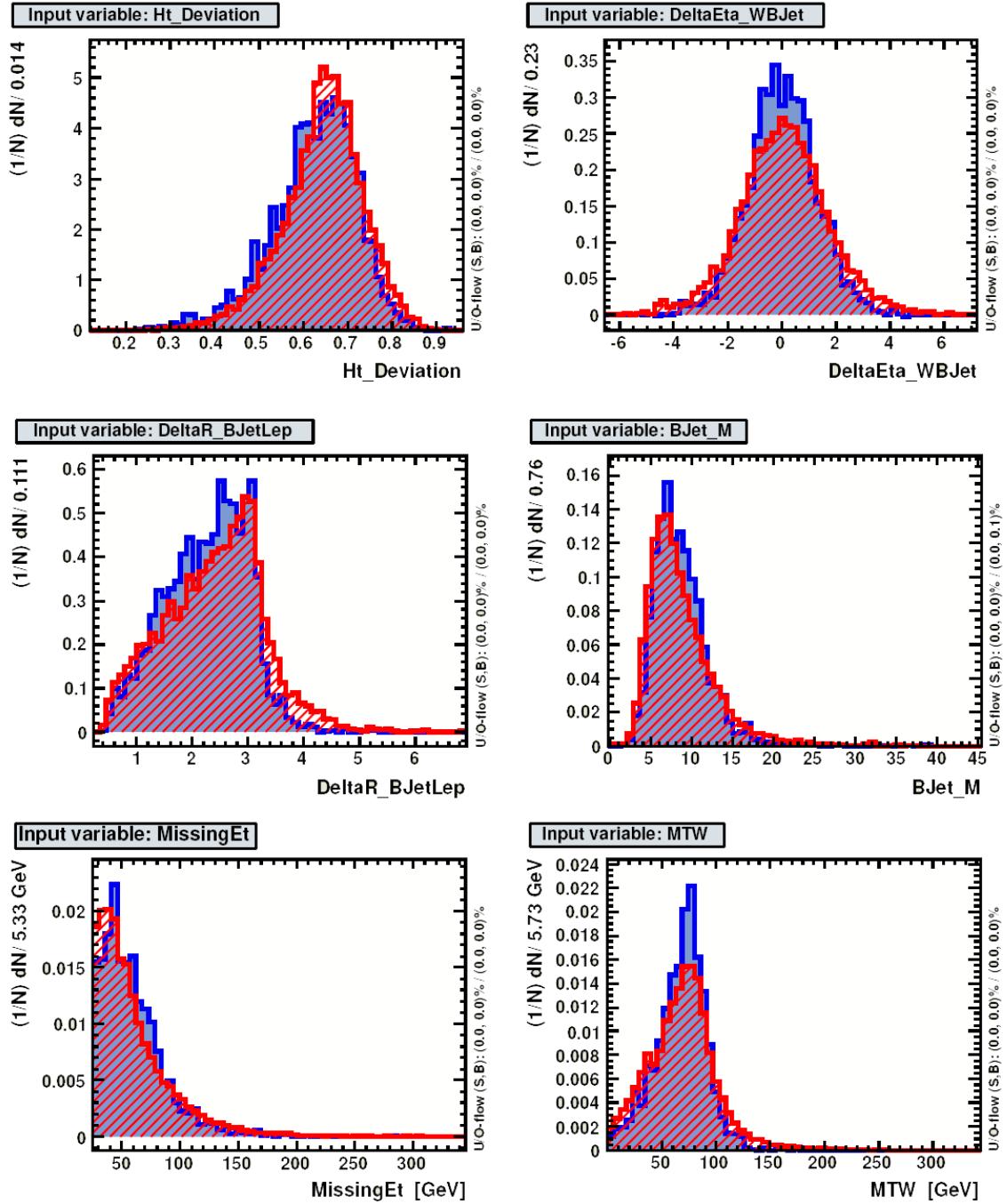
Figure A.4: Normalized distribution of the discriminating variables used as input of the boosted decision tree for signal (blue) and background (red) for 3-jets events.

154
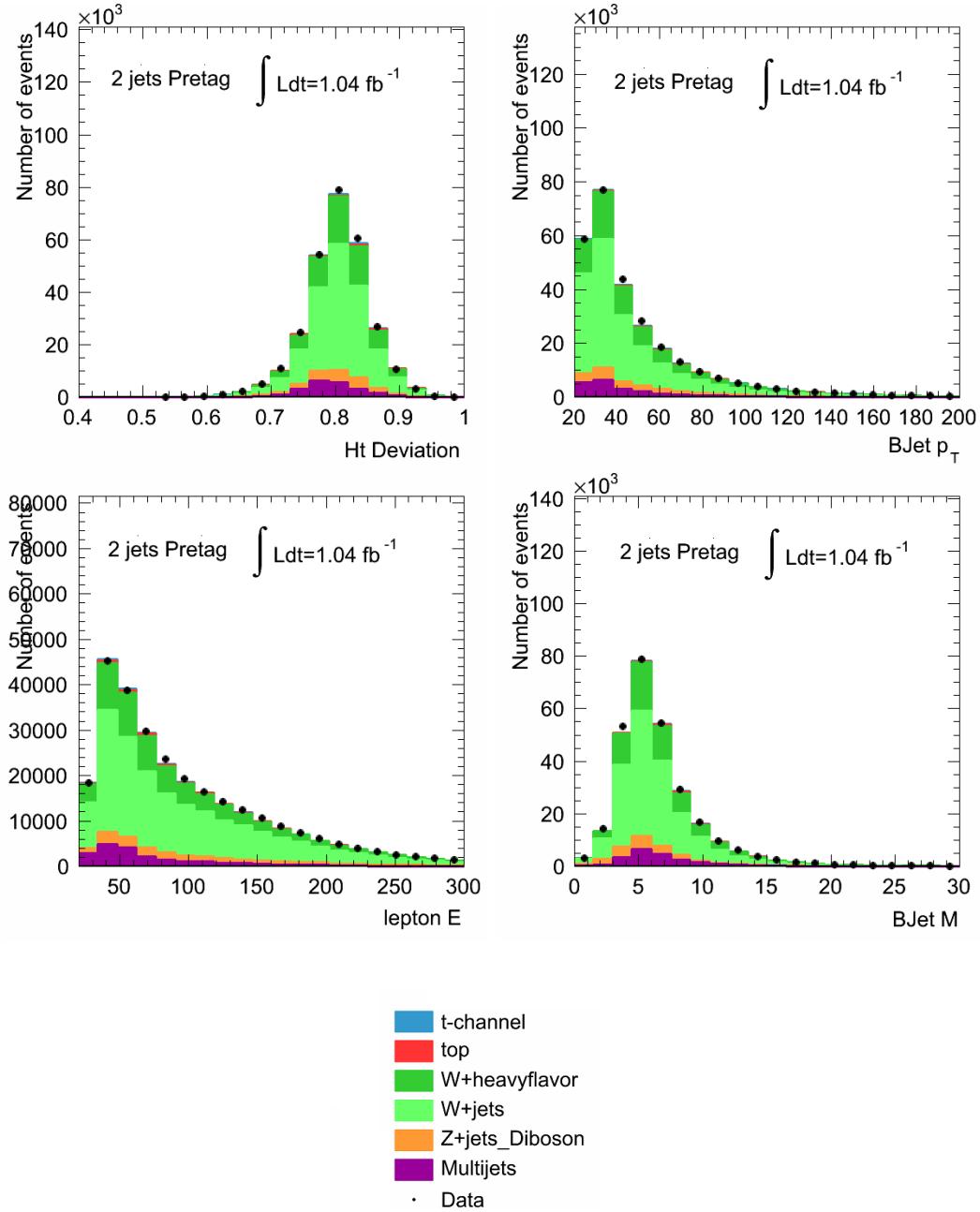
Figure A.5: Stacked distributions of the variables used as input of the BDT for the 2-jets pretag sample.
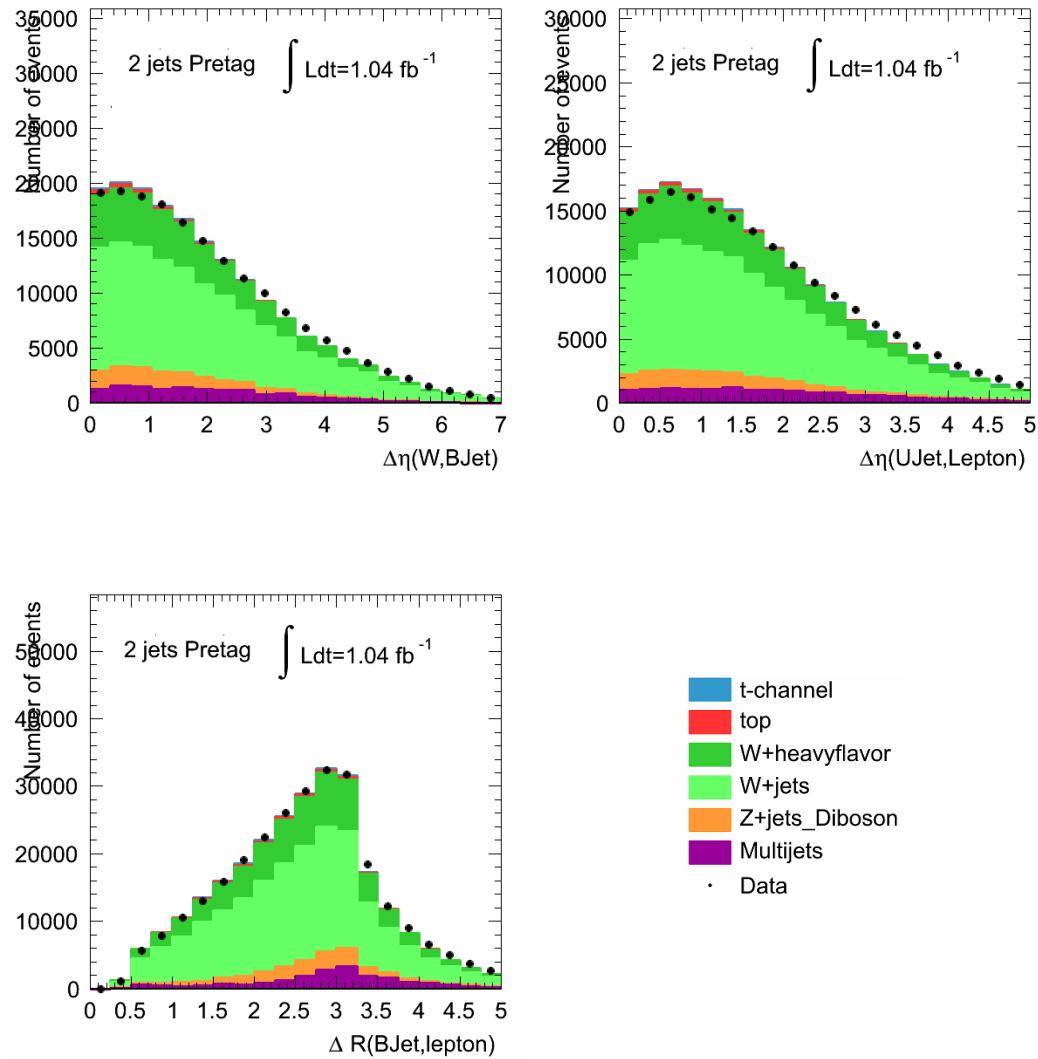
Figure A.6: Stacked distributions of the variables used as input of the BDT for the 2-jets pretag sample.
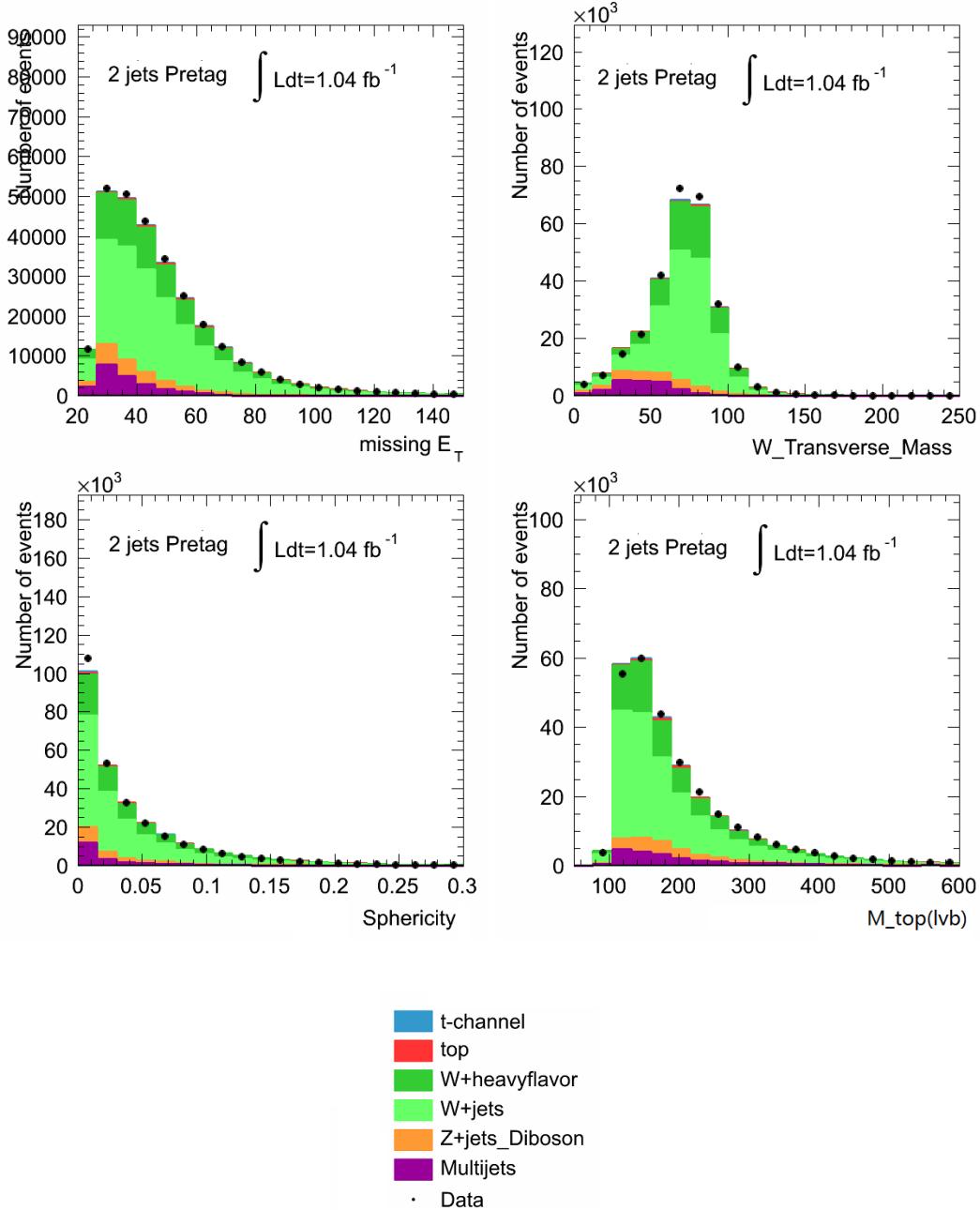
Figure A.7: Stacked distributions of the variables used as input of the BDT for the 2-jets pretag sample.
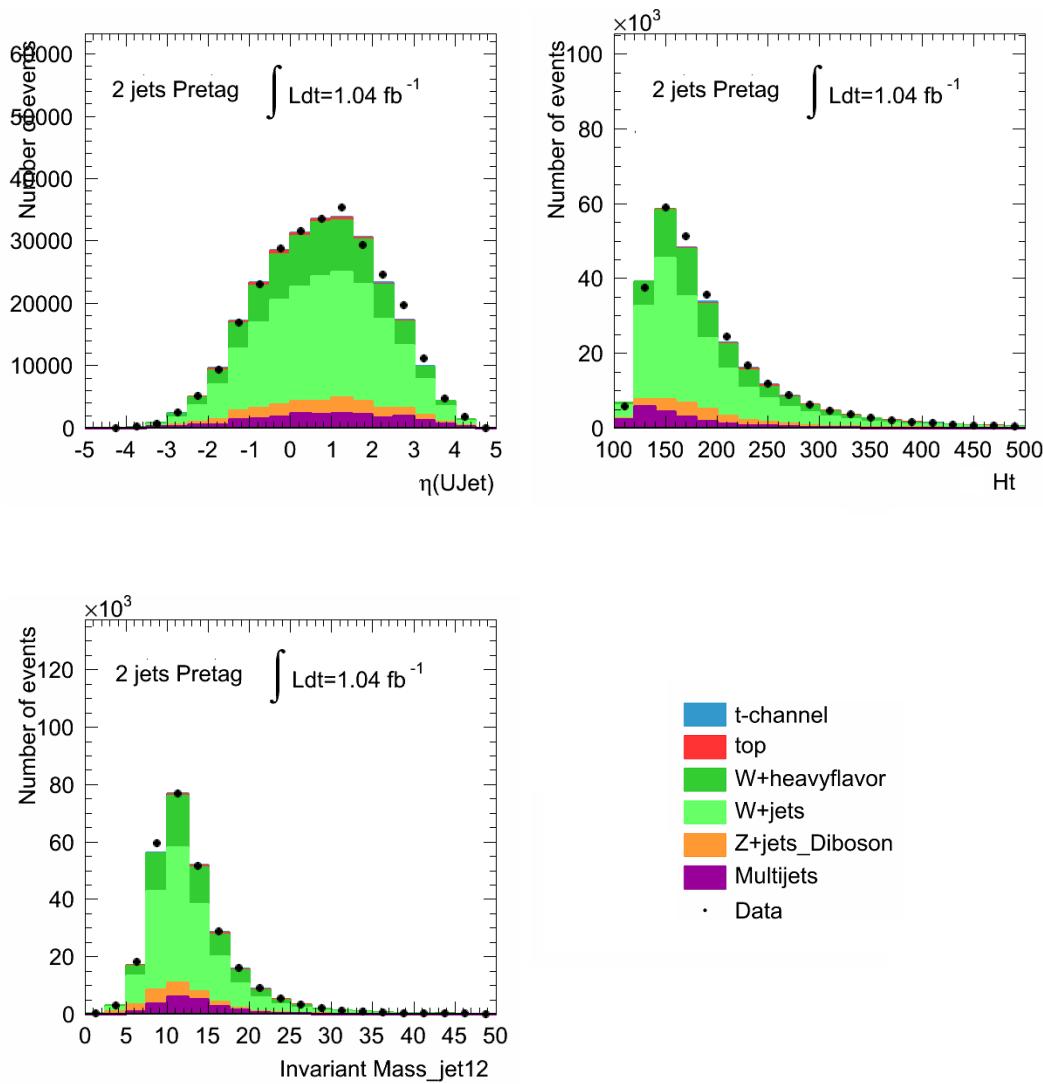
Figure A.8: Stacked distributions of the variables used as input of the BDT for the 2-jets pretag sample.
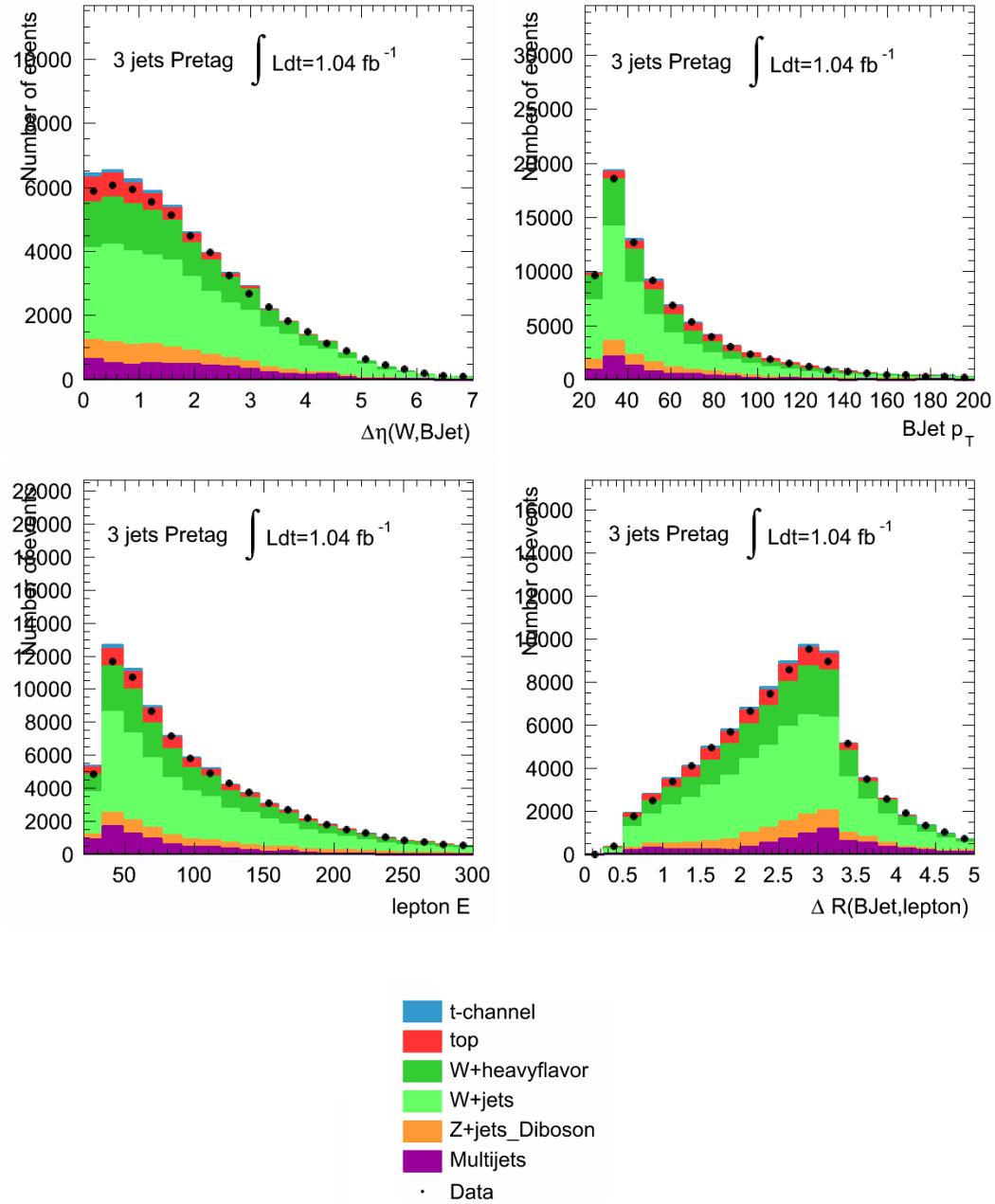
Figure A.9: Stacked distributions of the variables used as input of the BDT for the 3-jets pretag sample.
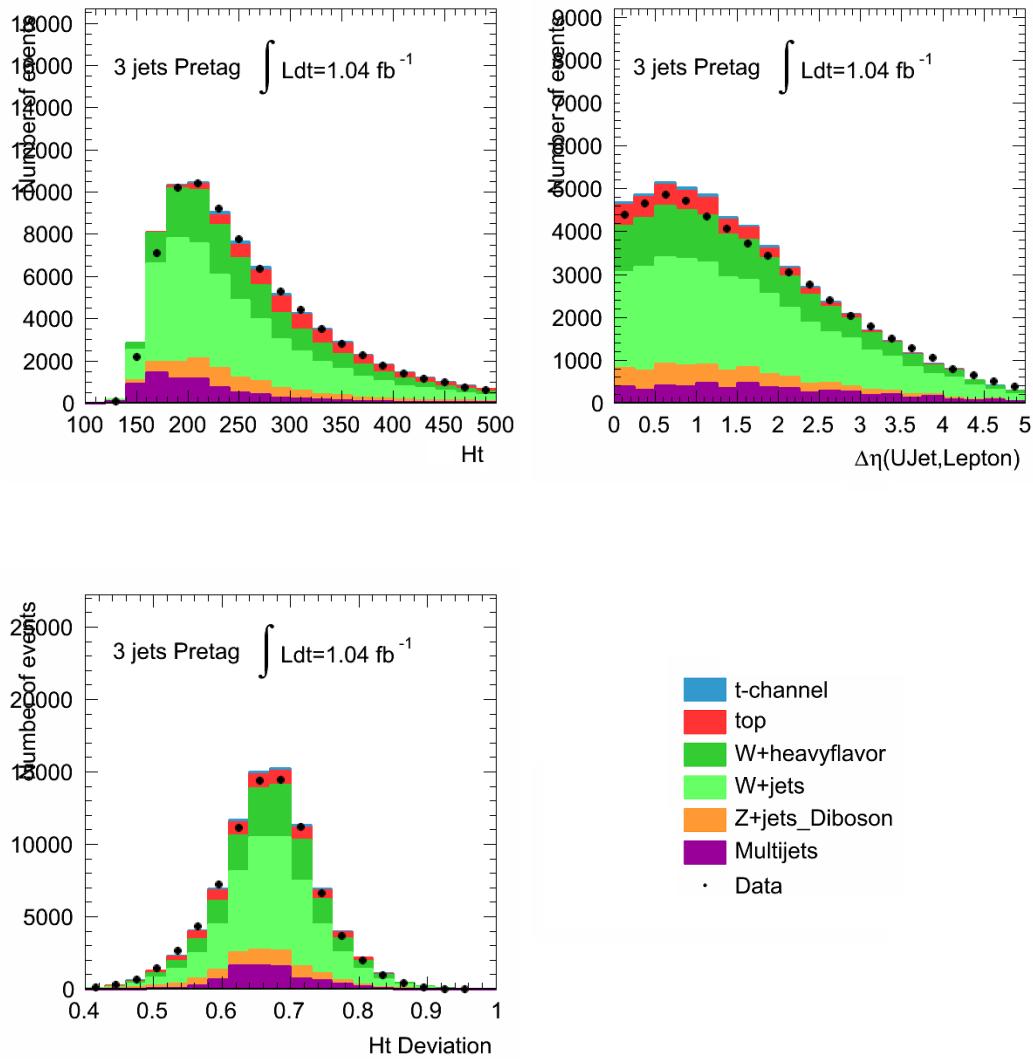
Figure A.10: Stacked distributions of the variables used as input of the BDT for the 3-jets pretag sample.
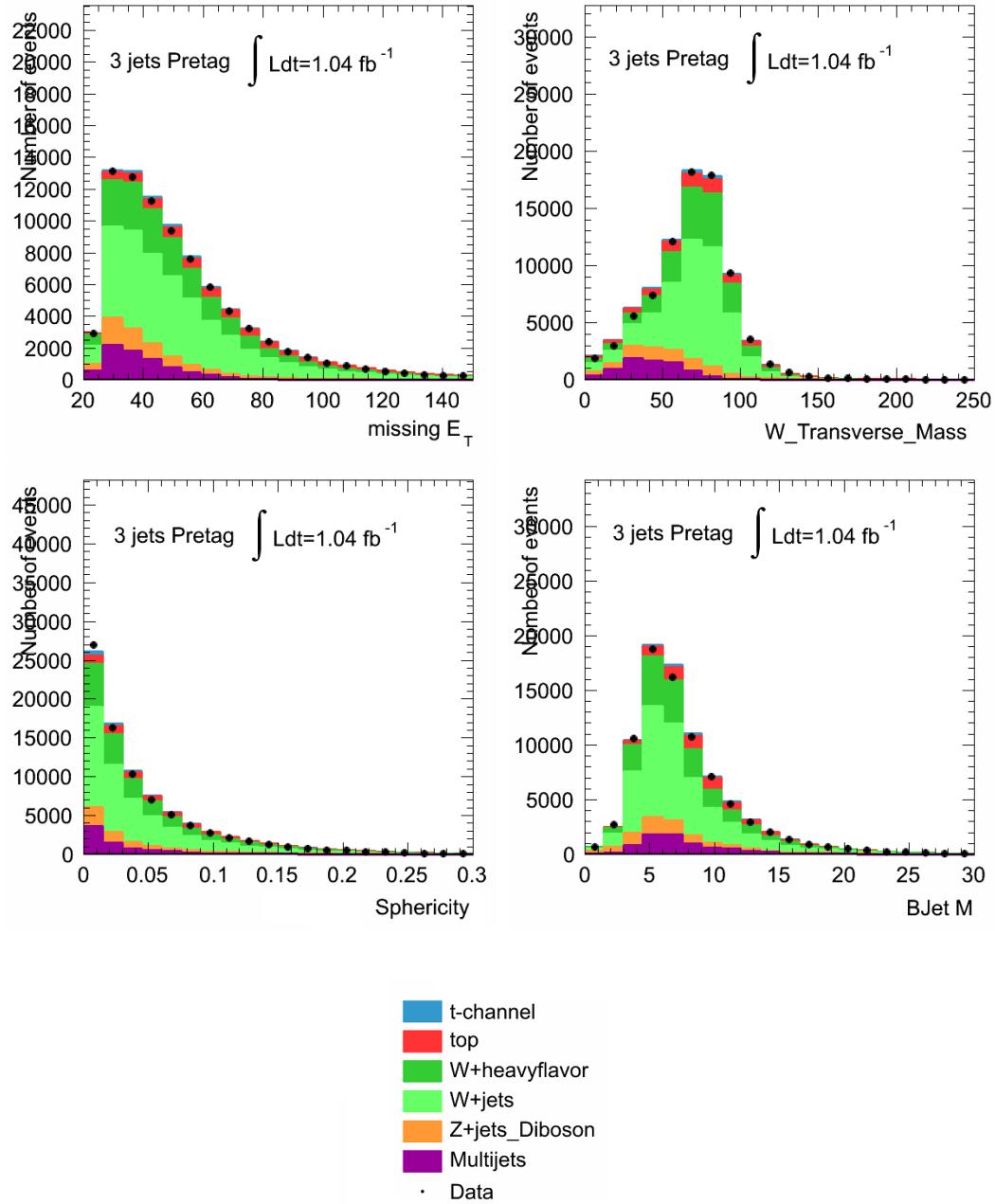
Figure A.11: Stacked distributions of the variables used as input of the BDT for the 3-jets pretag sample.
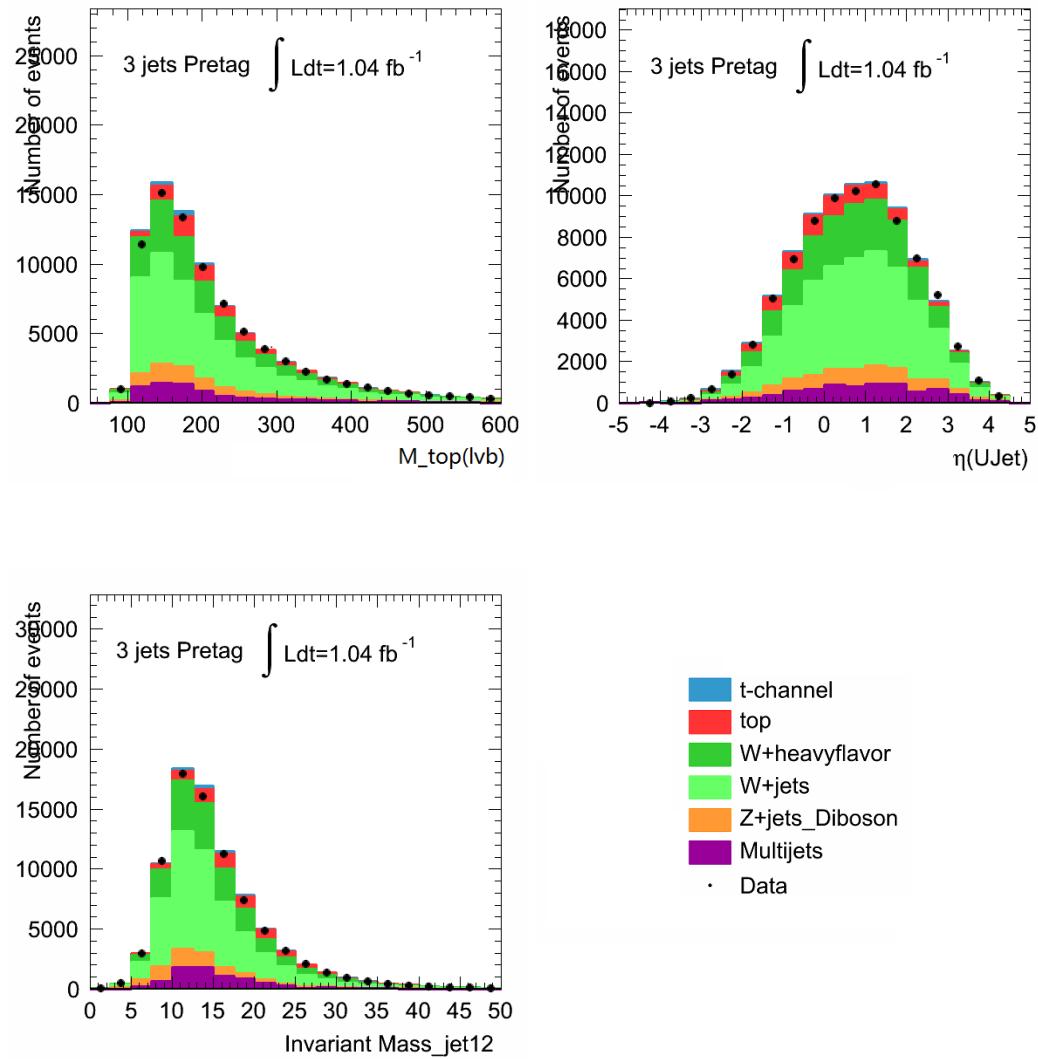
Figure A.12: Stacked distributions of the variables used as input of the BDT for the 3-jets pretag sample.
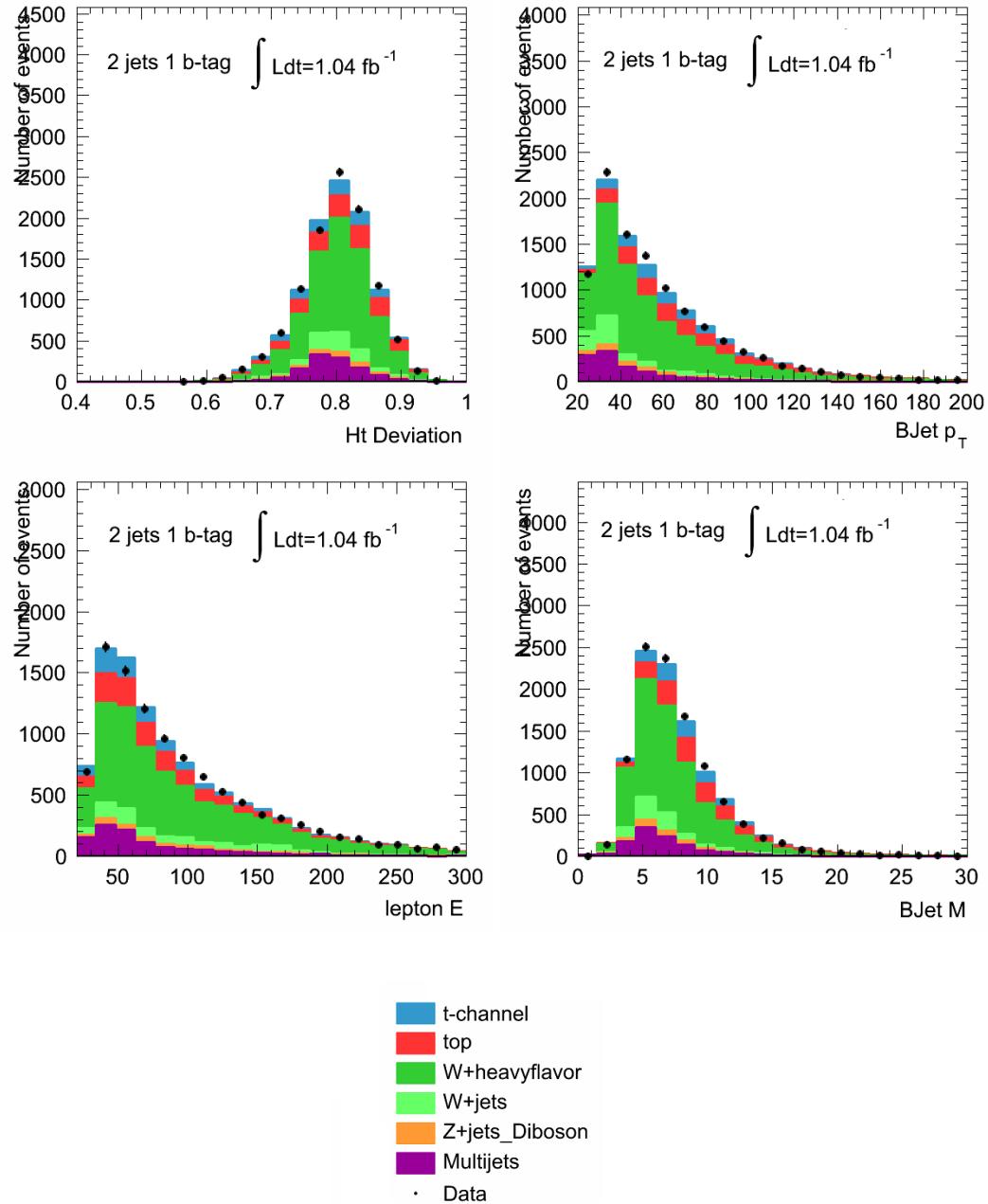
Figure A.13: Stacked distributions of the variables used as input of the BDT for the 2-jets tag sample.
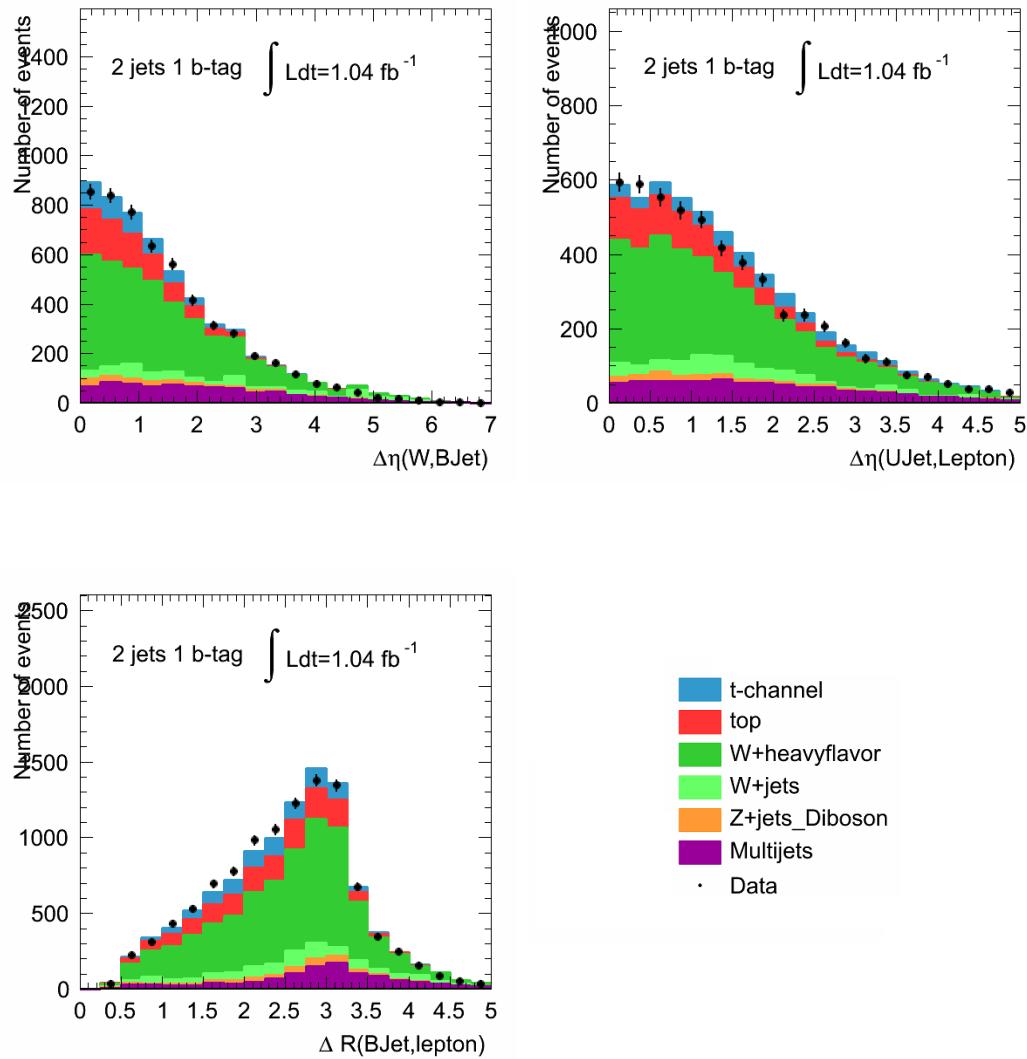
Figure A.14: Stacked distributions of the variables used as input of the BDT for the 2-jets tag sample.
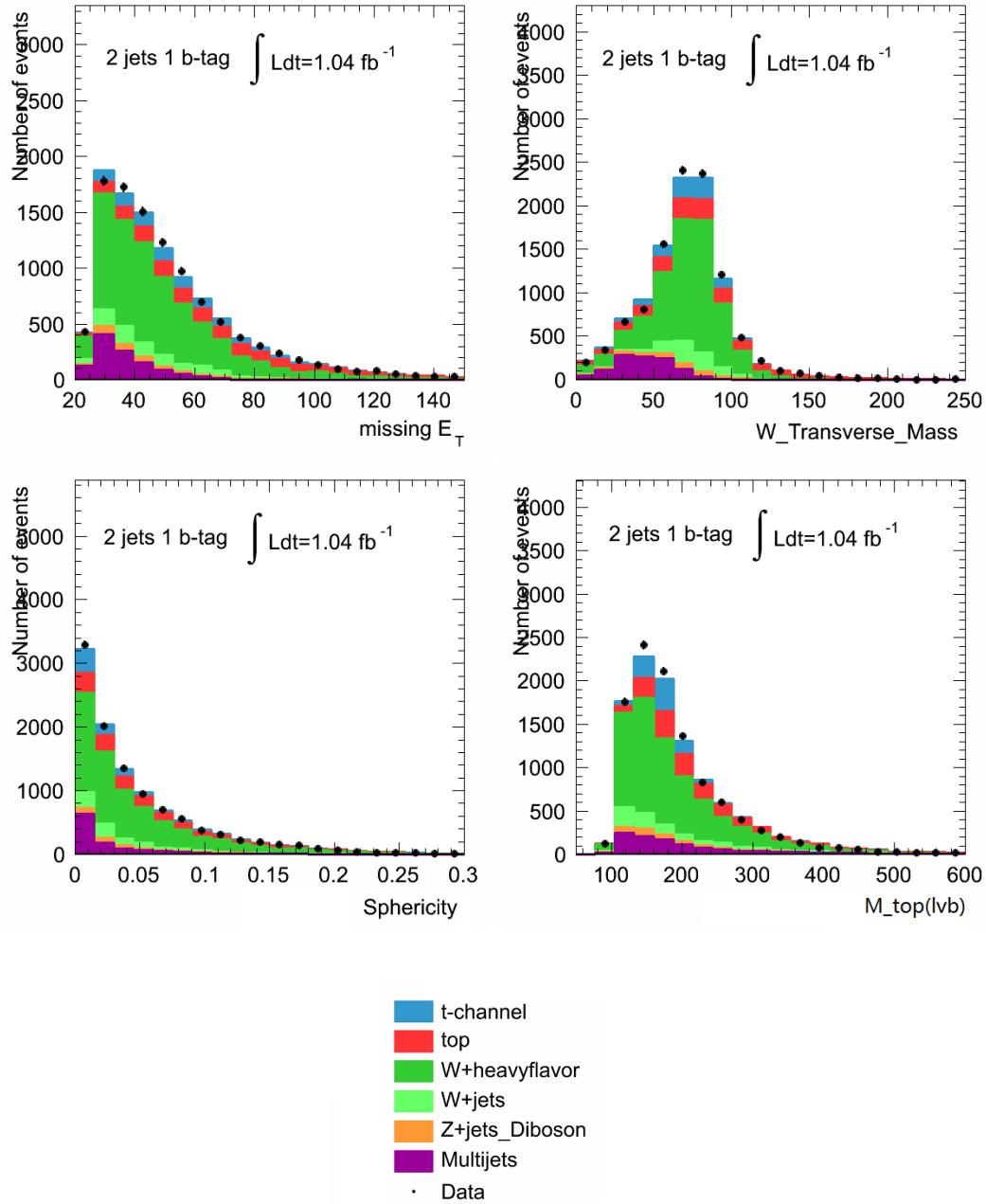
Figure A.15: Stacked distributions of the variables used as input of the BDT for the 2-jets tag sample.
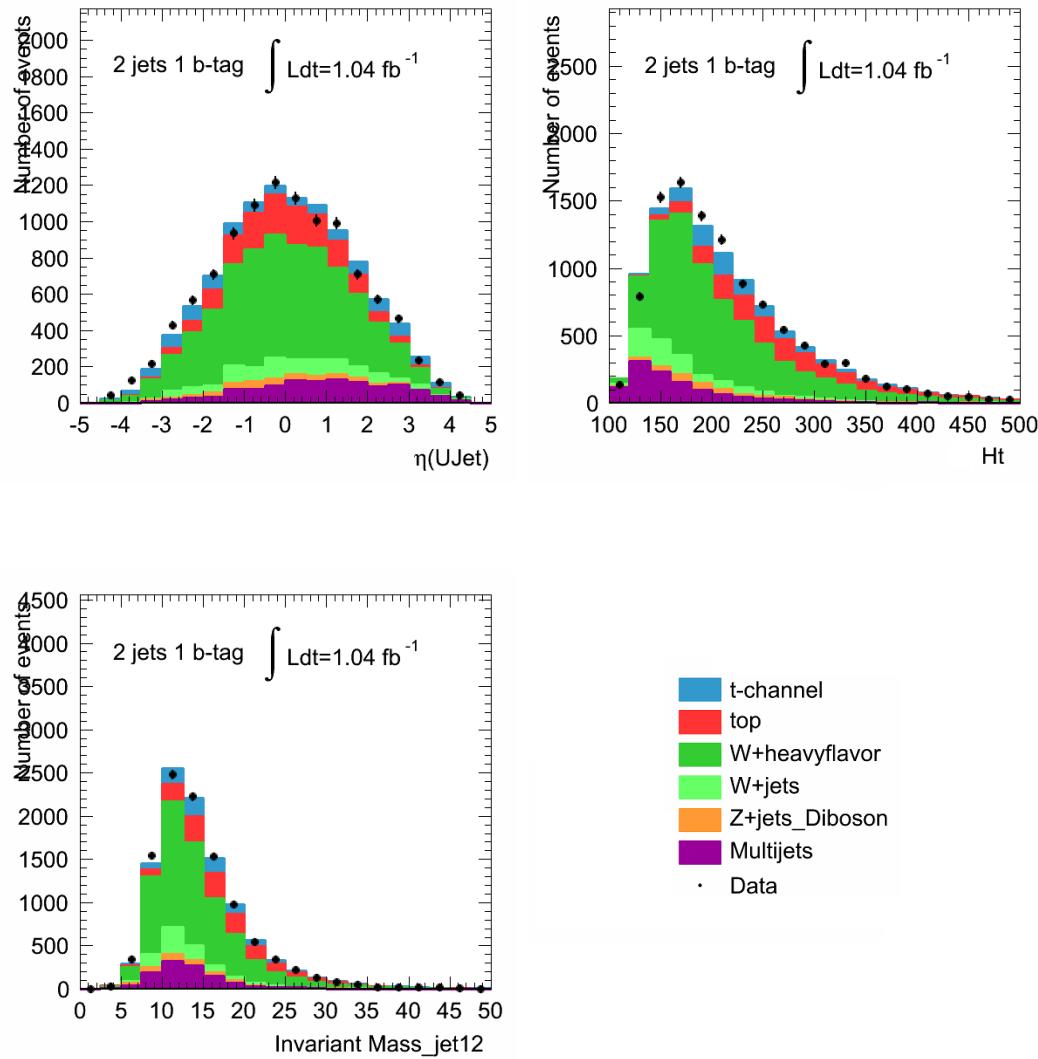
Figure A.16: Stacked distributions of the variables used as input of the BDT for the 2-jets tag sample.
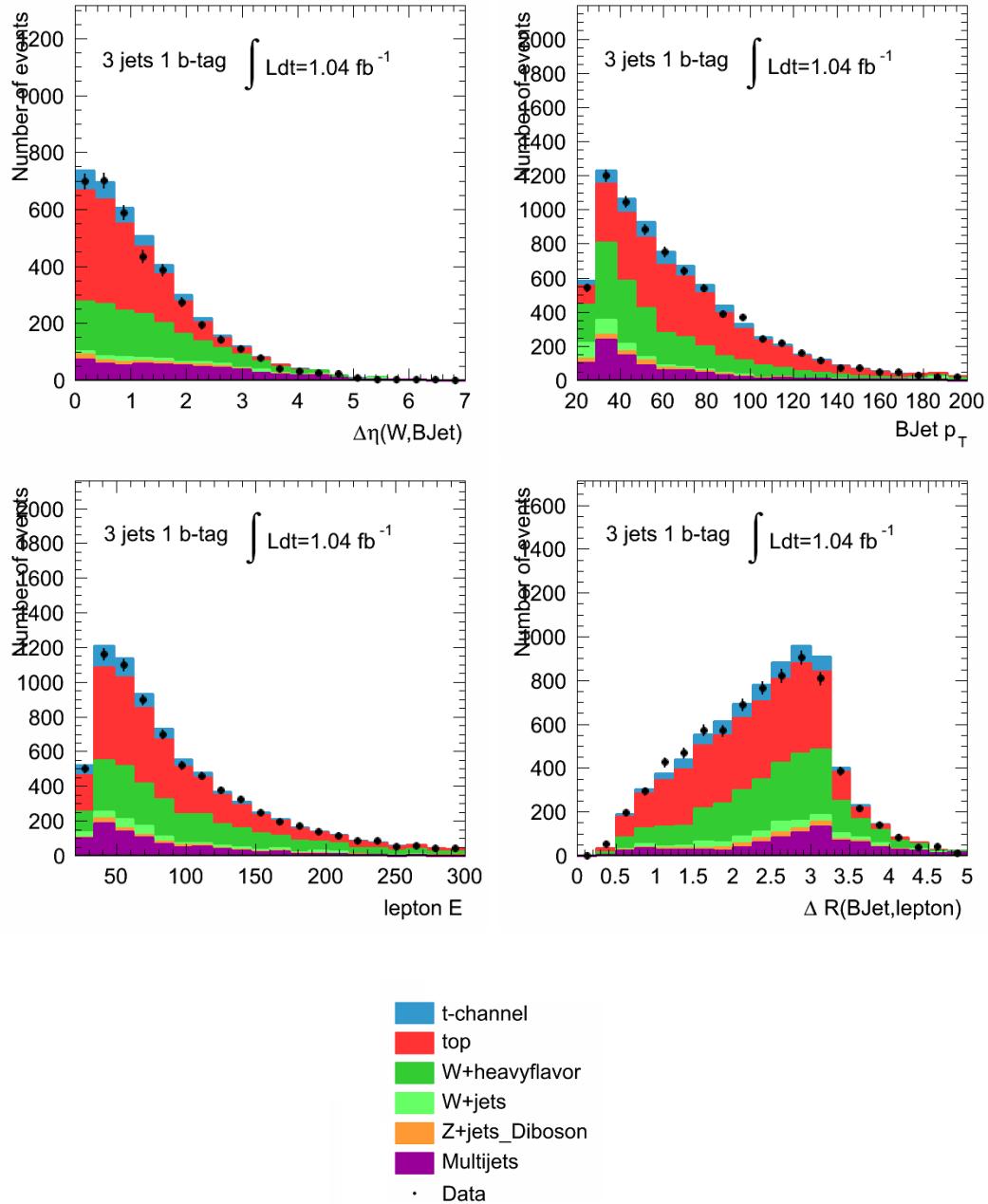
Figure A.17: Stacked distributions of the variables used as input of the BDT for the 3-jets tag sample.
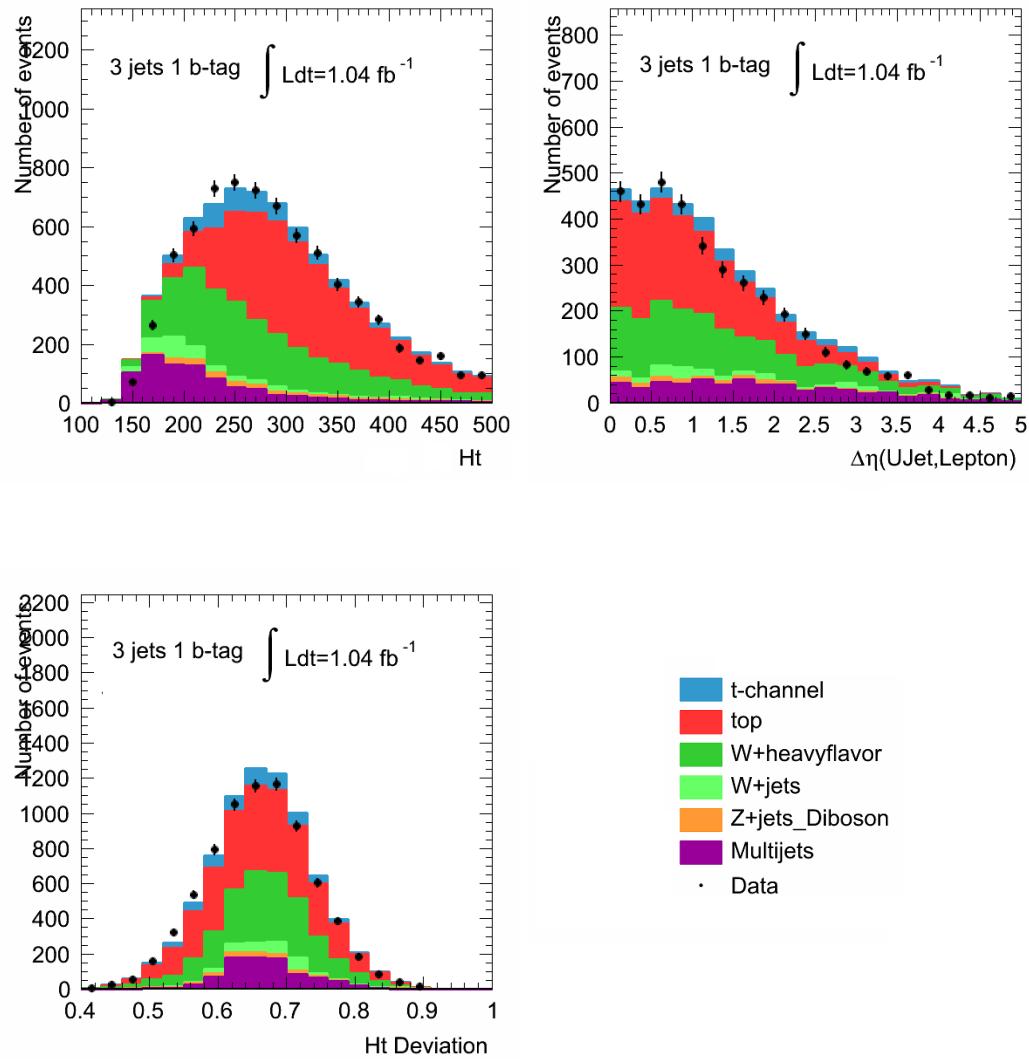
Figure A.18: Stacked distributions of the variables used as input of the BDT for the 3-jets tag sample.
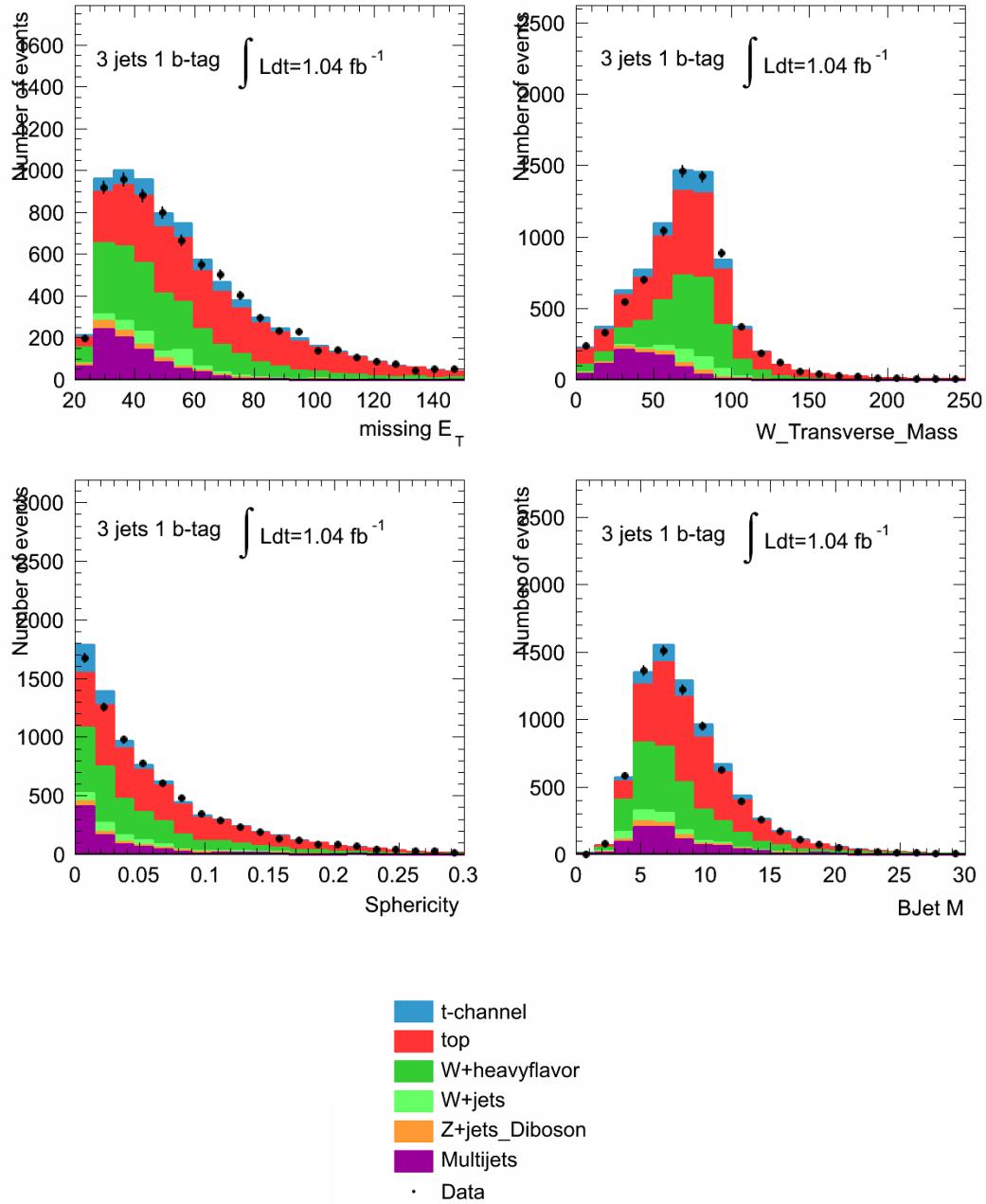
Figure A.19: Stacked distributions of the variables used as input of the BDT for the 3-jets tag sample.
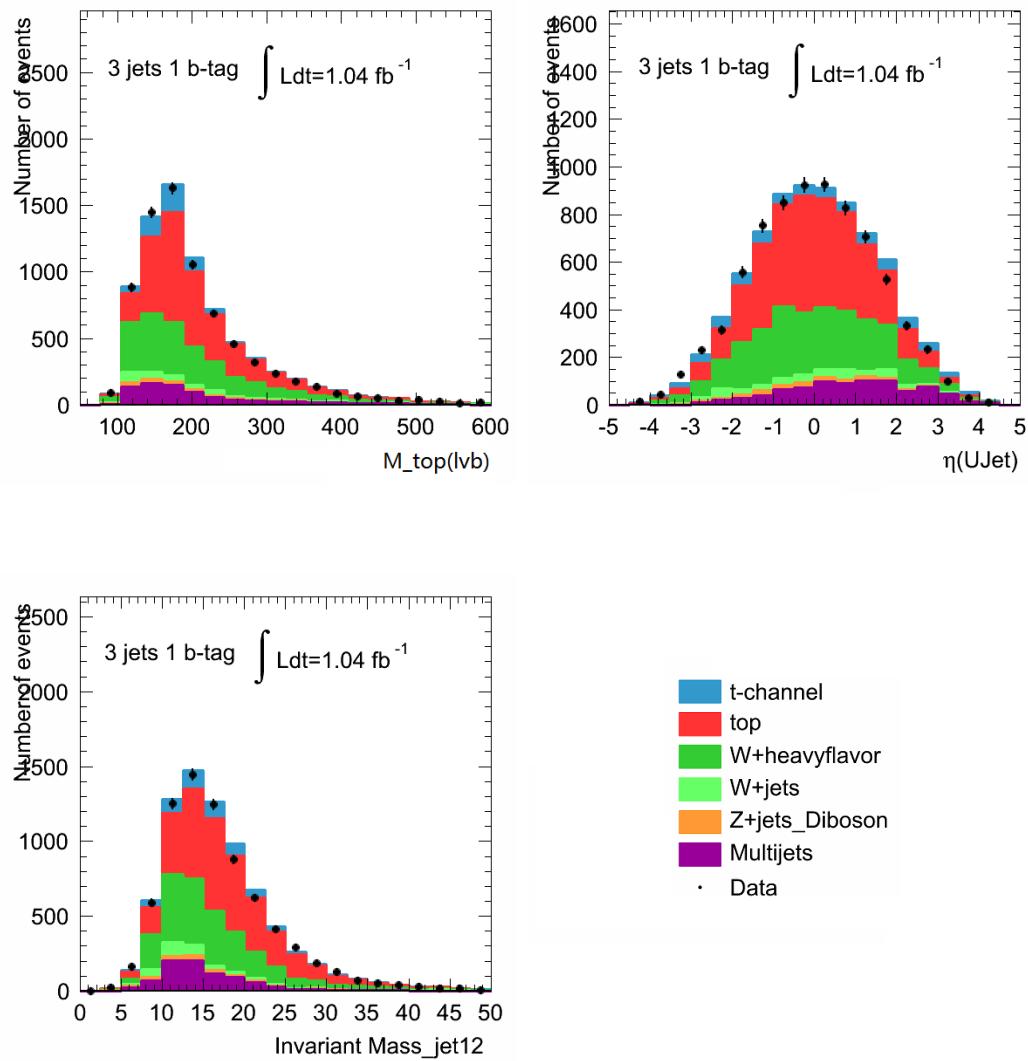
Figure A.20: Stacked distributions of the variables used as input of the BDT for the 3-jets tag sample.

BIBLIOGRAPHY

[1] J. R. Incandela, A. Quadt, W. Wagner, and D. Wicke, *Status and Prospects of Top-Quark Physics*, `arXiv:0904.2499`.

[2] ATLAS Collaboration, *Statistical combination of top quark pair production cross-section measurements using dilepton, single-lepton, and all-hadronic final states at s = 7 TeV with the ATLAS detector*, Tech. Rep. ATLAS-CONF-2012-024, CERN, Geneva, 2012.

[3] CMS Collaboration, *Combination of top quark pair production cross section measurements*, Tech. Rep. CMS-PAS-TOP-11-024, CERN, Geneva, 2011.

[4] M. Aliev et al., *HATHOR HAdronic Top and Heavy quarks crOss section calculatoR*, Comput.Phys.Commun. **182** (2011) 1034C1046.

[5] S. M. U. Langenfeld and P. Uwer, *Measuring the running top-quark mass*, Phys.Rev. D **80** (2009) 054009.

[6] N. Kidonakis, *Next-to-next-to-leading soft-gluon corrections for the top quark cross section and transverse momentum distribution*, Phys.Rev. D **82** (2010) 114030.

[7] M. N. e. a. V. Ahrens, A. Ferroglia, *Renormalization-Group Improved Predictions for Top-Quark Pair Production at Hadron Colliders*, JHEP **1009** (2010) 097.

[8] *Rudolf LEY, PS Division, CERN, 02.09.96 Revised and adapted by Antonella Del Rosso, ETT Div., in collaboration with B. Desforges, SL Div., and D. Manglunki, PS Div. CERN*, 23.05.01.

[9] D. Fournier, *Performance of the LHC, ATLAS and CMS in 2011*, tech. rep. `arXiv:1201.4681v1`.

[10] ATLAS Collaboration, *The ATLAS Experiment at the CERN Large Hadron Collider*, J. Instrum. **3** (2008) S08003.

[11] ATLAS Collaboration, *Expected electron performance in the ATLAS experiment*, Tech. Rep. ATL-PHYS-PUB-2011-006, CERN, Geneva, 2011.

[12] ATLAS Collaboration, *Measurement of the Mistag Rate of b-tagging algorithms with $5fb^{-1}1$ of Data Collected by the ATLAS Detector*, Tech. Rep. ATLAS-CONF-2012-040, CERN, Geneva, 2012.

[13] ATLAS Collaboration, *Commissioning of the ATLAS high-performance b-tagging algorithms in the 7 TeV collision data*, Tech. Rep. ATLAS-CONF-2011-102, CERN, Geneva, 2011.

[14] ATLAS Collaboration, *Luminosity Determination in pp Collisions at sqrts = 7TeV using the ATLAS Detector in 2011*, Tech. Rep. ATLAS-CONF-2011-116, CERN, Geneva, 2011.

[15] *108th LHCC Meeting AGENDA OPEN Session*, tech. rep. `ATLAS Status Report`.

[16] B. Marcello, *Mass measurements of the top quark in electroweak production channels at ATLAS*. PhD thesis, 2006.

[17] *Useful Diagrams of Top Signals and Backgrounds*, Http://www-d0.fnal.gov/run2physics/top/top-public-web-pages/top-feynman-diagrams.html.

[18] ATLAS Collaboration, B. Alvarez, K. Becker, M. Castanheira, D. Chakraborty, S. Caughron, T. Delemontex, J. Donini, C. Feng, D. Hirschbuehl, J. Holzbauer, J. Koll, J. Kraus, J. Linnemann, A. Lleres, A. Lucotte, J. Morris, I. Ochoa, B. Pope, R. Schwienhorst, P. Sturm, C. Suhr, X. Sun, W. Wagner, J. Wang, C. Weydert, H. Zhang, and H. Zhu, *Measurement of the t-channel single top-quark production cross section in pp collisions at $\sqrt{s} = 7$ TeV with the ATLAS detector*, Tech. Rep. TOPQ-2011-14, CERN, Geneva, 2011.

[19] B. Alvarez, K. Becker, M. Castanheira, D. Chakraborty, S. Caughron, T. Delemontex, J. Donini, C. Feng, D. Hirschbuehl, J. Holzbauer, J. Koll, J. Kraus, J. Linnemann, A. Lleres, A. Lucotte, J. Morris, I. Ochoa, B. Pope, R. Schwienhorst, P. Sturm, C. Suhr, X. Sun, W. Wagner, J. Wang, C. Weydert, H. Zhang, and H. Zhu, *BLUE combination of single top 1 t-channel measurements*, Tech. Rep. ATL-COM-PHYS-2011-1407, CERN, Geneva, November, 2011.

[20] N. Kidonakis, *Next-to-next-to-leading-order collinear and soft gluon corrections for t-channel single top quark production*, Phys. Rev. D **83** (2011) 091503, `arXiv:1103.2792 [hep-ph]`.

[21] CMS Collaboration, *Measurement of the single top t-channel cross section in pp collisions at $\sqrt{s} = 7$ TeV using 2011 data*, Tech. Rep. CMS-PAS-TOP-11-021, CERN, Geneva, 2011.

[22] D0 Collaboration, e. a. V. Abazov, *Model-independent measurement of t-channel single top quark production in $p\bar{p}$ collisions at $\sqrt{s} = 1.96$ TeV*, submitted to Phys. Lett. B (2011) , `arXiv:1105.2788v1 [hep-ex]`.

[23] CDF Collaboration, *First Observation of Electroweak Single Top Quark Production*, Phys. Rev. Lett. **103** (2009) 092002.

[24] F. M. e. a. J. M. Campbell, R. Frederix, *NLO predictions for t-channel production of single top and fourth generation quarks at hadron colliders*, JHEP **10** (2009) 042.

[25] M. Kobayashi and T. Maskawa, *CP-violation in the renormalizable theory of weak interaction*, Prog. Theor. Phys. **49** (1973) 652–657.

[26] K. N. et al., *Review of Particle Physics: The CKM Quark-Mixing Matrix*, Journal of Physics G **37** (2010) 150.

[27] S. L. Glashow, *Partial Symmetries of Weak Interactions*, Nucl. Phys. **22** (1961) 579–588.

[28] S. Weinberg, *A Model of Leptons*, Phys. Rev. Lett. **19** (1967) 1264–1266.

[29] A. Salam, *Gauge Unification of Fundamental Forces*, Rev. Mod. Phys. **52** (1980) 525–538.

[30] W. Hollik, *Electroweak Theory*, J. Phys. (2006) 53.

[31] P. W. Higgs, *Spontaneous Symmetry Breakdown without Massless Bosons*, Phys. Rev. **145** (1966) 1156–1163.

[32] H. Yukawa, *On the interaction of elementary particles*, Proc. Phys. Math. Soc. Jap. **17** (1935) 48–57.

[33] D. Gross and F. Wilczek Phys. Rev. Lett. **30** (1973) 1343.

[34] F. Abe et al., *Observation of top quark production in $p\bar{p}$ collisions with the Collider Detector at Fermilab*, Phys. Rev. Lett. **74** (1995) 2626.

[35] D0 Collaboration, S. Abachi et al., *Observation of the top quark*, Phys. Rev. Lett. **74** (1995) 2632–2637, `arXiv:9503003 [hep-ex]`.

[36] CDF and D0 Collaboration, M. Lancaster, *Combination of CDF and D0 results on the mass of the top quark using up to 5.8 fb-1 of data*, `arXiv:1107.5255 [hep-ex]`.

[37] W. J. Marciano, *Precision Electroweak Measurements and the Higgs Mass*, `arXiv:0411179v2 [hep-ph]`.

[38] B. L. Combridge, *Associated production of heavy flavour states in pp and $p\bar{p}$ interactions: Some QCD estimates*, Nucl. Phys. B **151** (1979) 429–456.

[39] Z. G. S. W. Bernreuther, A. Brandenburg and P. Uwer, *Top quark pair production and decay at hadron colliders*, Nucl. Phys. B **690** (2004) 81–137, `arXiv:0403035v1 [hep-ph]`.

174

[40] e. a. V. Ahrens, A. Ferroglia, *Renormalization-Group Improved Predictions for Top-Quark Pair Production at Hadron Colliders*, Nucl. Phys. B **151** (2010) 60, `arXiv:1003.5827`.

[41] M. Czakon Nucl. Phys. **B849** (2011) 250, `arXiv:1001.0642`.

[42] *Predictions in the paper are calculated with Hathor [4] to compute approximate NNLO cross sections with CTEQ66 [103] and $m_{top} = 172.5 \ GeV$*, 2011.

[43] R. Frederix, *Top quark phenomenology at hadron colliders.* PhD thesis, 2009.

[44] W. Bernreuther, *Top quark physics at the LHC*, `arXiv:0805.1333v1`.

[45] S. Willenbrock and D. Dicus, *Production of Heavy Quarks from W Gluon Fusion*, Phys. Rev. **D34** (1986) 155.

[46] L. P. Z. S. B.W. Harris, E. Laenen and S.Weinzierl Phys. Rev. **D66** (2002) 054024.

[47] F. M. J.M. Campbell, R. Frederix and F. Tramontano Phys. Rev. Lett. **122** (2009) 182003.

[48] P. M. P. Falgari and A. Signer Phys. Rev. **D82** (2010) 054028.

[49] C. M. R. Schwienhorst, C.-P. Yuan and Q.-H. Cao Phys. Rev. **D83** (2011) 034019.

[50] P. M. P. Falgari, F. Giannuzzi and A. Signer Phys. Rev. **D83** (2011) 094013.

[51] N. Kidonakis Phys. Rev. **D75** (2007) 071501.

[52] N. Kidonakis, *NNLL resummation for s-channel single top quark production*, Phys. Rev. D **81** (2010) 054028, `arXiv:1001.5034 [hep-ph]`.

[53] N. Kidonakis, *Two-loop soft anomalous dimensions for single top quark associated production with a W- or H-*, Phys. Rev. D **82** (2010) 054018, `arXiv:1005.4451 [hep-ph]`.

[54] Particle Data Collaboration, S. E. et al. Phys. Lett. B **592** 1.

[55] M. Jezabek and J. H. Kuhn, *QCD Corrections to Semileptonic Decays of Heavy Quarks*, Nucl. Phys. B **314** (1989) 1.

[56] J. H. Kuhn, *Theory of top quark production and decay*, `arXiv:9707321 [hep-ph]`.

[57] N. F. C. e. a. J. Aguilar-Saavedra, J. Carvalho, *Probing anomalous Wtb couplings in top pair decays*, Eur.Phys.J. **C50** 519.

[58] CDF Collaboration, e. a. T. Aaltonen, *Observation of the top quark*, Phys. Rev. Lett. **D81** (2010) , `arXiv:1004.3224v2 [hep-ex]`.

[59] CDF Collaboration, P. U. S. Moch, *Observation of the top quark*, Nucl. Phys. Proc. Suppl. **183** (2008) 75.

[60] CMS Collaboration, e. a. S. Chatrchyan Eur. Phys. J. **C71** 1721.

[61] CMS Collaboration, e. a. S. Chatrchyan Phys. Rev. **D84** 092004.

[62] CMS Collaboration, e. a. S. Chatrchyan JHEP **1107** 049.

[63] ATLAS Collaboration, e. a. G. Aad Phys.Lett.B **707** 459–477.

[64] C.-P. Y. T. Tait Phys. Rev. D (2001) 014018.

[65] CDF Collaboration, e. a. T. Aaltonen Phys.Rev.Lett. **103** 092002.

[66] D0 Collaboration, e. a. V. Abazov Phys.Rev.Lett. **103** 092001.

[67] N. Kidonakis, *Single top quark production at the Fermilab Tevatron: Threshold resummation and finite-order soft gluon corrections*, Phys. Rev. D **74** (2006) 114012.

[68] CDF and D0 Collaboration, T. E. W. Group, *Combination of CDF and D0 Measurements of the Single Top Production Cross Section*, `arXiv:0908.2171v1 [hep-ex]`.

[69] E. L. (ed.) and B. P. (ed.), *LHC Machine*, J. Instrum. **3** (2008) S08001.

[70] *LHC Design Report*, tech. rep., CERN, Geneva, 2004.

[71] CMS Collaboration, *The CMS Experiment at the CERN LHC*, J. Instrum. **3** (2008) S08004.

[72] LHCb Collaboration, *The LHCb Detector at the LHC*, J. Instrum. **3** (2008) S08005.

[73] ALICE Collaboration, *The ALICE Experiment at the CERN LHC*, J. Instrum. **3** (2008) S08002.

[74] LHCf Collaboration, *The LHCf Detector at the CERN Large Hardron Collider*, J. Instrum. **3** (2008) S08006.

176

[75] TOTEM Collaboration, *The TOTEM Detector at the CERN Large Hardron Collider*, J. Instrum. **3** (2008) S08007.

[76] *http://lhc-statistics.web.cern.ch/LHC-Statistics/*, tech. rep. `LHC Performance and Statistics`.

[77] *109th LHCC Meeting AGENDA OPEN Session*, tech. rep. `LHC Machine Status Report`.

[78] A. Y. et al, *The ATLAS central solenoid*, Nucl. Instrum. Meth. A **584** (2008) 53.

[79] A. F. et al, *Assembly concept and technology of the ATLAS barrel toroid*, IEEE T. Appl. Supercond **16** (2006) 565.

[80] D. E. B. et al, *Engineering status of the end cap toroid magnets for the ATLAS experiment at LHC*, IEEE T. Appl. Supercond **10** (2000) 357.

[81] A. A. et al, *The barrel modules of the ATLAS semiconductor tracker*, Nucl. Instrum. Meth. A **575** (2006) 642.

[82] A. A. et al, *The ATLAS TRT Barrel Detector*, JINST **3** (2008) P02014.

[83] A. A. et al, *The ATLAS TRT End-cap Detector*, JINST **3** (2008) P10003.

[84] ATLAS Collaboration, *ATLAS liquid-argon calorimeter: Technical Design Report*, Tech. Rep. ATLAS-TDR-002, CERN-LHCC-96-041, CERN, Geneva, 1996.

[85] ATLAS Collaboration, *ATLAS tile calorimeter: Technical Design Report*, Tech. Rep. ATLAS-TDR-003, CERN-LHCC-96-042, CERN, Geneva, 1996.

[86] ATLAS Collaboration, *ATLAS muon spectrometer: Technical Design Report*, Tech. Rep. ATLAS-TDR-010, CERN-LHCC-97-022, CERN, Geneva, 1997.

[87] ATLAS Collaboration, *Electron performance measurements with the ATLAS detector using the 2010 LHC proton-proton collision data*, Tech. Rep. CERM-PH-EP-2011-117. `arXiv:1110.3714v1 [hep-ex]`.

[88] ATLAS Collaboration, *Expected performance of the ATLAS experiment: detector, trigger and physics*, Tech. Rep. CERM-OPEN-2008-20. `arXiv:0901.0512 [hep-ex]`.

[89] *MuidMuonCollection*, Https://twiki.cern.ch/twiki/bin/viewauth/atlasprotected/muidmuoncollection.

[90] ATLAS Collaboration, *Track Reconstruction in the ATLAS Muon Spectrometer with MOORE*, Tech. Rep. ATL-SOFT-2003-007, CERN, Geneva, 2003.

[91] G. P. Salam and G. Soyez, *A Practical Seedless Infrared-Safe Cone jet algorithm*, JHEP **05** (2007) 086, `arXiv:0704.0292 [hep-ph]`.

[92] ATLAS Collaboration, *Jet energy measurement with the ATLAS detector in proton-proton collisions at $\sqrt{s} = 7$ TeV*, Tech. Rep. CERN-PH-EP-2011-191. `arXiv:1112.6426v1 [hep-ex]`.

[93] ATLAS Collaboration, *Expected Performance of the ATLAS Experiment - Detector, Trigger and Physics*, `arXiv:0901.0512v4 [hep-ex]`.

[94] ATLAS Collaboration, *Performance of impact parameter-based b-tagging algorithms with the ATLAS detector using pp collisions at $\sqrt{s} = 7$ TeV*, Tech. Rep. ATLAS-CONF-2010-091, CERN, Geneva, 2010.

[95] G. Piacquadio and C. Weiser, *A new inclusive secondary vertex algorithm for b-jet tagging in ATLAS*, J. Phys. **119** (2008) 032032.

[96] ATLAS Collaboration, *Measurement of Missing Tranverse Energy*, Tech. Rep. ATL-PHYS-PUB-2009-016, CERN, Geneva, 2009.

[97] ATLAS Collaboration, *Luminosity Determination in pp Collisions at sqrt(s)=7 TeV Using the ATLAS Detector at the LHC*, Eur. Phys. J. **C71** (2011) 1630.

[98] ATLAS Collaboration, *Forward Detectors for Luminosity Measurement and Monitoring*, Tech. Rep. CERN/LHCC/2004-010.

[99] ATLAS Collaboration, *The ATLAS Beam Conditions Monitor*, IEEE Nucl. Sci. Symp. Conf. Rec. **3** (2005) 1360.

[100] ATLAS Collaboration, *ATLAS Computing: Technical Design Report*, Tech. Rep. CERN-LHCC-2005-022, CERN, Geneva, 2005.

[101] ATLAS Collaboration, *Commissioning of ATLAS Data Quality Infrastructure with First Collision Data*, J. Phys. **331** (2011) 032009.

[102] GEANT4 Collaboration, *GEANT4: A simulation toolkit*, Nucl. Instrum. Meth. **A506** (2003) 250–303.

[103] J. Pumplin et al., *New generation of parton distributions with uncertainties from global QCD analysis*, JHEP **07** (2002) 012.

[104] B. P. Kersevan and R. W. Elzbieta, *The Monte Carlo Event Generator AcerMC version 3.5 with interfaces to PYTHIA 6.4, HERWIG 6.5 and ARIADNE 4.1*, hep-ph/0405247 (2008) .

[105] M. L. Mangano, M. Moretti, F. Piccinini, R. Pittau, and A. D. Polosa, *ALPGEN, a generator for hard multiparton processes in hadronic collisions*, JHEP **07** (2003) 001, `arXiv:hep-ph/0206293`.

[106] S. Frixione, B. R. Webber, and P. Nason, *MC@NLO Generator version 3.4*, hep-ph/0204244 and hep-ph/0305252 (2002) .

[107] P. Nason, *A new method for combining NLO QCD computations with parton shower simulations*, JHEP 11(2004)-040, hep-ph/0409146 (2004) .

[108] S. Frixione, P. Nason, et al., *Positive weight next-to-leading-order Monte Carlo*, JHEP 11(2007)-126 and JHEP 09(2007)111, hep-ph/07092092 and hep-ph/07073088 (2007) .

[109] G. Corcella et al., *HERWIG 6.5: an event generator for Hadron Emission Reactions With Interfering Gluons (including supersymmetric processes)*, JHEP **01** (2001) 010, `arXiv:hep-ph/0011363`.

[110] T. Sjostrand, S. Mrenna, and P. Skands, *PYTHIA Generator version 6.418*, JHEP **05** (2006) 026.

[111] J. M. Butterworth, J. R. Forshaw, and M. H. Seymour, *Multiparton interactions in photoproduction at HERA*, Z. Phys. C **72** (1996) 637–646, `arXiv:hep-ph/9601371`.

[112] N. L. e. a. S. Hoeche, F. Krauss, *Matching Parton Showers and Matrix Elements*, .

[113] *Single Top Object Definition*, Https://twiki.cern.ch/twiki/bin/view/atlasprotected/singletopntuplesforeps.

[114] ATLAS Top Group, *Mis-identified lepton backgrounds in top quark pair production studies for EPS 2011 analyses*, Tech. Rep. ATL-COM-PHYS-2011-768, CERN, Geneva, September, 2011.

[115] ATLAS Collaboration, B. Alvarez, K. Becker, M. Castanheira, D. Chakraborty, S. Caughron, T. Delemontex, J. Donini, C. Feng, D. Hirschbuehl, J. Holzbauer, J. Koll, J. Kraus, J. Linnemann, A. Lleres, A. Lucotte, J. Morris, I. Ochoa, B. Pope, R. Schwienhorst, P. Sturm, C. Suhr, X. Sun, W. Wagner, J. Wang, C. Weydert, H. Zhang, and H. Zhu, *Measurement of t-Channel Single Top-Quark Production in pp Collisions at $\sqrt{s} = 7$ TeV using Neural Networks*, Tech. Rep. ATL-COM-PHYS-2011-1404, CERN, Geneva, 2011.

[116] B. Alvarez, K. Becker, M. Castanheira, D. Chakraborty, S. Caughron,
T. Delemontex, J. Donini, C. Feng, D. Hirschbuehl, J. Holzbauer, J. Koll, J. Kraus,
J. Linnemann, A. Lleres, A. Lucotte, J. Morris, I. Ochoa, B. Pope, R. Schwienhorst,
P. Sturm, C. Suhr, X. Sun, W. Wagner, J. Wang, C. Weydert, H. Zhang, and
H. Zhu, *Measurement of t-Channel Single Top-Quark Production Cross-section with
pp Collisions using a Cuts-Based Approach*, Tech. Rep.
ATL-COM-PHYS-2011-1402, CERN, Geneva, November, 2011.

[117] J. Quinlan, *Induction of Decision Trees*, Machine Learning **1** (1986) 81–106.

[118] B. R. H.-J. Yang and J. Zhu, *Studies of Boosted Decision Trees for MiniBooNE
Particle Identification*, Nucl. Instrum. Methods Phys. Res., Sect. A **555** (2005) 370.

[119] ATLAS Collaboration, B. Alvarez, K. Becker, M. Castanheira, D. Chakraborty,
S. Caughron, T. Delemontex, J. Donini, C. Feng, D. Hirschbuehl, J. Holzbauer,
J. Koll, J. Kraus, J. Linnemann, A. Lleres, A. Lucotte, J. Morris, I. Ochoa, B. Pope,
R. Schwienhorst, P. Sturm, C. Suhr, X. Sun, W. Wagner, J. Wang, C. Weydert,
H. Zhang, and H. Zhu, *Measurement on t-channel single-top quark production using
boosted decision trees*, Tech. Rep. ATL-COM-PHYS-2011-1405, CERN, Geneva,
2011.

[120] M. Feindt, *A Neural Bayesian Estimator for Conditional Probability Densities*,
`arXiv:0402093v1 [physics.data-an]`.

[121] M. Feindt and U. Kerzel, *The NeuroBayes Neural Network Package*, Nucl. Instrum.
Meth. **A559** (2006) 190–194.

[122] A. Hocker et al., *TMVA: Toolkit for multivariate data analysis*, PoS **ACAT** (2007)
040, `arXiv:physics/0703039`.

[123] L. Breiman, J. Friedman, R. Olshen, and C. Stone, *Classification and Regression
Trees*. Wadsworth and Brooks, Monterey, CA, 1984.

[124] Y. Freund and R. E. Schapire, *A Decision-Theoretic Generalization of On-Line
Learning and an Application to Boosting*, Journal of Computer and System Sciences
55 (1997) no. 1, 119 – 139.

[125] ATLAS Top Group, *TopSystematicUncertainties*,
Https://twiki.cern.ch/twiki/bin/view/atlasprotected/topsystematicuncertainties2011plhc.

[126] J. Campbell and R. Ellis, *Mcfm—monte carlo for femtobarn processes.*,
Http://mcfm.fnal.gov.

[127] R. D. Cousins, J. T. Linnemann, and J. Tucker, *Evaluation of three methods for calculating statistical significance when incorporating a systematic uncertainty into a test of the background-only hypothesis for a Poisson process*, Nucl. Instrum. Methods Phys. Res., A **595** (2008) 480.

[128] M. Feindt, *A Neural Bayesian Estimator for Conditional Probability Densities*, `arXiv:0402093v1 [physics.data-an]`.

[129] M. Feindt and U. Kerzel, *The NeuroBayes Neural Network Package*, Nucl. Instrum. Meth. A **559** (2006) 190.

[130] *Search for W+t single-top events in the dileptonic channel at ATLAS*, Tech. Rep. ATLAS-CONF-2011-104, CERN, Geneva, 2011.

[131] *Search for single top tW associated production in the dilepton decay channel in pp collisions at $\sqrt{s} = 7$ TeV*, Tech. Rep. CMS-PAS-TOP-11-022, CERN, Geneva, 2011.

[132] J. A. Aguilar-Saavedra Acta Phys. Polon. B **35** (2004) 2695C2710.

[133] *Search for FCNC single top-quark production at $\sqrt{s} = 7$ TeV with the ATLAS detector*, Tech. Rep. CERN-PH-EP-2012-032, CERN, Geneva, 2012. `arXiv:1203.0529 [hep-ex]`.

[134] T. T. E. Malkawi and C. P. Yuan, *A Model of Strong Flavor Dynamics for the Top Quark*, Phys. Lett. B **385** (1996) 304.

[135] B. A. D. G. Burdman and E. Ponton, *Resonances from two universal extra dimensions*, Phys. Rev. D **74** (2006) 075008.

[136] M. Perelstein, *Little Higgs models and their phenomenology*, Prog. Part. Nucl. Phys. **58** (2007) 247.

[137] F. M. Jeremy Andrea, Benjamin Fuks, *Monotops at the LHC*, Tech. Rep. IPHC-PHENO-11-03, 2011. `arXiv:1106.6199 [hep-ph]`.

[138] F. S. D. H. J. L. F. M. W. W. M. Z. H. Lacker, A. Menzel, *Model-independent extraction of $|V_{tq}|$ matrix elements from top-quark measurements at hadron colliders*, Tech. Rep. CP3-12-01, 2012. `arXiv:1202.4694 [hep-ph]`.

[139] P. S. Saurabh D. Rindani, *Probing anomalous tbW couplings in single-top production using top polarization at the Large Hadron Collider*, tech. rep., 2011. `arXiv:1107.2597 [hep-ph]`.

[140] J. D. W. Sunghoon Jung, Aaron Pierce, *Top asymmetry and the search for a light hadronic resonance in association with single top*, tech. rep., 2011. `arXiv:1108.1802 [hep-ph]`.

[141] J.-F. S. Yao-Bei Liu, *Associated production of the charged Higgs boson and single top quark at the LHC*, Mod.Phys.Lett.A **24** (2009) 143–150.

[142] D0 Collaboration, V. M. Abazov et al., *Model-independent measurement of t-channel single top quark production in $p\bar{p}$ collisions at $\sqrt{s} = 1.96$ TeV*, `arXiv:1105.2788 [hep-ex]`.

[143] ATLAS Collaboration, e. a. G. Aad Eur.Phys.J. **C71** 1577.

[144] ATLAS Collaboration, *ATLAS Trigger Performance: Technical Design Report*, Tech. Rep. CERN-LHCC-98-015, CERN, Geneva, 1998.

[145] *LHC Beam Operation workshop*, tech. rep. `Evian 2011`.

[146] *LHC Performance Workshop*, tech. rep. `Chamonix 2012`.

[147] ATLAS single top group, *Strategy to Search for Single-Top Events using early Data of the ATLAS Detector at the LHC*, Tech. Rep. ATL-PHYS-PUB-2010-003, CERN, Geneva, May, 2010.

[148] *Commissioning of the ATLAS high-performance b-tagging algorithms in the 7 TeV collision data*, Tech. Rep. ATLAS-CONF-2011-102, CERN, Geneva, Jul, 2011.

[149] ATLAS Collaboration, *Searches for Single Top-Quark Production with the ATLAS Detector in pp Collisions at $\sqrt{s} = 7$ TeV*, ATLAS-CONF-2011-027 (2011) .

[150] ATLAS Top Group, *Scale Factors For Use in Rel 16 analyses*, Https://twiki.cern.ch/twiki/bin/view/atlasprotected/topcommonscales2011plhc.

[151] K. Becker, D. Hirschbuehl, P. Sturm, and W. Wagner, *Measurement of t-Channel Single Top-Quark Production in pp Collisions at sqrts = 7TeV using Neural Networks*, Tech. Rep. ATL-COM-PHYS-2011-688, CERN, Geneva, Jun, 2011.

[152] *Measurement of the t-channel Single Top-Quark Production Cross Section in 0.70 fb-1 of pp Collisions at $\sqrt{(s)} = 7$ TeV with the ATLAS detector*, Tech. Rep. ATLAS-CONF-2011-101, CERN, Geneva, Jul, 2011.

ACKNOWLEDGMENTS